UNIVERSITY OF CRETE

DEPARTMENT OF BIOLOGY

FOUNDATION FOR RESEARCH & TECHNOLOGY HELLAS
INSTITUTE OF ELECTRONIC STRUCTURE AND LASER (IESL)

Material processing via ultra-short pulsed laser: Study of the outgrowth and interfacing of neural networks in 3D Si scaffolds

PhD-Thesis

Chariklia (Hara) Simitzi

Supervisor : Professor Irene Athanassakis

Heraklion, Crete, July 2014

ΠΑΝΕΠΙΣΤΗΜΙΟ ΚΡΗΤΗΣ
ΤΜΗΜΑ ΒΙΟΛΟΓΙΑΣ

ΙΔΡΥΜΑ ΤΕΧΝΟΛΟΓΙΑΣ & ΕΡΕΥΝΑΣ
ΙΝΣΤΙΤΟΥΤΟ ΗΛΕΚΤΡΟΝΙΚΗΣ ΔΟΜΗΣ ΚΑΙ ΛΕΙΖΕΡ

Μικροεπεξεργασία υλικών με λέιζερ στενών παλμών: Μελέτη της ανάπτυξης και διεπαφής δικτύων νευρικών κυττάρων σε 3Δ ικριώματα πυριτίου

Διδακτορική Διατριβή

Χαρίκλεια (Χαρά) Σιμιτζή

Επιβλέπουσα: Καθηγήτρια Ειρήνη Αθανασάκη

Ηράκλειο, Κρήτη, Ιούλιος 2014

Η διατριβή αφιερώνεται

στη μνήμη της μητέρας μου,

η οποία επέμενε στην ομορφιά της αίσθησης του κόσμου

και στον πατέρα μου,

ο οποίος επέμενε στην ομορφιά της παρατήρησης του κόσμου.

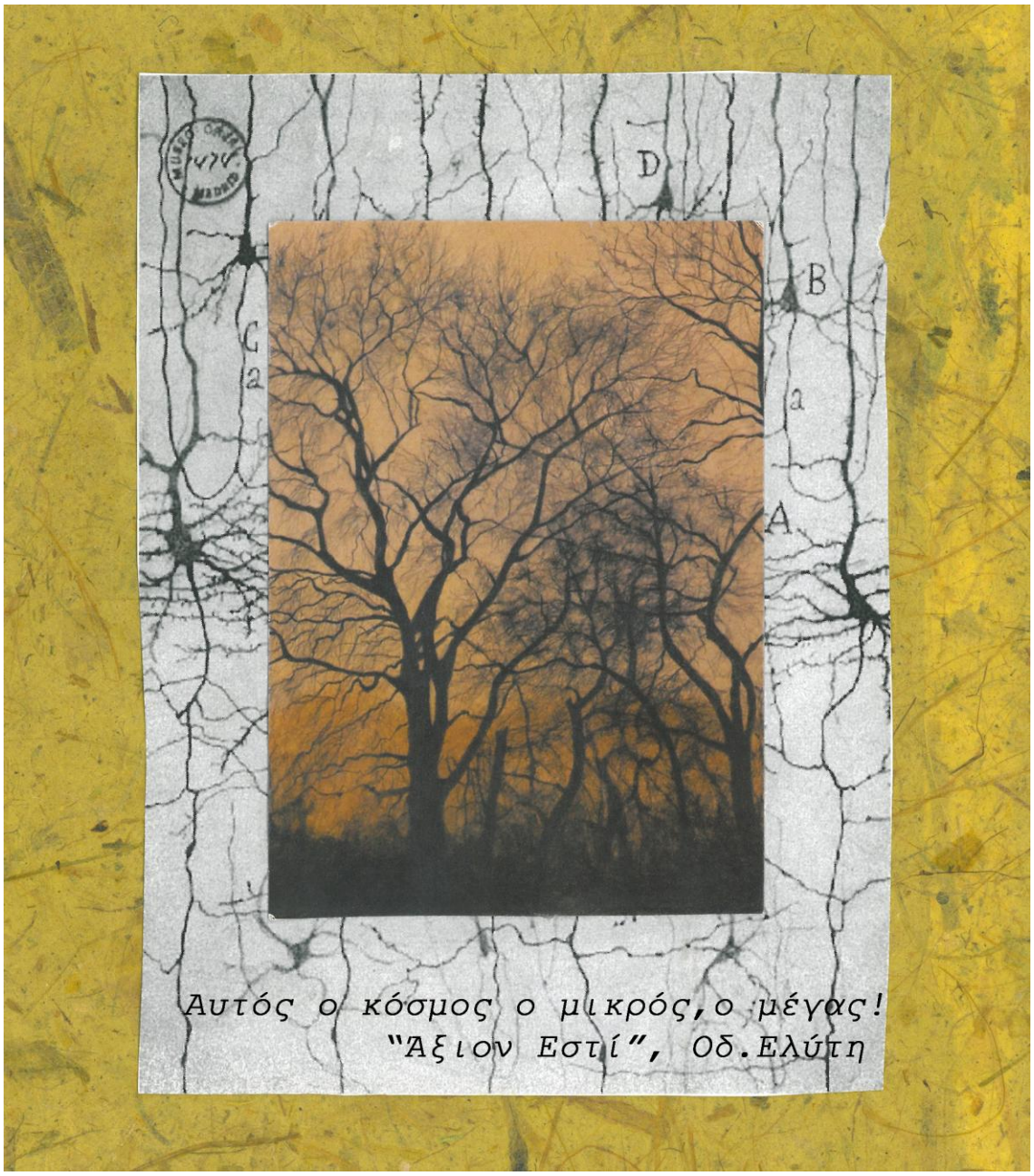

***Στην εικόνα απεικονίζεται τμήμα των περίφημων σκίτσων του Santiago Ramón y Cajal, που αναπαριστά νευρικά κύτταρα του εγκεφάλου.**

Preface

This PhD thesis has been elaborated in the Biology Department of the University of Crete (UoC) in collaboration with the Institute of Electronic Structure and Laser (IESL) of the Foundation for Research and Technology-Hellas (FORTH).

It has been co-financed by the European Union (European Social-Fund ESF) and Greek national funds through the Operational Program "Education and Lifelong Learning" of the National Strategic Reference Framework (NSRF) - Research Funding Program: Heracleitus II.

Ευχαριστίες

Καταρχήν θα ήθελα να εκφράσω τις εγκάρδιες ευχαριστίες μου στην επιβλέπουσα καθηγήτρια μου κ. Ειρήνη Αθανασάκη, για την εμπιστοσύνη που μου έδειξε και την υποστήριξή της όλα αυτά τα χρόνια σε επιστημονικό και σε ανθρώπινο επίπεδο. Επίσης, για τον ανθρωπισμό που επιδεικνύει στην έρευνα.

Είμαι ειλικρινά ευγνώμων στον καθηγητή κ. Κώστα Φωτάκη για την ευκαιρία που μου έδωσε να εκπονήσω το διδακτορικό μου στο ΙΤΕ σε συνεργασία με το Πανεπιστήμιο Κρήτης.

Πολλές εγκάρδιες ευχαριστίες στον κ. Μανώλη Στρατάκη και την κ. Ανθή Ρανέλλα για την εμπιστοσύνη που μου έδειξαν και την εξαιρετική συνεργασία που είχαμε. Τούς ευχαριστώ για το όμορφο κλίμα όλα αυτά τα χρόνια.

Επίσης, θα ήθελα να ευχαριστήσω τα υπόλοιπα μέλη της 3μελούς επιτροπής, την καθ. κ. Μαρία Βαμβακάκη και την καθ. κ. Κική Σιδηροπούλου για τα πολύτιμα σχόλια τους κατά την διάρκεια του διδακτορικής διατριβής.

Επιπλέον, θα ήθελα να ευχαριστήσω και τα υπόλοιπα μέλη της 7μελούς επιτροπής εξέτασης της διδακτορικής διατριβής, καθ. κ. Αχιλλέα Γραβάνη, καθ. κ. Κώστα Χαριτίδη και καθ. κ. Γιάννη Χαραλαμπόπουλο για την ανάγνωση του κειμένου και τα εποικοδομητικά σχόλια τους.

Πολλές θερμές ευχαριστίες στον Πασχάλη Ευσταθόπουλο και την Αλεξάνδρα Κουργιαντάκη, σε συνεργασία με τους οποίους πραγματοποιήθηκαν τα πειράματα με τις πρωτογενείς καλλιέργειες. Το όμορφο κλίμα συνεργασίας και ανταλλαγής ιδεών μαζί τους ήταν εξαιρετικά πολύτιμο.

Επειδή η παρούσα διατριβή είναι κατεξοχήν διεπιστημονικού χαρακτήρα, υπάρχουν πολλοί άνθρωποι οι οποίοι με βοήθησαν σε όλη αυτή την διαδρομή.

Ειδικότερα, θα ήθελα να ευχαριστήσω τον David Grey και τον Μάριο Μπαρμπέρογλου για την βοήθειά τους στην πειραματική διάταξη και λειτουργία του λέιζερ. Επίσης, τον Γιάννη Λαμπράκη για την τεχνική υποστήριξη στα εργαστήρια των λέιζερ. Ακόμα, ευχαριστώ τη Χριστίνα Γιαννακού για την όμορφη συνεργασία.

Θα ήθελα, επιπλέον, να ευχαριστήσω την κ. Αλέκα Μανουσάκη και την κ. Αλεξάνδρα Σιάκουλη για την συνεχή υποστήριξη τους με την ηλεκτρονική μικροσκοπία σάρωσης.

Αναφορικά με τις καλλιέργειες των κυττάρων θα ήθελα ευχαριστήσω τον Γιώργο Βρέντζο, την Μιρέλλα Γεωργούλη, την Ιωάννα Ζέρβα, τη Βάσω Μελισσινάκη, την Εύα Μπέσσα, τον Ιωσήφ Πεδιατικάκη, και τον Στέλιο Ψυχαράκη.

Επίσης, θέλω να ευχαριστήσω τη Δήμητρα Αχιλλέως, τη Μαρία Καλύβα, την Anca Mateescu και τη Ντίνα Τερζάκη που με βοήθησαν στην λειτουργικοποίηση των υποστρωμάτων.

Επιπλέον, θα ήθελα να ευχαριστήσω την κ. Λαμπρινή Σύγκελλου στο Ινστιτούτο Χημικής Μηχανικής του ΙΤΕ για τον χαρακτηρισμό των δειγμάτων με χρήση φωτοηλεκτρονικής φασματοσκοπίας ακτίνων Χ (XPS).

Τέλος, θα ήθελα να ευχαριστήσω τον Γιώργο Γιαννακάκη για την βοήθειά του στη στατιστική ανάλυση.

Αισθάνομαι τυχερή που η διδακτορική διατριβή μου εκπονήθηκε σε ένα περιβάλλον φιλικό και φιλόξενο, που ενθάρρυνε την συνεργασία, την αλληλεπίδραση ιδεών και τον επιστημονικό διάλογο. Ευχαριστώ όλους τους συναδέλφους και συνεργάτες που συνέβαλλαν με τον τρόπο τους στο όμορφο κλίμα.

Επειδή, όμως, η διδακτορική διατριβή σηματοδοτεί και μια προσωπική διαδρομή, υπάρχουν αρκετοί άνθρωποι εκτός του χώρου του Πανεπιστημίου που θα ήθελα να ευχαριστήσω.

Θα ήθελα εγκάρδια να ευχαριστήσω τις φίλες μου και τους φίλους μου για την αγάπη τους και την πίστη τους σε εμένα. Τις/Τους ευχαριστώ για τις εικόνες που μοιραζόμαστε.

Επίσης, τη Δέσποινα για τη συντροφικότητά της. Τη Στέλλα, τη Σταυρούλα, τη Νατάσσα και την Ευθυμία για την εμπειρία μιας πολύχρωμης συγκατοίκησης.

Τον Κωνσταντίνο, τους συγχορευτές της «Εχταγής» και την Όλια για τις δημιουργικές εικόνες που συνθέσαμε.

Την κ. Μαρία Σπυριδάκη για την πίστη της στις δυνάμεις της ζωής.

Τη Λήδα που επιμένει στην σημασία του βλέμματος και της κατάφασης. Την ευχαριστώ για το μοίρασμα της περιπλάνησης.

Τον Ανδρέα για το ταξίδι που έχει ξεκινήσει.

Abstract

Unlike other tissue types, which consist of cells with a much more homogeneous structure and function, the nervous tissue spans in a complex multilayer environment whose topographical features display a large spectrum of morphologies and size scales. Because of the necessity of a multilayer environment, the well established flat tissue culture surfaces are proven to be insufficient for studying the effect of the topography of the surroundings on nerve cell morphology and function. In an attempt to approach the complexity of the topographical milieu of nerve cells, it is necessary to shift to more complex 3D micropatterned surfaces. Micro-and nanofabrication techniques provide the opportunity to develop new types of cell culture platform, where the effect of various topographical cues on cellular functions such as proliferation and differentiation can be studied. Different approaches (regarding the material, fabrication technique, cell type and assay) have been used in order to fabricate micropatterned surfaces, where the effect of topography on nerve cell development can be studied.

In this study, the cellular growth on micropatterned Si substrates (comprising arrays of microcones -MCs) fabricated by ultra-short pulsed laser processing has been investigated. Using increasing laser fluence, three types of micropatterned Si surfaces, which exhibit different geometrical characteristics (denoted as low, medium and high roughness substrates, respectively), have been fabricated and characterized as to surface morphology, wetting properties and surface chemistry. As roughness increases, among the different geometrical characteristics of the MCs, intercone distance increases and an anisotropic topography becomes more pronounced. These three micropatterned Si substrates together with the unpatterned flat Si have been applied to *in vitro* cell cultures.

PC12 cells were used as a model of nerve cells in order to study the NGF-induced growth and differentiation pattern (neuritogenesis) on the micropatterned Si substrates. Upon NGF treatment, cell differentiation was promoted on low and intermediate roughness substrates, whereas it was strongly inhibited on the highly rough ones. The obtained results suggested that the intercone space did effectively influence the NGF-induced PC12 differentiation fate.

Dissociated primary cells of the PNS were used in order to investigate the topographic guidance of neural outgrowth and network formation of dissociated SCG sympathetic neurons as

well as the effect of (surface) topography on Schwann cell morphology. It was shown that the neuronal network on the low roughness substrates displayed high randomness, whereas the neurons on intermediate and high roughness substrates exhibited a parallel alignment. Furthermore, oriented Schwann cell outgrowth was promoted on intermediate and high roughness substrates. This surface -induced guidance effect was also observed in the whole DRG explant model, where both Schwann cell migration and axonal outgrowth exhibited a surface-dependent response. In this model, it was shown that Schwann cells create a cellular “carpet” onto the substrates. Neurons were, in turn, outgrown on top of them. It is hypothesized that the plasticity of Schwann cells and their processes allowed a glial “carpet” formation, which served as a substrate for neurite outgrowth.

Therefore, it can be concluded that the distinct geometrical characteristics of surface roughness could influence a variety of neuronal and neuroglial cell functions. The laser micropatterned silicon (Si) substrates presented here could potentially be used as model scaffolds for the systematic exploration of the role of 3D microtopography on cell differentiation and neural network outgrowth, where Schwann cell–neuronal interactions could be investigated in the context of nerve tissue regeneration.

Περίληψη

Σε αντίθεση με τους υπόλοιπους ιστούς, οι οποίοι αποτελούνται από κύτταρα πιο ομοιογενή σε δομή και λειτουργία, ο νευρικός ιστός εκτείνεται σε ένα πολύπλοκο και πολυεπίπεδο περιβάλλον, του οποίου τα τοπογραφικά χαρακτηριστικά επιδεικνύουν ένα μεγάλο φάσμα μορφολογιών και μεγεθών. Εξαιτίας της σημασίας ενός τέτοιου περιβάλλοντος, τα συνήθη επίπεδα υποστρώματα καλλιέργειας κυττάρων αποδεικνύονται ανεπαρκή για τη μελέτη της επίδρασης της τοπογραφίας του περιβάλλοντος στην μορφολογία και την λειτουργία των νευρικών κυττάρων. Συνεπώς, για να προσεγγίσουμε την πολυπλοκότητα του τοπογραφικού περιβάλλοντος των νευρικών κυττάρων, είναι απαραίτητο να μεταβούμε σε πιο πολύπλοκες 3Δ μικροδομημένες επιφάνειες. Μέσω των τεχνικών μικρο- και νανο-κατεργασίας, μπορούν να αναπτυχθούν νέου τύπου πλατφόρμες καλλιέργειας κυττάρων, στις οποίες μπορεί να μελετηθεί η επίδραση των διαφόρων τοπογραφικών σινιάλων στις κυτταρικές λειτουργίες, όπως ο πολλαπλασιασμός και η κυτταρική διαφοροποίηση. Διάφορες προσεγγίσεις, αναφορικά με το υλικό, το είδος της τεχνικής, τον τύπο του κυττάρου, κτλ., έχουν αναπτυχθεί για την κατασκευή μικροδομημένων επιφανειών, όπου μπορεί να μελετηθεί η επίδραση της τοπογραφίας στην ανάπτυξη των νευρικών κυττάρων.

Στην παρούσα εργασία, μελετήθηκε η κυτταρική ανάπτυξη πάνω σε μικροδομημένα υποστρώματα πυριτίου (τα οποία αποτελούνται από διατάξεις μικροκώνων) και τα οποία κατασκευάστηκαν με την τεχνική της δόμησης με λέιζερ υπέρστενων παλμών. Αυξάνοντας την πυκνότητα ενέργειας του λέιζερ, κατασκευάστηκαν τρία είδη μικροδομημένων επιφανειών πυριτίου, οι οποίες επιδεικνύουν διαφορετικά γεωμετρικά χαρακτηριστικά (διαβαθμισμένες σε τρεις κατηγορίες χαμηλής, μεσαίας και υψηλής ονομαστικής τραχύτητας). Οι μικροδομημένες επιφάνειες χαρακτηρίστηκαν αναφορικά με την επιφανειακή τους μορφολογία, τις ιδιότητες διαβροχής και την επιφανειακή τους χημεία. Όσο αυξάνεται η τραχύτητα, η απόσταση μεταξύ των κώνων αυξάνεται και η ανισοτροπία της μορφολογίας γίνεται εμφανέστερη. Αυτά τα τρία μικροδομημένα υποστρώματα χρησιμοποιήθηκαν μαζί με επίπεδο πυρίτιο, σε *in vitro* πειράματα με κύτταρα.

Τα PC12 κύτταρα χρησιμοποιήθηκαν ως ένα μοντέλο νευρικών κυττάρων, με σκοπό να ερευνηθεί η επαγόμενη από τον NGF ανάπτυξη και διαφοροποίηση (νευριτογένεση) πάνω στα μικροδομημένα υποστρώματα πυριτίου. Κατόπιν χορήγησης NGF, η κυτταρική διαφοροποίηση ενθαρρύνθηκε στα υποστρώματα χαμηλής και ενδιάμεσης τραχύτητας, ενώ ανεστάλη σε εκείνα της υψηλής τραχύτητας. Τα αποτελέσματα έδειξαν ότι η απόσταση μεταξύ των κώνων επηρεάζει αποτελεσματικά την μοίρα διαφοροποίησης των PC12 κυττάρων.

Πρωτογενή κύτταρα του περιφερικού νευρικού συστήματος χρησιμοποιήθηκαν για να μελετηθεί η τοπογραφική καθοδήγηση στην νευρική ανάπτυξη και την ανάπτυξη νευρικού δικτύου συμπαθητικών νευρώνων, καθώς επίσης και η επίδραση της (επιφανειακής) τοπογραφίας στην μορφολογία των κυττάρων Schwann. Τα αποτελέσματα έδειξαν ότι το νευρικό δίκτυο στα υποστρώματα χαμηλής τραχύτητας ήταν τυχαίου προσανατολισμού, ενώ οι νευρώνες στα υποστρώματα ενδιάμεσης και υψηλής τραχύτητας επιδείκνυαν παράλληλη ευθυγράμμιση. Επιπλέον, στα υποστρώματα ενδιάμεσης και υψηλής τραχύτητας ενθαρρύνθηκε η προσανατολισμένη ανάπτυξη των κυττάρων Schwann. Ανάλογο φαινόμενο επιφανειακά επαγόμενης κατευθυντικότητας παρατηρήθηκε και στο μοντέλο του ολόκληρου γαγγλίου, όπου τόσο η μετανάστευση των κυττάρων Schwann όσο και αξονική ανάπτυξη επιδείκνυαν μια απόκριση εξαρτώμενη από την επιφάνεια του υποστρώματος. Σε αυτό το μοντέλο, τα αποτελέσματα έδειξαν ότι τα κύτταρα Schwann δημιουργούν ένα είδος κυτταρικού "τάπητα" πάνω στα μικροδομημένα υποστρώματα. Οι νευρώνες αναπτύσσονταν πάνω σε αυτά. Διατυπώνεται η υπόθεση ότι η πλαστικότητα των κυττάρων Schwann και των απολήξεών τους επέτρεψε τον σχηματισμό ενός νευρογλοιακού "τάπητα", ο οποίος αποτέλεσε υπόστρωμα για την νευριτική ανάπτυξη.

Συνεπώς, συμπεραίνεται ότι τα συγκεκριμένα γεωμετρικά χαρακτηριστικά της επιφανειακής τραχύτητας μπορούν να επηρεάσουν ένα εύρος νευρικών και νευρογλοιακών κυτταρικών λειτουργιών. Τα μικροδομημένα υποστρώματα πυριτίου που κατασκευάζονται με χρήση λέιζερ και παρουσιάζονται με την παρούσα εργασία, θα μπορούσαν εν δυνάμει να χρησιμοποιηθούν ως πρότυπα ικριώματα για την συστηματική διερεύνηση του ρόλου της 3Δ μικροτοπογραφίας στην κυτταρική διαφοροποίηση και ανάπτυξη νευρικών δικτύων, όπου οι αλληλεπιδράσεις των κυττάρων Schwann με τους νευρώνες θα μπορούσαν να ερευνηθούν αναφορικά με την αναγέννηση του νευρικού ιστού.

CONTENTS

List of Abbreviations

BE: Binding Energies

CNS: Central Nervous System

DIV: Days in Vitro

DOC: Days of Culture

DRG: Dorsal Root Ganglion

ECM: Extracellular Matrix

FBS: Fetal Bovine Serum

FN: Fibronectin

GAG : Glycosaminoglycans

GF: Growth Factor

HS: Horse Serum

LN: Laminin

MC: Microcones

NGF: Nerve Growth Factor

PAN-MA: poly(acrylonitrile-co-methylacrylate

PC12: Pheochromocytoma

PCL: Polycaprolactone

PDL: Poly-D-lysine

PDLA: poly-D-lactide

PDMS: Polydimethylsiloxane

PLGA: Poly(lactic-co-glycolic acid)

PLLA: Poly-L-lactide

PMMA: Poly(methyl methacrylate)

PP: Polypropylene

PS: Polystyrene

SA: Sympathoadrenal

SAM: Self-Assembled Monolayer

SC: Schwann cell

SCG: Superior Cervical Ganglion

SEM: Scanning Electron Microscopy

SF_6: Sulfur hexafluoride

List of Figures

List of Tables

1. General Overview

1.1 The importance of extracellular matrix architecture in cell and tissue organization

Living tissues are intricate ensembles of multiple cell types embedded in a complex, well-defined extracellular space, the *extracellular matrix* (ECM). ECM is a heterogeneous chemical composite made of multiple structural and functional units that resembles a multivalent ligand. It is made up of an interconnected network of macromolecules, which can be grouped in two main categories: 1. fibrous proteins (collagen and elastin) and 2. largely amorphous interfibrillary matrix (glycosaminoglycans, proteoglycans, cell-binding adhesive glycoproteins, solutes and water). Figure 1.1 illustrates the basic components of ECM. Tables 1.1 and 1.2 summarize the key features of fibrous and amorphous ECM components, respectively [B. Alberts et al., 2002; B. O. Palsson, S. N. Bhatia, 2004]. The ECM possesses topographical and chemical/molecular features ranging from nanometers to micrometers. Following a hierarchical assembly pattern, many ECM proteins form large-scale structures up to several hundred micrometers in size that interact with multiple individual cells to coordinate complex multicellular behavior. For instance, collagen fibrils, with diameters ranging from 20–200 nm, can form hierarchically structured microscale collagen fibers [D. E. Birk et al., 1989, 1995; E.G. Canty et al., 2004].

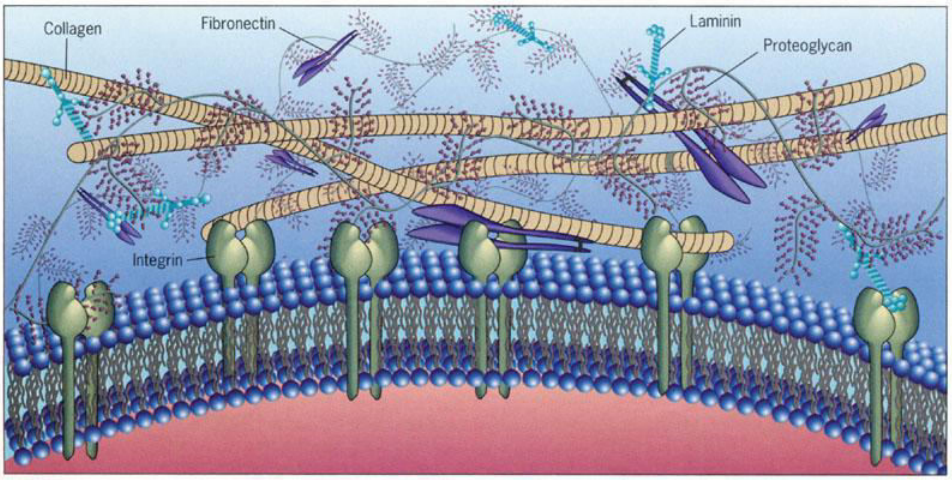

Figure 1.1: Schematic illustration of basic components of ECM
[http://jonlieffmd.com/blog/extra-cellular-matrix-is-critical-to-neuroplasticity]

Table 1.1: Key features of *fibrous* ECM components

Fibrous	(Bio)Chemical Composition	Physicochemical Property	Function	Location
Collagen	A triple helix of three polypeptide α chains; 30 different α chains form at nearly 20 distinct collagen types	-Insoluble -The collagen molecules are packed together into fibrils in which adjacent molecules are tied together by covalent cross-links between neighboring lysine residues, giving the fibril enormous tensile strength	Tissue architecture, tensile strength Cell-matrix Interactions Matrix-Matrix interactions	Ubiquitously distributed
Elastin	Polypeptide chains	-Insoluble -Its relatively loose and unstructured polypeptide chains are cross-linked covalently to generate a rubberlike elastic meshwork	Tissue architecture and elasticity	Tissues requiring elasticity, e.g lung, blood, vessels, heart, skin

Table 1.2: Key features of *amorphous* ECM components

Amoprhous matrix	(Bio)Chemical Composition	Physicochemical Property	Function	Location
GAGs **Hyaluronan**	Long chained polysaccharides	They occupy large amounts of space and form viscous Hydrated gels	Cell-matrix Interactions Matrix-matrix interactions Cell proliferation Cell migration	Ubiquitously distributed
Proteoglycans	Long polysaccharide chains linked covalently to a protein core	-Highly water soluble -GAGs and proteoglycans associate to form huge polymeric complexes in the extracellular matrix.	Cell-matrix interactions Matrix-matrix interactions Cell proliferation Cell migration	Ubiquitously distributed
Adhesive glycoproteins **Fibronectin**	A dimer composed of two very large subunits joined by a pair of disulfide bonds near their carboxyl termini.		Tissue architecture Cell-matrix Interactions Matrix-matrix interactions Cell proliferation Cell migration Opsonin	Ubiquitously distributed
Laminin	A large (~850,000 daltons) flexible complex of three very long polypeptide chains arranged in the shape of an asymmetric cross and held together by disulfide bonds	It consists of a number of functional domains: one binds to type IV collagen, one to heparan sulfate, one to entactin, and two or more to laminin receptor proteins on the surface of cells	Basement Membranes Components Cell migration	Basement Membranes

The structure of a tissue is critical for its function, which is achieved by interactions between the cells and the surrounding extracellular matrix (ECM), a model described by M. Bissel as *dynamic reciprocity* theory [M. Bissell *et al.*, 1982]. According to this model, ECM molecules interact with receptors on the surface of cells, which then transmit signals across the cell membrane to molecules in the cytoplasm. These signals initiate a cascade of events through the cytoskeleton into the nucleus, resulting in the expression of specific genes, whose products, in turn, affect the ECM in various ways (Fig. 1.2). [M. Petreaca and M. Martins-Green, 2007]. Therefore the importance of ECM in tissue organization and function is both structural and functional.

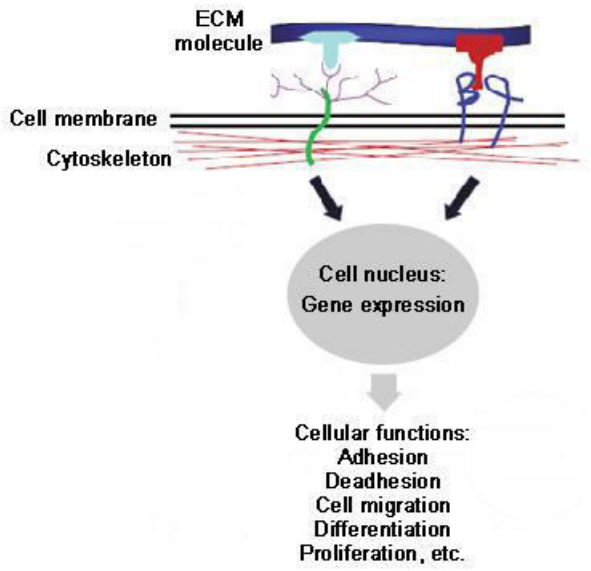

Figure 1.2: Schematic illustration of cell/ECM interaction

In this respect, there is an interrelation between the distinct spatial patterns of ECM and the respective distinct patterns of cells, dictating thus tissue function. The importance of ECM architecture in cells and tissue organization is apparent from the early developmental stages. Thus, embryonic cells produce their own extracellular scaffolds by secreting many types of molecules in the surrounding space, following a well defined program of differentiation [J. Adams and F. Watt, 1993; S. Vainio and U. Muller, 1997]. The different spatial organization of these secreted molecules gives rise to a great variety of natural scaffolds where cells continue to proliferate and organize themselves in order to build up tissues and accomplish all their natural functions [F. Rosso *et al.*, 2004]. Furthermore, there are many examples of oriented ECM in various tissues during many physiological states. Such an example includes blood vessels, which have a distinct structural organization that provides both flexibility

(resilience) and tensile strength properties. These properties are necessary for the pulsatile flow of blood. Vascular smooth mucle cells (SMCs) are circumferentially arranged in the form of fibrous helix within vascular media, collagen fibers, stacked between bands of elastin, and discontinuous sheets of endothelial basement membrane. Following this alignment, the intracellular contractile protein is fully exploited so that maximal vessel contraction and therefore dilation occurs over a comparatively small range of shorting and lengthening of vascular SMCs, respectively [Y. Li *et al*, 2014]. Fig. 1.3A shows the complex 3D texture of the basement membrane of aortic endothelial cell in the nanometer range [D.-H. Kim *et al.,* 2012]. Another example is in heart muscles, where native ventricular myocardium is composed of sheets of aligned cardiac fibers and myocytes with multi-surface orientation, varying as a function of transmural location. Fig. 1.3B illustrates this structural organization of the myocardium which is correlated with matrix fibers aligned in parallel. This structural spatial distribution of cell alignment leads to a large degree of mechanical anisotropy of the cardiac fibers, which is critical for their strong ductility during heart beating [Y. Li *et al*, 2014].

In order to emphasize the interrelation between the tissue structure and the tissue function, an insight into the respective state during pathological conditions must be provided. A correlation between tissue architecture perturbation and loss of structural organization of ECM features can be demonstrated in several pathological conditions. For example, in hypertrophic cardiomyopathy, there is a random arrangement of cardiac fibers with grossly hypertrophied, thick, short and fragmented features. Furthermore, loss of cell polarity is involved in many human disease processes, including cancer metastasis. These conditions involve common ECM remodelling [D.-H. Kim *et al*., 2012].

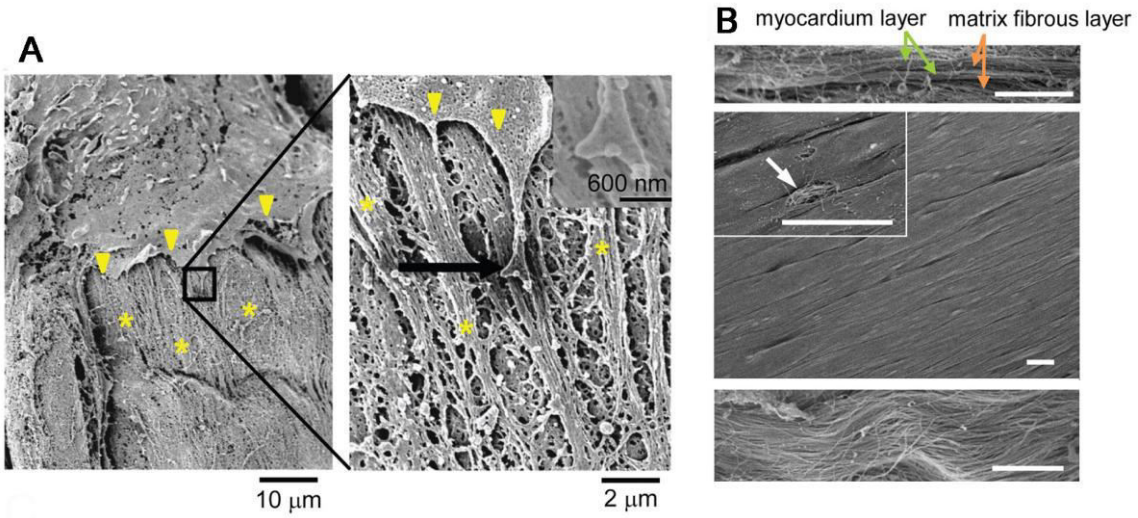

Figure 1.3: Anatomical features of highly oriented ECM in various tissues. (A) SEM images showing interaction of an aortic endothelial cell with the basement membranes in an intact vessel. The left image shows the edges of the cell membrane (arrowheads) interacting with the rough ECM structures forming the basement membrane (asterisks). The boxed area marks the area that is magnified in the right image and displays an end process of the cell membrane adhering to the basement membrane. The higher magnification allows better visualization of the bumps, ridges, pits, and grooves forming the complex topography of the basement membrane. The arrow marks the area magnified in the inset (top right), which highlights the specific interaction between an end foot of the cell membrane and the nanotopography of the ECM. (B) SEM images of ex vivo myocardium of adult rat heart. The side view (top) and top view (middle) show well-aligned myocardium. The inset in the middle image and the magnified view (bottom) demonstrate that the structural organization of the myocardium correlates with matrix fibers (arrows) aligned in parallel. Bars, 10μm. [Deok-Ho Kim *et al.*, 2012]

1.2 When cell biology met microtechnology

1.2.1 The effect of topography on neuronal/cell outgrowth- Early observations

In order to study the effect of complex topographical features of 3D cell microenvironment in various tissues, new types of cell culture platforms must be developed. The cell cultures on the well established 2D flat and rigid substrates represent a common laboratory technique since the 1950s which has provided the biologists with very broad valuable information. This model however, is mainly restrained on how and under which conditions specific bioactive molecules (such as peptides, growth factors, etc.) at different concentrations or combinations can influence cellular functions. Although these experimental models have elucidated fundamental principles in cell biology, they have been unable to recapitulate the complexity of the topographical milieu of the cells and are therefore

insufficient for the study of complex topographical features of the 3D cell microenvironments in the various tissues.

The role of topography on cellular outgrowth *in vitro* has been addressed early in the 19th century. As it is shown in Fig. 1.4, already in 1914 Ross Granville Harrison cultured embryonic frog spinal neurons in a meshwork of spider web filaments and observed that these cells only extended along the solid support of the filaments. Some years later, in 1934, Paul Weiss made similar observations with embryonic chicken spinal neurons on grooves generated by brushing clotting blood and established the term ‘‘contact guidance’’, in an attempt to describe the tendency of the cells to orient themselves along anisotropic (topographical) features of the surface (such as fibers or ridges) [S. Moore and M. Sheetz, 2011]. The observations that certain physical properties of the substrate can influence cellular outgrowth and functions *in vitro*, opened a new promising research field. However, many of these early experimental situations in which contact guidance was demonstrated, were quite complex. Due to the distinct features of the substrates, it was difficult to discriminate between the effects resulting from the chemical cues and those resulting from the topographical anisotropy. More specifically, the substrates used, i.e. plasma clots, fish scales, and various grooved surfaces, were anisotropic not only in shape but also in chemistry facilitating or not cell adhesiveness [G. Dunn and J. Heath, 1976].

Therefore, there was a need to carefully and systematically study the effect of topographical cues *vis-a-vis (*bio)chemical cues. With the emergence of micro- and nanofabrication techniques, a plethora of approaches to engineering or tailoring surfaces in a controllable manner are now available [J. Voldman *et al*., 1999; T. Park and M. Shuler, 2003; H. Andersson and A. van den Berg, 2004].

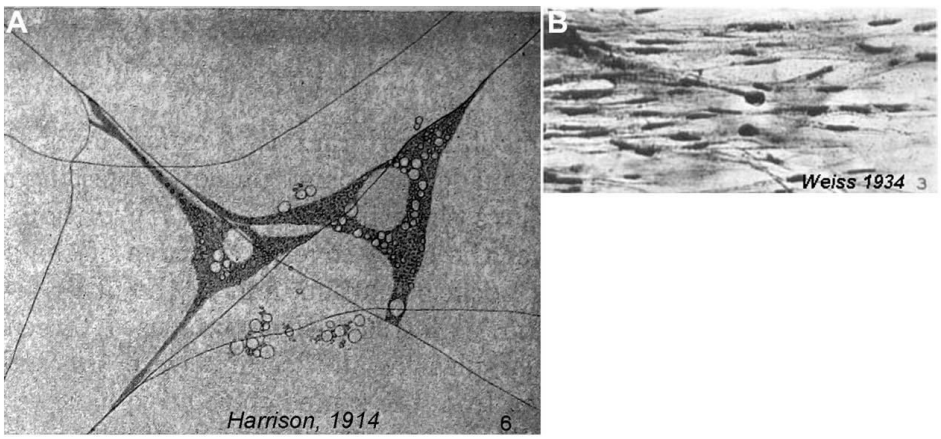

Figure 1.4: Early observations of the importance of solid substrates and contact guidance of axons. (A) Ross Granville Harrison cultured embryonic frog spinal neurons culture in a meshwork of spider web filaments and observed that these cells only extended along the solid support of the filaments. (B) When

Paul Weiss cultured embryonic chicken spinal neurons on grooves generated by brushing clotting blood, he noted that axon tended to follow the direction of these channels [S. Moore and M. Sheetz, 2011]

1.2.2 Tailoring biomaterials at different length scales

Generally, biomaterials can be tailored at three different length scales: the subcellular (<10μm), the cellular microenvironment (10-100μm) and supracellular structure (>100μm) length scale. The subcellular length scale ranges from biological recognition via cell-surface receptors (100Å), to organized subcellular structures (e.g. focal adhesions ~2-5 μm). The chemical structural properties of the cellular microenvironment directly influence many cell-fate processes. Finally, supracellular structures are important for mechanical properties of the tissue, biocompatibility, etc. [B. O. Palsson, S. and N. Bhatia, 2004]. For the study of the cellular and tissue functions at the different length scales, biomaterials can be designed to contain specific cues eliciting specific responses. For such a design, there are three critical parameters: 1. surface chemistry, 2. surface topography and 3. bulk morphology. These parameters are important at all three principal length scales. Table 1.3 summarizes these critical biomaterial parameters as to their main features, the respective cues they induce at the different lengthscales and the fabrication techniques.

More specifically, surface chemistry may influence the biological processes at the early timescales. For example, the biomaterial surface chemistry is critical for the biological response at the subcellular level by binding to specific receptors. Furthermore, it can influence cell adhesion within the implant at the cellular scale and the tissue mechanical properties of the tissue at the supracellular scale. Tailoring surface chemistry of a biomaterial can be performed via the combination of inert and/or adsorptive surfaces in two ways: 1. in a specific manner through chemical immobilization of specific functional moieties on the surface (such as proteins, peptides, etc.) and 2. in a non-specific manner by modifying surface thermodynamics (change in wettability, charge, etc.). Some common techniques used for tailoring surface chemistry are chemical immobilization, physical adsorption, molecular imprinting, peptide/protein grafting etc.

Surface topography is also important in all three principal length scales. Subcellular features can modulate cell orientation and other cellular functions. Surface topography may impact cells even far away from the surface. Both surface roughness and surface topography have a profound impact on supracellular lengthscales as well. In particular, the adhesion of the tissue-engineered constructs to the surrounding tissues is profoundly affected by surface topographical features. Tailoring the topography of a surface can be realized in the following ways: 1. by adding material, 2. by removing material, 3.

using a mold to guide surface topography, 4. using a combination of these [B. Palsson and S. Bhatia, 2004]. Some common techniques used for bulk topography tailoring are electrospinning, laser processing, micromachining, soft lithography, etc.

Regarding bulk morphology, most of biomaterial bulk modifications give rise to increase of the surface-to-volume ratio. Such increase may result in great impact both on subcellular and cellular length scale. More specifically, larger surface area implies that more proteins can be adsorbed resulting in conformational change, and exposure of additional cryptic binding sites. Therefore, novel binding sites can be presented to cell. For example, a simple increase of the pore nanoscale roughness may enhance the expression of matrix components and cell attachment [M. Stevens and J. George, 2005]. At cellular length scale the increase in surface-to-volume ratio influences not only the diffusion and mass transport of soluble molecules, such as nutrients and metabolic wastes, but also the 3dimensional (3D) cellular organization of the tissue. Tailoring the bulk topography of a surface can be realized in the following ways: 1. by expanding the material in volume, (such as in the case of hydrogels) and 2. by increasing the surface area via the insertion of pores or the creation of fiber network/ mesh. Some common techniques used for bulk topography tailoring are electrospinning, freeze drying, gas foaming, solvent casting, etc. However, it has to be emphasized that the study of the cellular and tissue responses on cues imposed by bulk topography is more complex compared to the ones induced by surface chemistry and surface topography.

Table 1.3: Main features and fabrication techniques of the critical biomaterial parameters at the different length scales.

LENGTH - SCALE	CUES - CONTROLLING PARAMETERS					
	Surface Chemistry		Surface Topography		Bulk Topography	
	Feature	Technique	Feature	Technique	Feature	Technique
Sub-cellular (<1µm)	•Bioactive chemical moieties/species (e.g. ECM molecules, GFs) •Wettability •Charge •Hydrophobicity	•Chemical immobilization •Physical adsorption •Molecular Imprinting •Peptide/Protein grafting	•**Symmetry** (e.g.orthogonal, hexagonal packing of nanopits) •**Anisotropy** (e.g. grooves, parallel fibers)	•Electrospinning •Nanolithography • Solid Free Form Fabrication	**Nanoscale** architecture: •Interconnected pores •Anisotropy •Nanofiber mesh or sponge-like • **3D**	•Electrospinning •Thermal- induced phase separation •Self-assembly of fibers (e.g. amyloid-like)
Cellular (1-100µm)	•Bioactive chemical moieties/species (e.g. ECM molecules, GFs) •Wetttability •Charge •Hydrophobicity	•Chemical immobilization •Physical adsorption •Molecular Imprinting •Peptide/Protein grafting	•**Pore** •**Symmetry** (e.g. hexagonal packing of micropits, pillars) •**Anisotropy** (e.g. Grooves, parallel aligned fibers) •**2D**	•Polymer Processing •Micromachining •Micromolding •Solid Free Form Fabrication •Electrospinning	**Microscale** Architecture: •Micropore •Microfiber mesh or sponge-like • **3D**	•Electrospinning •Gas foaming •Freeze-drying •Solid Free Form Fabrication
Supra-cellular (>100µm)	Surface hydrophobicity	•Solvent casting •Extrusion •Gradients			Macroscale Architecture	•Solvent casting •Rapid Prototyping

Abbreviations: 2/3D: two/three dimensional; ECM: Extracellular matrix;GF:Growth factor

1.3 3D micro/nano surface texturing of biomaterials as a means towards the manipulation of cell fate

1.3.1 3D micro/nano surface texturing techniques

The present work aims at tailoring biomaterial surfaces in a controllable manner. For the production of microtextured biomaterial surfaces, numerous techniques are available, ranging from simple manual scratching to more controlled fabrication methods [B. Ratner *et al*., 2004]. Accordingly, a plethora of approaches to engineer surfaces in a controllable manner have been described [J. Voldman *et al.,* 1999; T. Park and M. Shuler, 2003; H. Andersson and A. van den Berg, 2004]. Examples of these techniques are photolithography, microcontact printing, microfluidic patterning, electrospinning and self-assembly. Using these techniques 3D topographical features of tailored geometry, roughness and orientation, complemented by the desired spatial resolution at micron and submicronscales, can be realized on material surfaces of different chemical and mechanical properties [M. Stevens and J. Georg, 2005; J. Norman and T. Desai, 2006]. The main characteristics of 3D micro/submicron surface texturing techniques of biomaterials are listed in Table 1.4a,b [D. Qin *et al.*, 1998; J. Voldmann, 1999; G. Whitesides *et al.,* 2001; B. Ratner *et al.,* 2004; A.Noori *et al*. 2008 ; V.Saile, 2009; E.Stratakis *et al*., 2011]. Patterning of culture surfaces has triggered the development of new types of cell culture platforms, where the effect of topographical cues on cellular responses can be investigated [R. Flemming *et al*., 1999; C. Bettinger *et al*., 2009; E. Martínez *et al*., 2009].

Table 1.4a: Main characteristics of 3D micro/submicron surface texturing techniques of biomaterials

Technique	Principle	Material	Pattern Type	Advantages	Disadvantages
Photo-structuring: Photo-lithography	The transfer of a user-generated geometrical pattern onto a material through the selective exposure of a light sensitive polymer	Hard materials	Usually: alternating grooves and ridges	-The first step/basis for many other microfabrication techniques, such as electron beam lithography, X-ray lithography, etc. -The underlying process for all microstructuring processes in microelectronics	-Not easily applied to curved surface -Multiple step technique -Clean-room facilities & expensive equipment
Photo-structuring: Ultrashort-pulsed Laser ablation	A pulsed laser beam of high intensity at short timescale impinges on substrate. Material is vapourized or melted and ejected from surface. Pattern can happen by x-y movement of the sample, the beam or a combination of both	Broad range of materials (ceramics, metals and polymers)	Surface texturing with complex geometries including 3D shapes or structures with varying wall shapes and etch depths, and various aspect ratios on the same substrate	-Limited size of the affected volume -High fabrication rate -Noncontact interaction -Reproducibility	
Photo-structuring: Stereo-lithography	Laser beam is focused on the free surface of a photosensitive liquid to induce polymerization of the local region of liquid and to transform it to a polymerized solid.	Photocurable polymers	3D shapes or structures	-3D polymer microdevices -Simple fabrication (the structure is defined using a CAD program which allows for rapid and inexpensive prototype adjustments)	-Time consuming system -Limited range of available materials
Photo-structuring: LIGA	A hybrid fabrication technique consisting of sequentially 1.lithography, 2.electroplating and 3. molding	Wide variety: polymers, metals, alloys and ceramics	High aspect ratio microstructures	-Large structural height and sidewall properties. - Thickness ranging from 100-1000 μm. - High spatial resolution. - High aspect ratios	-High cost in some types (i.e. X-ray LIGA) - Slow process - Complicated process - Difficulty transitioning from research to production

Abbreviations: 3D: three dimensional; CAD: Computer-aided design; LIGA: German acronym for Lithographie, Galvanoformung, Abformung

Table 1.4b: Main characteristics of 3D micro/submicron surface texturing techniques of biomaterials

Technique	Principle	Material	Pattern Type	Advantages	Disadvantages
Soft lithography- Replica Molding	The replication via casting and curing of the 3D topography of a patterned, solid surface in an elastomer, usually polydimethylsiloxane (PDMS)	Hard materials	Dependence on the master and replication polymer used	-Simple and easy procedure (no need for clean room facilities) -Multiple stamps can be created from a single master -Reusability of the masters -High resolution (~100nm)	Stamp distortion
Soft lithography- Microcontact printing	The pattern transfer of the material of interest- usually self assembled monolayers (SAMs) of ink-from a PDMS stamp onto the substrate surface.	Metal substrates (mainly Au or SiO_2- coated surfaces)	Patterning of alkanethiols, proteins, silanes, polymers, etc. onto surfaces	- Simple and easy procedure -Multiple stamps can be created from a single master -Individual stamps can be used several times with minimal degradation of performance -Both flat and curved surfaces can be stamped	-Substrate contamination -Shrinking/swelling of the stamp -Ink mobility -The resolution of the printed features, depends on the concentration of the alkanethiols and the printing conditions
Etching	The creation of topographical features on a surface by selective removal of material through physical (dry etching) or chemical (wet etching) means.	Silicon, glass, plastics	Dry anisotropic etching results in a flat profile, while wet anisotropic etching results in cavities with inclined sidewalls. Isotropic etching occurs not only in the direction of depth, but also laterally, and results in a curved profile.		The desired feature dimension depends on the etch rates
Electro-spinning	Fibers are electrostatically spun into a nonwoven scaffold	Polymer solution	Fiber alignment	Good control over pore sizes and fiber diameters	Limited mechanical properties

Based on their design, the different geometries attained via patterning could be classified in two main categories: (i) continuous and (ii) discontinuous (Figure 1.5). Continuous geometries could be further classified into anisotropic, isotropic and topography-gradient topographies. Anisotropic are directionally dependent, providing cues along a single axis. Isotropic topographies are uniform in all directions, providing cues along multiple axes. Topography gradients provide cues through gradual changes in physical features (e.g., groove spacing) along a particular direction. Examples of continuous topographies are photolithographically fabricated grooved silicon substrates or electrospun polymer fibers at parallel or random orientation. Discontinuous geometries could be further classified into isotropic and topography-gradient topographies. Examples of discontinuous topographies are silicon or gold pillars or posts [D. - H. Kim et al., 2012].

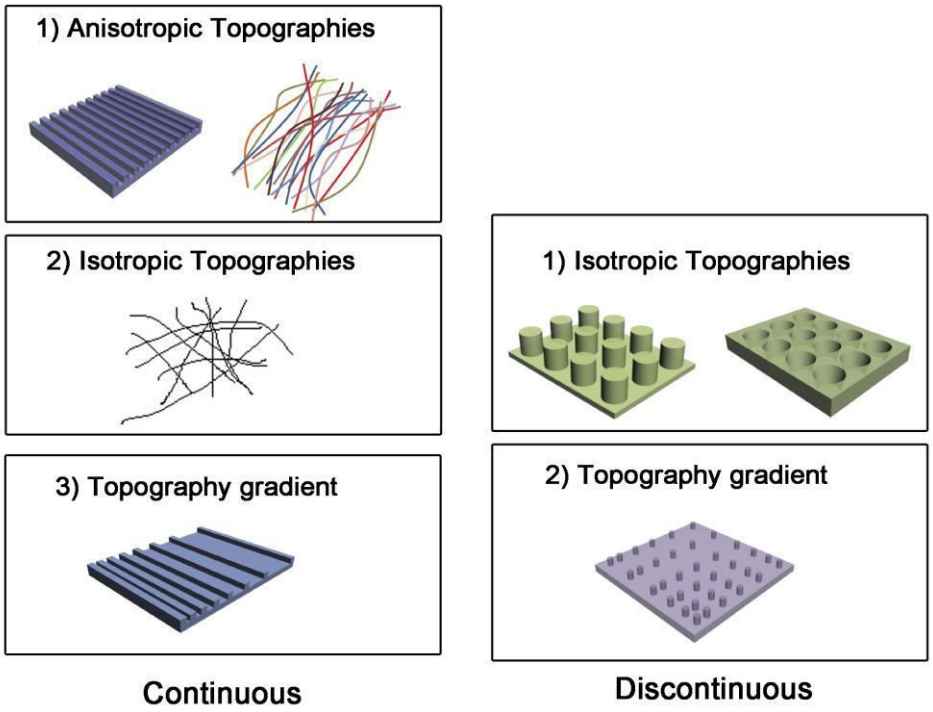

Figure 1.5: Schematic illustrations of the different geometries being used as cell culture platforms [modified from D. - H. Kim *et al.*, 2012]

1.3.2 Biomaterial surfaces and the physiological environment

A crucial consideration regarding cell/tissue-biomaterial interface is that this is a quite complex and dynamic environment. Cell interactions with surfaces appear to be mediated by proteins adsorbed from the local environment. Short time after implantation in a living system (<1 second), proteins can be observed on biomaterial surfaces. Within seconds to minutes, a monolayer of proteins adsorbs to

most surfaces. This layer, however, is not static, since during and after protein adsorption, proteins can undergo physical and chemical transformations. By the time cells reach the surface, the material has already been coated with a monolayer of proteins. Hence, the host cells do not "see" the material, but instead they "see" a dynamic layer of proteins. Since cells respond specifically to proteins, this interfacial protein film may be critical for the subsequent cell-material surface interactions [B. Ratner *et al*., 2004].

Protein adsorption occurs following the electorstatic, hydrophobic and non covalent hydrogen-bonding during solid-liquid interaction. Both biomaterial surface properties and protein properties can affect the rate, extent and mechanisms of protein adsorption to a surface. These are summarized in Table 1.5 and Table 1.6, respectively [K. Dee *et al*., 2003; B. Palsson and S. Bhatia, 2004].

Table 1.5: Properties of proteins that affect their interactions with surfaces [K. Dee *et al*., 2003]

Property	Effect
Size	Larger molecules can have more sites of contact with the surface
Charge	Molecules near their isoelectric point generally adsorb more readily
Structure Stability Unfolding rate	 Less stable proteins, such as those with less intramolecular cross-linking, can unfold to a greater extent and form more contact points with the surface Molecules that rapidly unfold can form contacts with the surface more quickly

Table 1.6: Properties of surfaces that affect their interactions with proteins [K. Dee *et al*., 2003]

Property	Effect
Topography	Greater texture exposes more surface area for interaction with proteins
Composition Hydrophobicity Hydrophilicity	Chemical makeup of a surface will determine the types of intermolecular forces governing interaction with proteins Hydrophobic surfaces tend to bind more proteins Hydrophilic surfaces tend to resist protein adsorption
Charge	Opposite charges between the surface and protein promote increased protein adsorption, while like charges tend to reduce protein adsorption
Potential	Surface potential will influence the distribution of ions in solution and interaction with proteins
Heterogeneity	Nonuniformity of surface characteristics results in domains that can interact differently with proteins

1.4 Interfacing of biomaterial surfaces with nerve cells and neural networks

With the aid of microfabrication techniques, new types of cell culture platforms with specific topographical patterns, at micro and sub-micro scale can be designed and fabricated, while maintaining a constant chemical composition. In such culture platforms, the effect of topography on the cellular

functions can be carefully and specifically investigated and/or controlled, depending on the field of interest.

In neuroscience, the control of the exact positioning and outgrowth of nerve cells and neuronal networks is very important in a wide spectrum of subfields, ranging from basic research to clinical applications. Fig. 1.6 illustrates the different possibilities arisen from exploiting the interface between neural tissue and technology. Representative examples in basic research include microfluidic/cell culture platforms for the study of separate nerve cell compartments and their biochemical function *in vitro* [A. Taylor *et al*., 2005; J. Park *et al*., 2009] addressing basic *in vitro* neuroscience questions. Another example includes multielectrode devices for stimulating and recording cultured neurons with multielectrode arrays (neurochips), in order to study the dynamics of functioning neuronal networks [M. Maher *et al*., 1999; M. Merz and P. Fromherz, 2005]. In clinical research, implantable scaffolds and electrodes, promoting *in vivo* tissue regeneration and cell stimulation or recording, respectively, have been fabricated [R. Bellamkonda, 2006; K. Ludwig *et al*., 2006]. A great variety of different geometries (alternating grooves/ridges, periodical pillars, etc.) can be now structured on different material surfaces (of different physicomechanical characteristics) and the effect of the topography on cellular functions can be investigated and controlled.

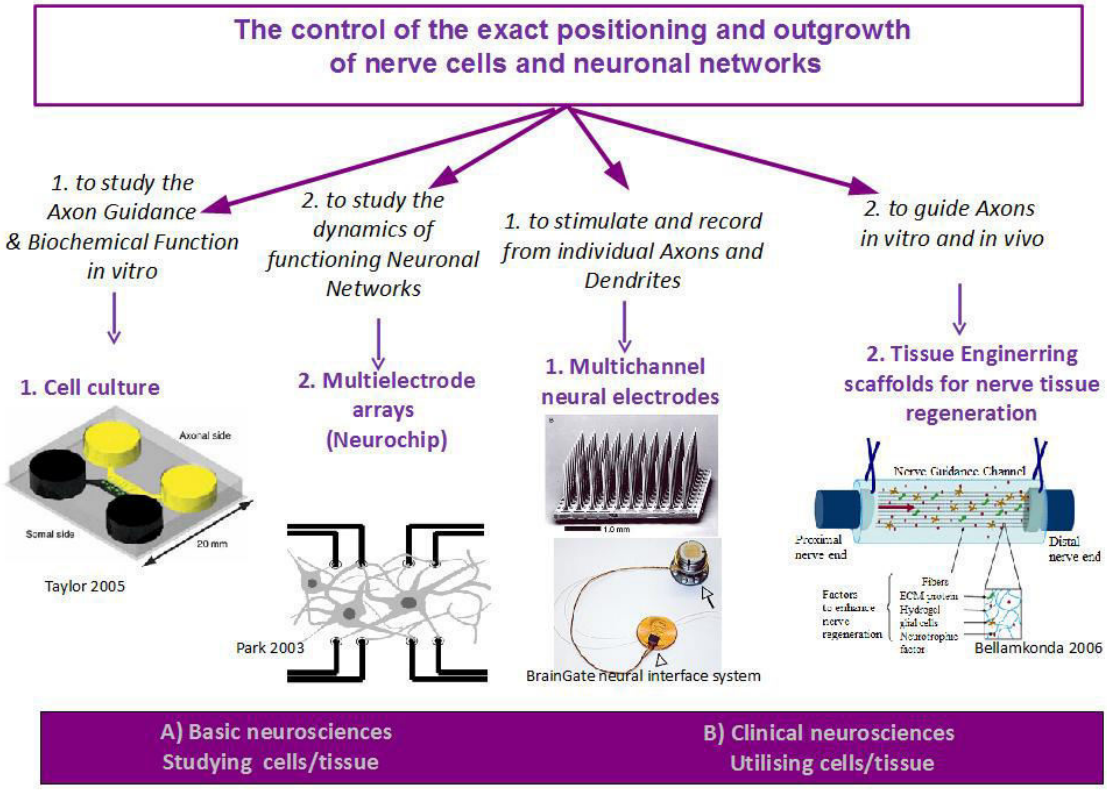

Figure 1.6: Schematic illustration of the different possibilities arisen from exploiting the interface between neural tissue and technology.

1.5 The nervous system

Since the aim of the present work was to study the effect topography of a cell culture platform on nerve cell differentiation and growth, a short introduction on the nervous system is given hereby.

1.5.1 Organization and complexity of the nervous system and nervous tissue

The nervous system has two anatomically distinct components: the central nervous system (CNS), consisting of the brain and the spinal cord, and the peripheral nervous system (PNS), composed of specialized clusters of neurons (ganglia) and peripheral nerves. The peripheral nervous system relays information to the central nervous system and executes motor commands generated in the brain and spinal cord (Fig. 1.7). The simplest action involves the integrated activity of multiple sensory, motor, and motivational pathways in the central nervous system. Each pathway contains a series of relay nuclei and each nucleus has several functional subdivisions. Most neurons are precisely arranged into functional pathways that have the same anatomical arrangement in every individual. Many pathways cross from one side of the nervous system to the other. These basic principles govern the organization of the nervous system from the spinal cord through the brain stem to the highest levels of the cerebral cortex [E. Kandel *et al*, 2000].

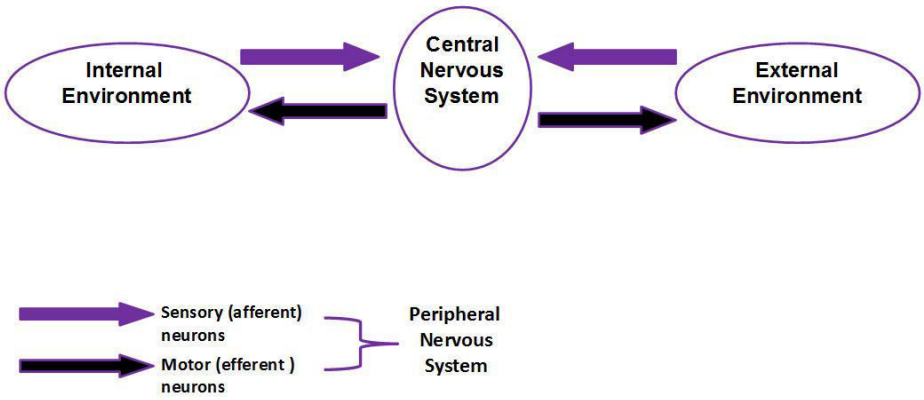

Figure 1.7: Schematic illustration of the functional interconnectivity between Central Nervous System and Peripheral Nervous system.

The peripheral nervous system is distinguished into the somatic and autonomic divisions (Fig. 1.8). The somatic division includes the sensory neurons that innervate the skin, muscles, and joints. The cell bodies of these sensory neurons lie in the dorsal root ganglia and the cranial ganglia. Receptors associated with the dorsal root and cranial ganglion cells provide sensory information to the central

nervous system about muscle and limb position and about touch and pressure at the body surface. The autonomic division of the peripheral nervous system mediates visceral sensation as well as motor control of the viscera, smooth muscles, and exocrine glands. It consists of the sympathetic, parasympathetic, and enteric systems. The sympathetic system participates in the body's response to stress, while the parasympathetic system acts to conserve body resources and restore homeostasis. The enteric nervous system controls the function of smooth muscle of the gut [E. Kandel *et al*, 2000].

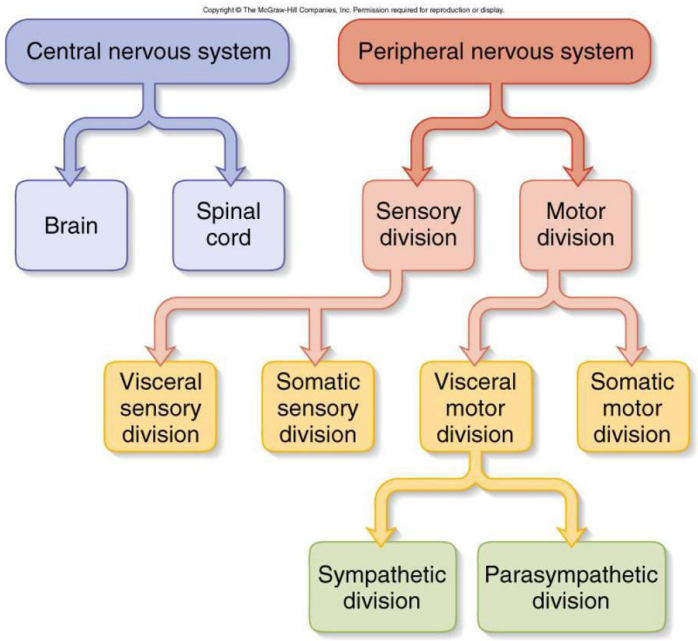

Figure 1.8: Schematic illustration of the main subdivisions of the nervous system (NS) [http://javiciencias.blogspot.gr/2014_05_01_archive.html]

Unlike other tissues, where cells have simple shapes and fit into a single field of the light microscope, the nervous tissue is a complex three-dimensional environment whose topographical features span a large spectrum of morphologies and size scales. Cell bodies vary greatly in size between the different cell types; however, in the vertebrate nervous system, they typically have diameters in the range of 10 μm (10–50 μm), whereas axons and dendrites have diameters in the micrometer range (typically, 0.2–3 μm). Although the smallest neurons can be some microns in diameter, there are neurons that have processes that extend over considerable distances [E. Kandel *et al.*, 2000]. Figure 1.9 illustrates the broad shape diversity of the two main cell types of the nervous tissue: neurons and neuroglia. The great diversity in morphologies is accompanied by a wide functional diversity (Table 1.7).

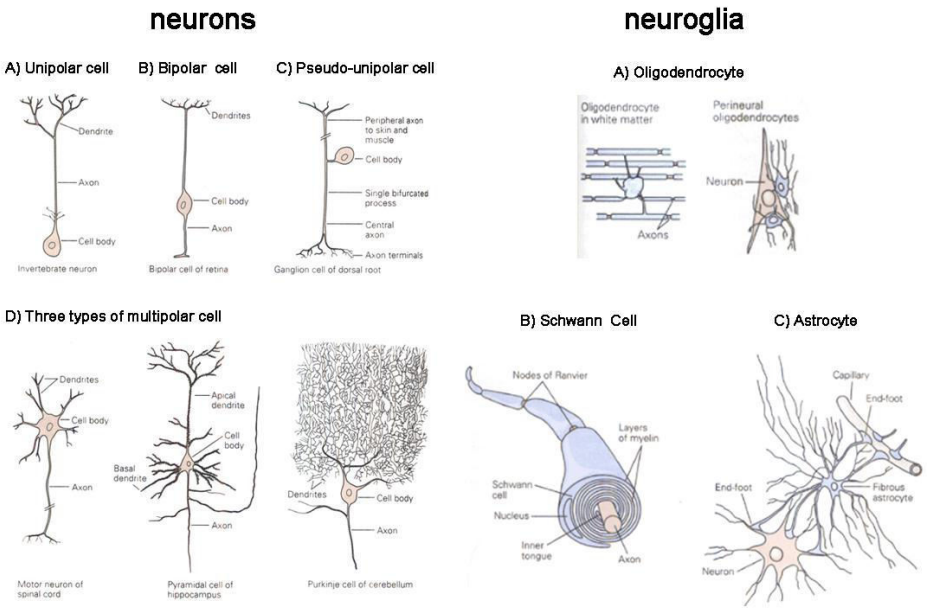

Figure 1.9: The broad shape diversity of the two main cell types of the nervous tissue: neurons and neuroglia [E. Kandel *et al*., 2000]

Table 1.7: The basic functions of the neurons and neuroglial cells.

Neurons (CNS: pyramidal cells PNS: sensory, sympathetic neurons)	**Neuroglia** (CNS: oligodendrocytes, astrocytes PNS: Schwann cells)
are the basic structural and functional units of the nervous system (the Neuron doctrine)	form myelin
The basic unit of signal transmission of the nervous system	surround neurons and hold them in place
are electrically excitable	supply nutrients and oxygen to neurons
process and transmit information by electrical and chemical signaling	destroy pathogens and remove dead neurons modulate neurotransmission

In the nervous tissue, a change in cell morphology induced by specific geometric patterns of its surroundings is correlated with emergent functions at the cellular or tissue level and is very important during early nervous system development or peripheral nerve regeneration. Such an example includes radial glia spanning the walls of the developing brain, organized into regular arrays guiding the migrating embryonic neurons [M. Hatten, 1990]. In PN regeneration, Schwann cells after lesion-

induced Wallerian degeneration, proliferate, migrate and organize themselves into longitudinal cell columns, the so called ‘‘bands of Bungner’’, which serve as a permissive substrate for the growth of regenerating peripheral nerves [M. Burnett and E. Zager, 2004; V. Ribeiro-Resende *et al*., 2009]. This procedure is illustrated in Figure 1.10.

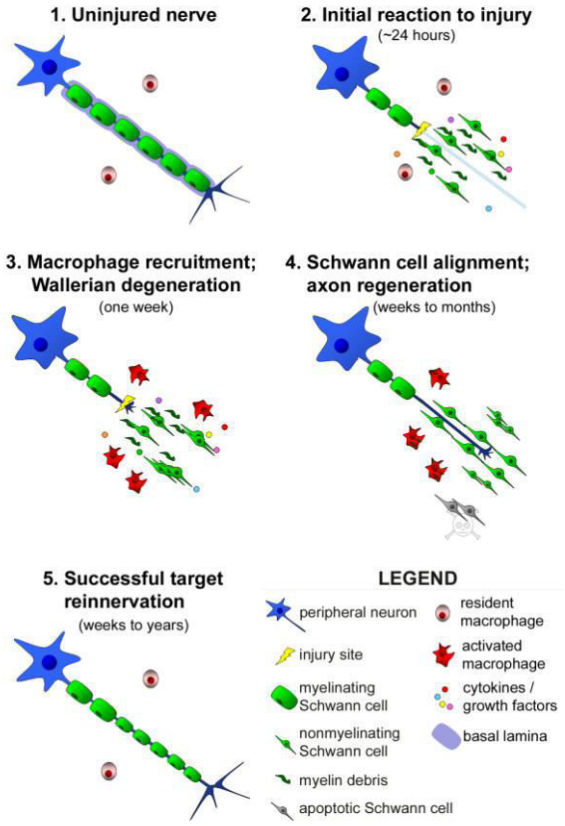

Figure 1.10: Schematic illustration of the progression of Wallerian degeneration and axon regeneration after peripheral nerve injury. A single axon with associated myelinating Schwann cells is shown. 1. The endoneurium of an uninjured nerve consists of axons, associated Schwann cells (myelinating and nonmyelinating), and resident, inactivated macrophages. 2. Soon after PNI, denervated myelinating Schwann cells release their myelin. These Schwann cells then proliferate within their basal lamina tubes, produce cytokines/trophic factors, and phagocytose detached debris. In addition, the reaction within the neuron cell body begins. 3. Wallerian degeneration is well underway within a week of injury. Soluble factors produced by Schwann cells and injured axons activate resident macrophages and lead to recruitment of hematogenous macrophages. The activated macrophages clear myelin and axon debris efficiently, and produce factors that facilitate Schwann cell migration and axon regeneration. 4. After a lag period, injured axons form a growth cone and begin to regenerate along bands of Büngner formed by Schwann cells. These tubes provide a permissive growth environment and guide extending axons towards potential peripheral targets. Schwann cells that have been chronically denervated (e.g., for a few months) are less supportive of regrowth and are more likely to undergo apoptosis. 5. If the axon is able to traverse the injury site, and its environment supports its growth along the entire distal stump, then the axon can connect with peripheral targets. [A. Gaudet *et al*., 2011]

1.5.2 Cells used for this study

For the *in vitro* assays of this study, cells with sympathetic neural phenotype (PC12 cell line and primary sympathetic neurons form Superior Cervical Ganglia), sensory (primary sensory neurons from Dorsal Root Ganglia) and neuroglial cells of PNS (Schwann cells from ischiac nerve) have been used.

The PC12 cell line was cloned in 1976 [L. Greene and A. Tischler, 1976] from a transplantable rat pheochromocytoma of adrenal medullary chromaffin cells [S. Warren and R. Chute, 1972]. The original tumor appeared in an X-irradiated male New England Deaconess Hospital-strain rat. Embryologically, chromaffin cells are derived from the sympathoadrenal (SA) lineage in the neural crest. In the rat, during migration out of the neural crest, some SA cells arrive in the adrenal anlagen around embryonic day 10.5 and are arrested there both developmentally and functionally, while other SA cells continue to migrate and differentiate eventually into sympathetic neurons [D. Anderson and R. Axel, 1986]. In the past 35 years PC12 cells have become an enormously popular model, mainly for studying fundamental mechanisms of neuronal differentiation and mechanisms of neurotransmitter synthesis and release. PC12 cells maintain some of the features of the bipotentiality of embryonic SA cells, while they are readily available and rather easy to culture. Thus, depending on the appropriate environmental cues, PC12 cells can differentiate towards either the sympathetic neuronal or the neuroendocrine, chromaffinergic pathway. For example, in the presence of neurotrophic agents, such as nerve growth factor (NGF) or brain-derived neurotrophic factor (BDNF), PC12 cells can differentiate into sympathetic neurons, whereas in the presence of glucocorticoids (and in organotypic culture) these cells acquire a neuroendocrine, chromaffin cell-like phenotype) [P. Lelkes *et al*., 2006]. As mentioned above, PC12 cells are a useful *in vitro* model to study neuronal differentiation at cellular and molecular level [G. Guroff, 1985]. They respond to several growth factors, neurotrophins, and hormones and can be used to assess distinct responses during differentiation. When stimulated, PC12 cells recapitulate several steps of neuronal differentiation as they block proliferation and extend multiple neurites. Nerve growth factor (NGF) is the classical inducer of neuronal differentiation. Without NGF, this line remains viable and retains the characteristics of the parent tissue. The cells grow in epithelial-like clumps, contain dense cored granules, and synthesize and store catecholamines. When NGF is added to the culture medium, the cells cease dividing over the period of a week and obtain the phenotype of sympathetic neurons, i.e. they begin to develop processes which are fine in caliber, varicose and fascicles and become electrically excitable. Since PC12 cells can be grown for many generations in the absence of NGF, the formation of processes must involve a *de novo* production rather than a

regeneration of existing processes [L. Greene and A. Tischler, 1976; L. Luckenbill – Edds *et al*., 1979 ; D. Vaudry *et al*., 2002].

The superior cervical ganglia (SCG) contain sympathetic neurons. These neurons provide sympathetic innervations for the head and neck regions and they constitute a well-characterized and relatively homogeneous population. Sympathetic neurons are dependent on NGF for survival, differentiation and axonal growth. Cultured sympathetic neurons have been utilized in studies of neuronal development and differentiation, mechanisms of programmed and pathological cell death and signal transduction studies [N. Zareen and L. Greene, 2009]. Studies of axonal elongation, substrate requirements, and molecular interactions, underlying neurite extension and ensheathment, have utilized explants; other experiments on dendrite growth, cell death, and neurotransmitter changes have used dissociated, even isolated, single neurons, depending on the question being asked [M. Johnson, 2001].

Dorsal root ganglia (DRG) are ball-shaped clusters of sensory nerve bodies, axons, Schwann cells and fibroblasts, which are located posterolateral to the spinal cord. The neurons in the DRG project axons to the periphery and into the spinal cord, thereby forming a relay system for sensory information from skin and muscle. DRGs have proven of great use in modern neurobiology and cell biology. The DRG is a reliable and robust model system for studying sensory neurons in a variety of conditions. Furthermore, because of DRG axon projection from the periphery into the spinal cord, the system is useful research models for spinal cord injury and recovery. Depending on the experiment, explants or dissociated cells can be used. Axons extend radially from explanted DRG, forming a "halo." On the other hand, dissociated DRG cells allow investigation of cellular mechanisms acting throughout the neurons [P. Lelkes *et al*., 2006].

Schwann cells are the glial cells of the peripheral nerve trunks. Part of this housing function is the formation of an interface between the neural and surrounding tissues. Thus, around each axon-Schwann cell unit an invariable basal lamina delineates the border with adjacent connective tissue components. This arrangement allows a peripheral nerve to contain considerable amounts of connective tissue providing the requisite physical strength, while retaining tubular channels for the delicate nerve fibers. In addition to this function, Schwann cells form myelin sheaths along the larger nerve fibers. Schwann cell populations for the ventral nerve roots are provided from neural crest cells migrating ventrally along the lateral aspect of the neural tube. Schwann cells maintain the ability to dedifferentiate following injury, and to proliferate, providing additional Schwann cells for the regenerative process [H. Kettenmann and B. Ransom, 1995]. In this context, they are useful in studies of myelination and peripheral nerve regeneration. The study of Schwann cell functions has been

facilitated by the availability to isolate and establish pure population of primary Schwann cells. The most widely used method of preparing Schwann cell culture uses primary sciatic nerves of new-born rats. The procedure is relatively simple and yields a highly purified population of Schwann cells in a short period of time [H. Kim and P. Maurel, 2010]

1.6 The effects of artificial micro- and nanotopographical features on nerve cell morphology

In order to address different questions regarding the effect of topography on cellular functions, different cell assays have been used. These range from cell adhesion and orientation assays to more complex functional assays, such as cell proliferation and differentiation on the different substrates [E. Martinez *et al*., 2009]. Many studies report the response of cell types, like fibroblasts or osteoblasts which do not form extensive processes [E. Martinez *et al*., 2009]. In these cell types the underlying topographical cue rearranges and reorganizes the cytoskeleton of the whole cell. In nerve cells the response seems quite distinct, mainly due to their unique morphology. The neuron consists of a network of processes called neurites (axons and dendrites), which extend from the cell body. When cultured on different substrates, the neurons have been shown to rearrange their network shape according to the imposed topography, while the cell body does not necessarily follow a similar adjustment. In case of co-cultures, neurons have been shown to follow the topography of glial cells [D. Thompson and H. Buttner, 2006].

Different assays have been generally used to evaluate the responses of nerve cells depending on the substrate topography. These have been very thoroughly reviewed by *D. Hoffman -Kim et al.* [D. Hoffman-Kim *et al*., 2010]. Regarding differentiation of dissociated cells, the cellular assays applied include measuring of the number of cells forming neurites [J. Foley *et al*., 2005], the neurite density, i.e. the number of neurites per cell [M. Mahoney *et al*., 2005; F. Haq *et al*., 2007; W. Su *et al*., 2013], the length of the longest neurite [K. Das *et al*., 2004; N. Gomez *et al*., 2007], and the total neurite extension length [S. Koh *et al*., 2008]. In studies using whole explants the neurite outgrowth and the Schwann cell migration have been evaluated [E. Schnell *et al*, 2007; A. Hurtado *et al*., 2011; V. Mukhatyar *et al*. 2011]. These have been quantified via measuring the longest distance relative to the explant edge at which the neurite and the Schwann cell have been outgrown and migrated, respectively. An additional assay quantifying the directed outgrowth, which is critical in repair strategies for damaged peripheral nerves, includes the evaluation of somal, nuclear or neurite alignment relative to the directive topographical cues.

The neuronal response to different continuous and discontinuous topographies (according to the division presented at 1.3.1) used in the literature is summarized in Tables 1.8 and 1.9, respectively, where the different approaches (regarding the material, fabrication technique, cell type and cell assay being used) and the respective nerve cell responses are presented.

Table 1.8a: The effects of artificial micro- and nanotopographical features on nerve cell morphology /response- **Continuous Geometries**

Feature Type	Biomaterial / Fabrication Technique	Feature dimensions	Cell type / Cell assay	Cellular response	Reference
Grooves	Fused quartz / Electron beam lithography	Depth: 14 -1.100 nm Width: 1, 2 or 4 µm	Dissociated embryonic *Xenopus* spinal cord neurons and rat hippocampal neurons / Neurite growth	Effect of species: Xenopus neurites grew parallel to grooves but hippocampal neurites regulated their direction of neurite growth depending on groove dimensions and developmental age. Effect of feature size (depth): Hippocampal neurites grew parallel to deep, wide grooves but perpendicular to shallow, narrow ones. Effect of developmental age: The frequency of perpendicular alignment of hippocampal neurites depended on the age of the embryos from which neurons were isolated	A. Rajnicek et al. 1997
Grooves	Tissue culture PS / Thermal nano-imprint lithography	Depth: 200 nm Width: 500,750 nm Pitch : 1000 nm	PC12 cells / Differentiation after NGF	Effect of feature size (width): increasing the width of the plateaus and grooves from 500 to 750 nm reduced PC12 neurite alignment though neurites were longer on flat and 750 nm grooved surfaces than the 500 nm surfaces.	M. Cecchini et al. 2007
Grooves	PLGA / Laser ablation	Depth: 2-3µm Width: 5,10 µm Spacing: 5, 10 µm	PC12 cells / Neurite growth	Effect of feature size: More parallel growth on small groove sizes (5 µm) than on larger groove sizes (10 µm) Preferential growth on spaces and not in grooves (probably because the PC12 cell diameter was larger than the microgroove size)	L. Yao et al. 2009
Grooves	PMMA covered Si / Nanoimprint lithography	Depth: 0.3µm Width: 0.1-0.4 µm Spacing: 0.2-2 µm	DRGs & SCGs whole explants / Axon guidance	All axons grow on ridges/ spacings and not in grooves Effect of feature size (depth): On narrow grooves/ridges the axons grew on top of several ridges simultaneously, while on wider grooves/ridges the axons were found on single ridges Effect of feature size (width): The relation of axon diameter and groove/ridge width seems to be crucial for axon.guidance	F. Johansson et al. 2006

Table 1.8b: The effects of artificial micro- and nanotopographical features on nerve cell morphology /response- **Continuous Geometries**

Feature Type	Biomaterial / Fabrication Technique	Feature dimensions	Cell type / Cell assay	Cellular response	Reference
Grooves	PDMS with immobilized NGF / Replica molding	Depth: 400, 800 nm Width: 1, 2 μm	Embryonic rat hippocampal cells (E18) / Polarization and axon length	Perpendicular or parallel contact guidance in a manner dependent on surface feature sizes Effect of feature size (depth): As depth increased, the percentage of cells growing parallel to the microchannels increased Effect of specific binding of NGF: The topographical cues had the most pronounced effect on polarization regardless of the simultaneous presence or absence of NGF. In contrast, axon length was increased by tethered NGF and not by topography, though an enhancing effect was seen when both cues were presented simultaneously, perhaps because of faster polarization due to the topography in combination with enhanced growth due to the NGF	N. Gomez et al. 2007
Grooves	PDMS / replica molding	Depth: 2.5 - 69 μm Width : 50-350μm	Murine embryonic cortical neurons / Axon Guidance	Effect of depth: Axons were found to cross over the shallow grooves of 2.5 or 4.6μm, whereas grooves 22 or 69μm caused the axons to turn after contact with the feature. However, at an intermediate depth of 11μm, about half of the axons crossed the step while the others turned in response to the cue (this behavior was correlated with the angle at which the axon approached the feature)	N. Li, A. Folch 2005
Grooves	PDMS / Replica molding	Depth: 50μm Width: 30-100 μm Spacing: 30-1000 μm	Dissociated DRGs Hippocampal neuron & Schwann Cells (SC) / Neurite bridging	Neurite bridging formation Effect of anisotropy: The majority of DRG extended neurites in a direction parallel to the groove pattern, and a subset of DRGextended neurites perpendicular to/ bridging the groove pattern. Effect of feature dimensions: As width increases, the number of bridges decreases as well (The highest numbers of bridges for $w_{gspacing}$/ w_{groove} =200/30.)	J. Goldner et al. 2006
Grooves	Copolymer 2-norbornene ethylene / Thermal nanoimprint lithography	Depth: 350 nm Width: 500 nm Spacing: 500-2000 nm	PC12 cells / Differentiation after NGF	Effect of alignment: The PC12 cells adopted a bipolar morphology. Speed and angular restriction characterizing their directional migration (on nanogratings). Thus, randomly aligned neurites were produced in all directions and migration occurred with no angular restriction.	A. Ferrari et al. 2011
Micro-channels	Photosensitive polyimide / photolithography	Depth: 11 μm Width: 20–60 μm	PC12 cells / Differentiation after NGF	Effect of feature size (width): As the width decreased, the growth orientation of the neurites was promoted in a direction parallel to channel walls and the complexity of neuronal architecture was reduced	M. Mahoney et al. 2005

Table 1.8c: The effects of artificial micro- and nanotopographical features on nerve cell morphology /response- **Continuous Geometries**

Feature Type	Biomaterial / Fabrication Technique	Feature dimensions	Cell type / Cell assay	Cellular response	Reference
Filaments	PLLA / Melt extrusion	Diameter: 375 μm	DRG whole explants / Neurite outgrowth & Schwann cell migration	Effect of anisotropy: Topography guided neurite outgrowth and SC migration, Effect of coating: Neurite outgrowth was significantly increased in the presence of LN, past the SC leading edge	N. Rangappa et al. 2000
Filament bundles	PP / Thermal extrusion	Diameter: 5, 30, 100, 200, and 500 μm.	DRG explants / Neurite outgrowth and Schwann cell migration	Effect of anisotropy: Neurites grew along the long axis of the filament bundles, regardless of the filament diameter Effect of diameter: As filament diameter decreased, the neurite outgrowth and SC migration was promoted in a direction parallel to the long axis of the lament bundles	X. Wen and P. Tresco 2006
Fibers	PLLA / Electrospinning	Diameter: 250 nm and 1.25 μm	Neonatal mouse cerebellum C17.2 stem cells (NSCs) / NSC differentiation and Neurite outgrowth	Effect of anisotropy: NSC elongation and neurite outgrowth along the fiber direction was promoted on the aligned electrospun fibers independent of the fiber diameter. Effect of fiber diameter: The rate of NSC differentiation was higher for nanofibers than that of micro fibers and was independent of the fiber alignment	F. Yang et al. 2005
Fibers	PLLA / electrospinning	Diameter: ~524 nm	E15 rat DRG explants / Neurite outgrowth	Effect of anisotropy: Ganglia were elongated in the direction of fiber alignment On aligned fibers, neurites sprouted radially but turned to align to fibers upon contact, and neurite length increased on aligned fibers relative to random and intermediate fibers Schwann cells adhering to planar glass exhibit good spreading, while those adhering to fibers elongate and become extremely narrow	J. Corey et al. 2007
Fibers	PAN-MA / Electorspinning	Diameter: 0.8μm	P1 DRG explants and dissociated SCs / Neurite outgrowth & SC migration and ECM organization	Effect of anisotropy: Aligned PAN-MA fibers influenced fibronectin distribution, and promoted aligned fibronectin network formation compared to smooth PAN-MA films. Outgrown axons extended along the fibers to significantly greater extent compared to smooth films	V. Mukhatyar et al. 2011
Fibers	PAN-MA / Electrospinning	Diameter: 400-600nm	P1 rat DRG explant/ Neurite outgrowth & Schwann cell migration	Effect of anisotropy:The majority of neurite outgrowth and Schwann cell migration from the DRGs on the aligned fiber film extended unidirectionally, parallel to the aligned fibers. On the contrary, the orientation of neurite outgrowth and Schwann cell migration on the random fiber films was randomly distributed	Y. Kim et al. 2008

Table 1.8d: The effects of artificial micro- and nanotopographical features on nerve cell morphology /response- **Continuous Geometries**

Feature Type	Biomaterial / Fabrication Technique	Feature dimensions	Cell type / Cell assay	Cellular response	Reference
Fibers	PCL and PCL/Collagen blend/ Electrospinning	Diameter: ~0.5μm	E10 chick DRG explants / Schwann cell migration and axonal outgrowth	Effect of anisotropy: The direction of neurite elongation was largely orientated in parallel with the artificial fibers.	E. Schnell et al. 2007
Fibers	Polydioxanone / Electrospinning	Diameter: ~2-3μm	E16 rat DRG explants P3 astrocytes (as glial substrate)/ Neurite outgrowth	Effect of anisotropy: DRG neurons grown on random electrospun matrices show no directional preference, whereas neurites grown on aligned matrices display directionality that mimics that of the underlying fiber orientation. • Astrocytes grown on random matrices show no directional preference, whereas astrocytes grown on aligned matrices display directionality. • DRGs cultured on a substrate of astrocytes grow more robustly and extend longer processes than when grown on a glia-free matrix	W. Chow et al. 2007

*Abbreviations: DRG: Dorsal Root Ganglion ; E18: Embryonic Day 18 ; LN: Laminin ; FN: Fibronectin ; NF: Neurofilament ; NGF: Nerve growth factor ; NSC: Neural Stemm Cell ; P1: Postnatal Day 1 ; PAN-MA: poly(acrylonitrile-co-methylacrylate ; PDMS: Polydimethylsiloxane ; PLGA: poly(lactic-co-glycolic acid) ; PLLA:poly-L-lactide ; PMMA: Poly(methyl methacrylate) ; PP: Polypropylene ; PS: Polystyrene ; SC: Schwann cell ; SCG: Superior Cervical Ganglion ; Si: Silicon

Table 1.9a: The effects of artificial micro- and nanotopographical features on nerve cell morphology /response- **Discontinuous geometries**

Feature Type	Biomaterial / Fabrication Technique	Feature dimensions	Cell type / Cell assay	Cellular response	Reference
Pillars	Single crystal Si / UV stepper lithography & deep reactive ion etching	Diameter: 400 nm, Length: 5 μm, Spacing: 0.8 - 5 μm Aspect ratio: 12:1	PC12 cells / Cell morphology	Effect of spacing: Cells exhibited polarization and alignment at 2 μm interpillar spacing	M. Bucaro et al., 2012
Square-shaped Pillars	Silicon / Photolitohgraphy	Height: 1 μm Diameter: 0.5 or 2 μm Spacing: 0.5 -5 μm	Hippocampal neurons / Dendrite & Axonal outgrowth (orientation & length)	Effect of spacing: The neurites tended to span the smallest distance between pillars, aligning either at 0° or 90°, with the highest alignment with the larger pillars at the smallest spacing. As the spacing between pillars increased, the fidelity of alignment decreased, and at 4.5 μm spacing, the distribution of neuronal arbor was similar to that found on a flat surface.	N. Dowell-Mesfin et al., 2004
Conical-shaped pillars	Single crystal Si / Femtosecond pulsed laser processing	Height: ~1-2 μm	Embryonic mouse brain cells/ Cell outgrowth & network formation	Effect of surface roughness: Although only a few neurons survived on the flat substrate, the neurons on the pillars formed an elaborate web of cytoplasmic processes in the absence of glial elements.	E. Papadopoulou et al., 2010
Conical Posts	PDMS posts on glass / Masterless soft lithography transfer method	Diameter: 10-100 μm Edge to edge spacing: 10-200 μm Height: ~ 1/10(diameter)	Hippocampal neurons / Neuron process outgrowth	Effect of feature size (diameter): On surfaces with smaller features and smaller spacings, processes aligned and connected in straight lines between adjacent pillars and mostly followed a single direction by occasionally branching in the perpendicular direction. However, as feature diameters started to increase, neurites would wrap around the post they were already on, especially as the spacing increased past 40 μm. Effect of spacing: Spacing of 200 μm promoted both random outgrowth and wrapping, and flat surfaces promote random outgrowth. Therefore, as the feature size and spacing was increased, a transition from aligned outgrowth to process wrapping to random growth occured in parallel.	J. Hanson et al., 2009

Table 1.9b: The effects of artificial micro- and nanotopographical features on nerve cell morphology /response- **Discontinuous geometries**

Feature Type	Biomaterial / Fabrication Technique	Feature dimensions	Cell type / Cell assay	Cellular response	Reference
Pillars	Gallium phosphide / Chemical vapor deposition	Diameter: 50 nm Height: 2.5 μm	DRG neurons /Neuronal growth	Effect of topography: Neuronal survival relative to control surfaces with no topography was increased, and the neurons underwent complex interactions with the nanowires, such as pulling on and bending them.	W. Hällström et al., 2007
Pillars & Pores	Gold / Electrodeposition	Pillars diameter: 200 nm spacing: 70 nm height: 2 μm Pores diameter: 200 nm spacing: ~40 nm depth: 35 μm	PC12 cells / Differentiation after NGF	Effect of feature size: Features of nanosize (pillars & pores) inhibited or limited neurite outgrowth of PC12 cells compared to smooth substrates	F. Haq et al., 2007
Nano-roughness	Single crystal Si / Chemical etching	Ra: 18, 64 & 204 nm	Embryonic rat cortical neurons/ Cell adherence	Effect of nanoroughness: Unimodal cell response (an intermediate value of Ra = 64 nm promoted an optimal response, and both higher and lower roughness reduced this response)	S. Khan et al., 2005
Nano-roughness	Single crystal Si / Chemical etching	Ra: 2-810 nm	Substantia Nigra neurons/ Cell adherence and viability	Effect of nanoroughness: Unimodal cell response (an intermediate value range of Ra = 20-50 nm promoted an optimal response, and both higher and lower roughness reduced this response)	Y. Fan et al., 2002
Nano-roughness	Titanium nitride films / 1.Pulsed DC magnetron reactive sputtering 2. unbalanced magnetron ion plating	Ra : 1.3 - 5.6 nm	Primary hippocampal neurons/ Cell proliferation, attachment & morphology	Effect of nanoroughness: Reduced attachment of neurons relative to PDL coated glass.	L. Cyster et al., 2004

*Abbreviations: DRG: Dorsal Root Ganglion ; NGF: Nerve growth factor ; PDL: Poly- D - lysine ; Ra : Profile roughness parameter ; Si: Silicon

1.7 Silicon-based cell culture platforms fabricated via ultrashort-pulsed laser processing

Silicon-based microfabricated culture substrates with well-defined topographies have been extensively developed in order to create neuronal interfaces for a variety of applications [T. Pearce and J. Williams, 2007]. Representative examples include the development of grooved surfaces for the study of polarity [A. Ferrari *et al*., 2011; J. Foley *et al*., 2005], microfluidic culture platforms for the study of biochemical functionality of different nerve cell compartments *in vitro* [A. Taylor *et al*., 2005; J. Park *et al*., 2009], and multielectrode devices (neurochips) to monitor the electrical activity of functional neuronal networks [M. Maher *et al*., 1999; M. Merz and P. Fromherz, 2005].

1.7.1 Silicon

Silicon (Si) is the most common material in microfabrication, since it can readily be used in the fabrication of integrated circuits. In addition to its excellent electrical properties, silicon also exhibits outstanding mechanical properties, enabling the design of micromechanical structures, as reviewed by *K. Petersen* in the beginning of 1980's [K. Petersen, 1982]. There exists a wide range of silicon-based micromachines, which in combination with the integrated-circuit (IC) fabrication can potentially lead to monolithically integrated microsystems. Nowadays the use of silicon has been established in the commercial fabrication of many mechanical components, such as switches, filters, oscillators, fluidistic devices, medical and biochips, microphones, accelerometers, gyroscopes, flow detectors, micromirrors, and cantilever sensors [J. Voldman *et al*., 1999; P. Sievila, 2013].

Silicon is used either as bulk material or as a thin film. Bulk silicon is polycrystalline silicon (polysilicon) that is converted into single crystalline ingots via Czochralski or float-zoning methods. Thin-film silicon - including epitaxial, amorphous, and polysilicon layers - is produced by various chemical-vapor-deposition processes during the fabrication of devices [L. Hunt, 1990]. The different properties of single crystal, polycrystalline and amorphous silicon, which dictate their respective application, are mainly interrelated with the different crystal structure. Schematically the three forms of silicon are illustrated in Figure 1.11.

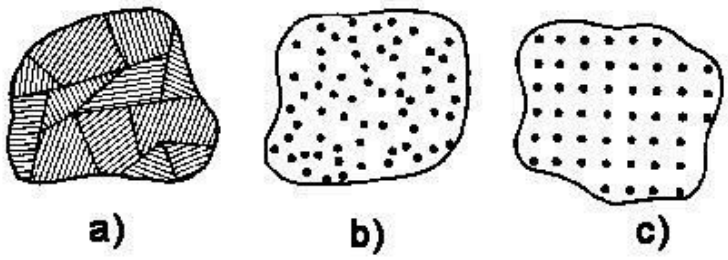

Figure 1.11: Different forms of silicon, based on crystal structure. a) Polycrystalline, b) amorphous and c) single-crystal

Single crystal or monocrystalline silicon has an ordered crystal structure, composed of a continuous crystal lattice. All lattice planes and lattice directions are described by a mathematical description known as the Miller Index. In the cubic lattice system, the direction [hkl] defines a vector direction normal to surface of a particular plane or facet. Figure 1.12 shows the three common types used in semiconductor research, i.e. [100], [110], [111]. Monocrystalline is opposed to amorphous silicon, in which the atomic order is limited to a short range order only.

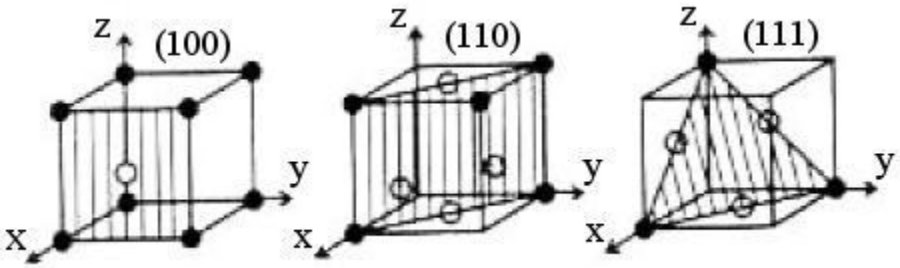

Figure 1.12: Three different crystal orientation of single-crystal silicon: [100], [110] and [111] [S. M. Sze, 2002].

Polycrystalline silicon is composed of a large number of small randomly oriented crystals or grains. The boundary separating two small grains or crystals having different crystallographic orientations imposes an interfacial defect. This leads to higher chemical reactivity in these regions.

Semiconductor surfaces have been investigated for many years. The principal reasons for dominance of silicon and metal–oxide–semiconductor (MOS) structures in IC industry is good electronic properties of SiO_2 as well as Si/ SiO_2 interface. In contrast to other materials which suffer from one or more problems, SiO_2 offers a lot of desired characteristics and advantages [A. Hierlemann]:

1. Excellent electrical insulator with a high dielectric strength and wide band gap (Resistivity > 1×10^{20} Ωcm , Energy Gap ~ 9 eV)

2. High breakdown electric field (> 10MV/cm)
3. Dielectric constant SiO_2: 3.9 (whereas Si_3N_4 : 7; Si: 11.9)
4. Stable and reproducible SiO_2 interface
5. Conformal oxide growth on exposed Si surface
6. SiO_2 good diffusion mask for common dopants: B, P, As, Sb
7. Very good etching selectivity between Si and SiO_2
8. SiO_2 has a high-temperature stability (up to 1600^oC)

According to these unique properties of SiO_2 and Si/ SiO_2 interface, silicon oxide can form a high quality electrically insulating layer on the silicon surface, serving as a dielectric in numerous devices that can also be a preferential masking layer in many steps during device fabrication.

There are several techniques to form oxide layers, namely thermal oxidation, wet anodization, chemical vapor deposition, and plasma oxidation. Among the four techniques, *thermal oxidation* in a resistance-heated oxidation furnace tends to yield the cleanest oxide layer with the least amount of interfacial defects. Thermal oxidation of Silicon can be performed in two ways: 1. Dry and 2. Wet oxidation process. 1. Dry process uses dry oxygen. The oxidation process is slow, e.g., 50 nm/h at 1000 °C and therefore is mainly used for high-precision thin oxide layers (such as gate oxide). The chemical reaction describing thermal oxidation of silicon in dry oxygen is:

$$Si\ (solid) + O_2\ (gas) \rightarrow SiO_2\ (solid)$$

2. Wet process uses (pyrogenic) water vapor. The oxidation process is fast, e.g., 400 nm/h at 1000°C and therefore is mainly used for thick oxide formation applications. The chemical reaction is the following:

$$Si\ (solid) + 2H_2O\ (gas) \rightarrow SiO_2\ (solid) + 2H_2\ (gas)$$

During the course of the oxidation process, oxygen or water molecules diffuse through the surface oxide into the silicon substrate, and the Si- SiO_2 migrates into the silicon. Therefore, during the oxide evolution, silicon from the wafer is consumed, but the total thickness (Si + oxide) increases (Fig. 1.13).

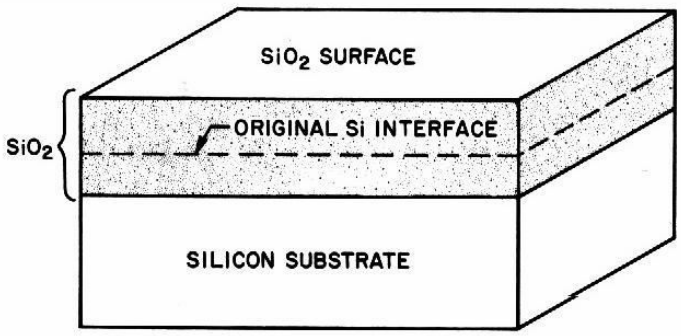

Figure 1.13: Schematic of the thermal oxide (SiO_2) formation [S. M. Sze, 2002]

A model elucidating the kinetics of oxide growth has been developed by Deal and Grove [B. Deal and A. Grove, 1965], where it is assumed that oxidation proceeds by an inward movement of the oxidant species rather than an outward movement of silicon. The transported species must go through the following stages: 1. It is transported from the bulk of the oxidizing gas to the outer surface where it reacts or is adsorbed, 2. It is transported across the oxide film towards the silicon and 3. It reacts at the silicon surface to form a new layer of SiO_2. The detailed description of the model and its equations, are analyzed by *B. Deal and A. Grove*, 1965. The model is generally valid for temperatures between 700 and 1300^{o}C, partial pressure between 0.2 and 1.0 atmosphere, and oxide thickness between 30 nm and 2000 nm for oxygen and water ambients. The model is valid for (111), (100) single crystal silicon, and polysilicon. According to the equations of this model, oxidation rate charts (different for dry and wet oxidation) have been developed, based on which, a prediction of the oxide thickness layer for the optimum oxidation parameters can be done.

Regarding its structure, SiO_2 can be described as a three-dimensional network constructed from tetrahedral cells, with four oxygen atoms surrounding a silicon atom (Fig. 1.14a). The silicon atoms are in the center of each of the tetrahedra. The length of a Si-O bond is 0.162nm and the normal distance between oxygen ions is 0.262 nm. The Si-Si bond distance depends on the particular form of SiO_2 and is about 0.31nm. The six-membered ring structure of SiO_2 is presented in Figure 1.14b. In an ideal network the vertices of the tetrahedra are joined by a common oxygen atom called bridging oxygen (i.e. O atoms that bond to two silicon atoms).

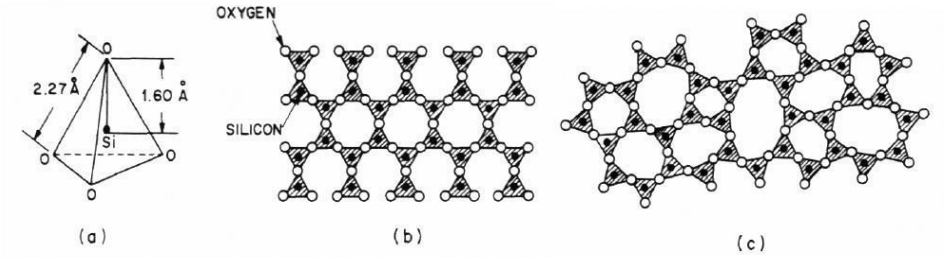

Figure 1.14: a) Structural unit of SiO_2 b) Quartz crystal lattice (2D), c) Amoprhous SiO_2 (2D) [A. Hierlemann]

In the amorphous forms of SiO_2 (Figure 1.14c), some non-bridging oxygen atoms can also exist. These phases are often named, fused silica. Crystalline forms of SiO_2, such as quartz contain only binding oxygen bonds. The various crystalline and amorphous forms of SiO_2 arise because of the ability of the bridging oxygen bonds to rotate, allowing the position of one tetrahedron to move with respect to its neighbors. This same rotation allows the material to lose long-range order and hence become amorphous. The rotation and the capability to vary the angle of the Si-O-Si bond from 120^o to 180^o with only a little change in energy play an important role in matching amorphous SiO_2 with crystalline silicon without breaking bonds. Dry oxides having larger ratio of bridging to non-bridging sites as compared to wet oxides, are thus "more stable".

The chemical bonding configurations are important basis for understanding the electronic states of the fabricated silicon oxides. In order to understand the chemical and electronic structures of the Si-SiO_2 interface, the Si-SiO_2 interface has been studied by various techniques such as high energy ion backscattering, high resolution electron microscopy, Auger electron spectroscopy and X-ray photoelectron spectroscopy (XPS) [H. Ibach and J. E. Rowe, 1974; G. Queirolo *et al.*, 1988; M. Ulrich *et al.,* 2006; C. Logofatu, 2011] . Nonstoichiometric transition regions in thermally grown ultra thin oxide films have been identified by XPS. The oxide formation evolution has been investigated using measurements of Si_{2p} photoelectron spectra [F. Jolly *et al*., 2001].

According to literature, the evolution of the oxide formation on silicon is as follows (Figure 1.15): the Si_{2p} core level spectrum of a clean silicon crystal (before any thermal treatment) shows at the beginning one distinct peak in the region of approximately 100.0 eV. As the oxide layer is formed, this Si_{2p} attributed to the Si bulk (Si^0) is decreased, while a second peak shifted towards higher binding energies (B.E.) is evolved. The shift in the silicon core-level B.E.s varies continuously from ~2.4 to 4.2 eV, until a stable SiO_2 film is formed [G. Hollinger *et al*., 1975]. These intermediate shifts are attributed to suboxides of the interface between bulk silicon and SiO_2. The suboxide states, usually denoted Si^{+1},

Si^{+2}, Si^{+3}, correspond then to a silicon atom surrounded by an increasing number of oxygen ligands, varying from one to three. While the oxide layer grows, it is progressively less and less influenced by the properties of the interface. At the end of the oxide formation, the oxide films exhibit only the XPS shift characteristic of bulk SiO_2 in the region of approximately 104.0 eV.

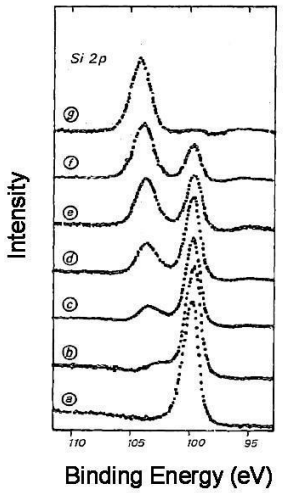

Figure 1.15: Si2p XPS spectrum of thermally grown oxides on silicon monocrystals at some different stages of oxidation. a denotes the clean crystal. b-g denote the following timepoints: 30s, 1min, 2min, 10min, 30min, 60min [G. Hollinger *et al*., 1975]

Another important issue when dealing with silicon is the so called *native oxide layer*, which is built up on the surface when a clean Si surface is exposed to atmosphere at room temperature. It is of great importance, because it has been pointed out that this may influence the thermal oxidation kinetics. Thus, the existence of a native oxide film on silicon surfaces degrades the control ability of quality of the device fabrication processings and the performance and reliability of semiconductor devices themselves.

The native oxide on silicon surfaces has a varying composition with depth, gradually changing from a highly oxidized, near stoichiometric state at the surface to a silicon rich phase, near the interface. The Si atoms in the interface are displaced with respect to their normal bulk lattice sites. The interface between the oxide and their underlying structure consists of layers of Si atoms displaced from their normal lattice sites. Figure 1.16 illustrates the Si_{2p} XPS spectra of native oxide of Si in air and in ultrapure water [M. Morita *et al*., 1990]. There are two major peaks. The Si_{2p} at lower binding energies (B.E.) is attributed to Si bulk (Si^0) and the second peak is attributed to silicon dioxide (Si^{+4}). Furthermore, the small hill present between the peaks at positions ~99.3eV and ~103.5eV, indicates that

suboxides are very likely to be present in this sample. Comparing the two conditions responsible for the native oxide formation, the binding energy of SiO_2 peak for the native oxide in ultrapure water is higher than that in the air. The intensity of the suboxide (SiO bond) at the oxide-Si interface for the native oxide in ultrapure water is smaller than that in air.

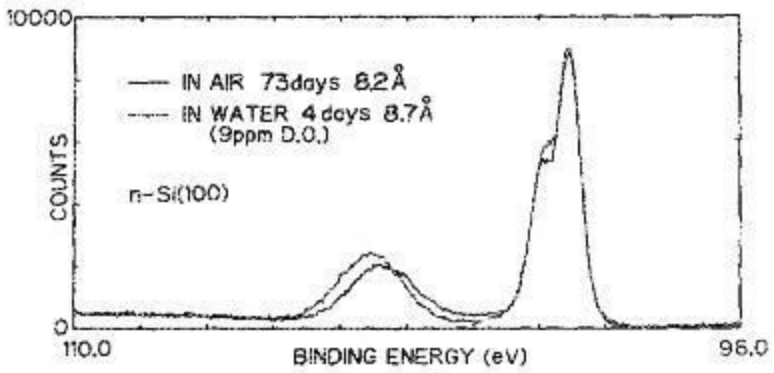

Figure 1.16: Si_{2p} XPS spectra of native oxide on Si in air and in ultrapure water [M. Morita *et al*., 1990].

The oxidation mechanism of Si in air at room temperature (RT) is entirely different from the thermal oxidation mechanism. The following model [M. Morita *et al*., 1990] is proposed for the oxidation of Si at room temperature (Figure 1.17):

1. Si atoms at a cleaned wafer surface are terminated by hydrogen (Fig. 1.17a).

2. The oxygen species (O or OH from water) are expected to break preferentially the Si_{bulk}=$Si_s(-H)_2$ backbonds rather than the Si_s-H bonds on the surface at the initial stage. (Si_{bulk-} -O-$Si(-H)_2$ bonds are formed- Fig. 1.17b).

3. After all Si atoms of the top layer are oxidized, the Si_{bulk}≡ Si_{bulk}-O backbonds of the 2nd monolayer are broken by subsequent insertion of O_2 (Fig. 1.17d).

4. In this way, a *layer-by layer growth* of the native oxide film takes place on Si surfaces exposed to air at RT.

5. The overlayer structure converts to the amorphous phase.

6. The remaining O-Si-$(H)_2$ bonds on top layer cause hydrophobic behavior of the surface, which can be observed during the initial phase of native oxidation in air.

7. The Si-H bonds on the surface are oxidized only after completion of the backbond oxidation, and silanol groups SiOH are respectively formed, which introduce polarity (and the surface becomes less hydrophobic.)

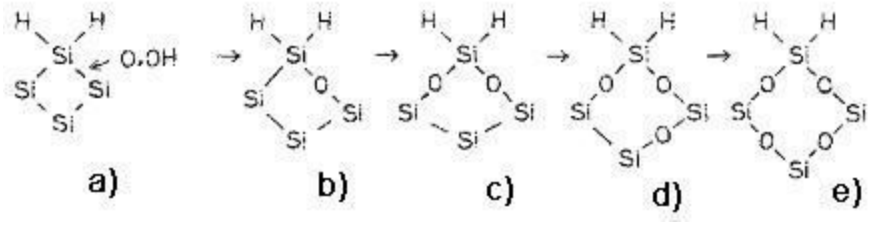

Figure 1.17: A model of native oxide growth in air [M. Morita *et al*., 1990]

1.7.2 (Pulsed) laser processing: Fundamentals of laser-matter interaction

From the earliest work with pulsed ruby lasers, it has been understood that the unique interaction of laser light with a material can lead to permanent changes in the material's properties not easily achievable through other means. Laser irradiation has been shown to induce changes to the local chemistry, the local crystal structure, and the local morphology, all of which affect how the material behaves in a given application [M. Brown and C. Arnold, 2010]

In order to understand and control the material response after/upon laser irradiation, the laser-matter interactions have to be taken into consideration. These could be summarized as follows: 1) The deposition of a certain amount of laser energy induces 2) carrier excitation. 3) The deposited energy is then redistributed through a number of processes which eventually end in the 4) structural modification of the material. Focusing on semiconductors, like silicon, the initial interaction of laser pulses with a semiconducting material is the excitation of electrons; upon photon absorption electrons are excited from their equilibrium states into higher-lying unoccupied states. The initial electronic excitation is followed by a complex hierarchy of secondary processes. The excited electrons relax and the deposited energy is redistributed through a number of processes which eventually end in the structural modification of the material. Four regimes with different timescales can be distinguished and are illustrated in Fig. 1.18 [S. Sundaram and E. Mazur, 2002].

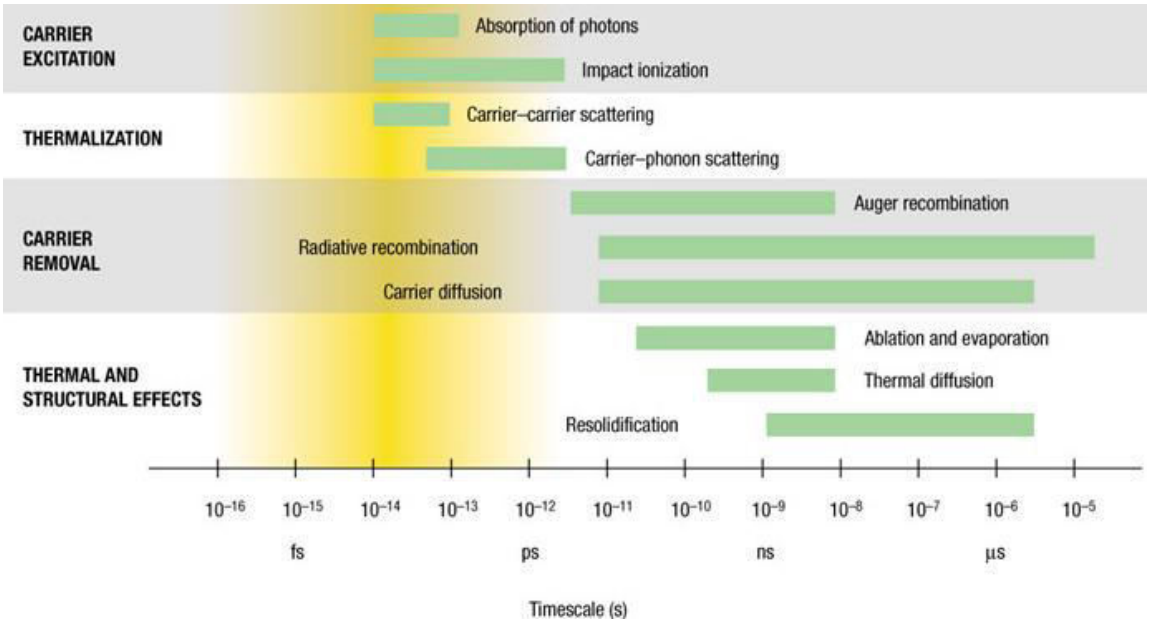

Figure 1.18: Processes (and associated timescales) taking place in the target following the absorption of the laser pulse [S. Sundaram and E. Mazur, 2002]

(1) Carrier excitation: Carrier (electrons in metals or electron-holes in semiconductors) excitation is the movement of an electron to a higher energy state due to absorption of photons by a laser beam. Single or multiphoton absorption are the dominant mechanisms for exciting electrons in the valence band provided that the energy gap is smaller or greater respectively than the photon energy. If some of the carriers are exited well above the band gap (or Fermi level in metals), impact ionization can generate additional excited states.

2) Thermalization: After excitation, electrons and holes are redistributed throughout the conduction and valence bands by carrier–carrier and carrier–phonon scattering.

(3) Carrier removal: Once the carriers and the lattice are in equilibrium, the material is at a well-defined temperature. Although the carrier distribution has the same temperature as the lattice, there is an excess of free carriers compared to that in the thermal equilibrium. The excess carriers are removed either by recombination of electrons and holes or by diffusion out of the excitation region.

(4) Thermal and structural effects. On the time scale of 10^{-11} sec and below carriers and lattice come to an equilibrium temperature and heat is diffused from the material‘s surface to the bulk. If the laser pulse intensity exceeds the melting or boiling point thresholds, melting or vaporization of the material occurs. As the deposited optical energy is converted to kinetic energy of the lattice ions,

material removal via ablation can occur in the form of individual atoms, ions, molecules or clusters. Finally solidification of the material occurs in timescales from nanosecond through microseconds.

There is a distinct line at about 10^{-12} - 10^{-11} s which distinguishes the regimes between non-thermal and thermal processes [D. von der Linde *et al*., 1997]. Mechanisms leading to structural modifications using picosecond and longer laser pulses are predominantly thermal. By contrast, exposure to ultrashort (femtosecond) pulses leads to a different type of modification. As illustrated in Figure 1.18, for pulse durations that are significantly less than electron-to-lattice (ions) non-thermal pathways may be accessed that take place on a timescale shorter than a picosecond, hence before thermal processes are initiated. Nevertheless, there are still several aspects of femtosecond laser induced modification of solids yet to be interpreted.

1.7.3 Ultra-short pulsed laser processing for material structuring

A variety of micrometer-scale structures have been observed on substrates of different materials after pulsed laser irradiation. The resulting structures/ morphology depend on the material (optical and thermal properties), laser source (such as laser fluence, repetition rate, wavelength, etc.) and irradiation environment (liquid, vacuum or reactive gas). In this respect, upon irradiation with laser pulses at a fluence close to the melting threshold, the surfaces of the substrates develop ripples with a spacing equal to or larger than the laser wavelength [J. Young *et al*., 1984]. By irradiating silicon surfaces with femtosecond laser pulses above the ablation threshold in the presence of a variety of background gases, quasi-periodic sharp conical micrometer-sized spikes. High-intensity nanosecond pulses can induce the formation of much larger conical microstructures [A. Pedraza *et al*., 1999; S. Dolgaev *et al.*, 2001]. By irradiating silicon surfaces with 400 nm femtosecond laser pulses in water, the formation of submicrometer-sized silicon spikes with diameters down to 200 nm is reported [M. Shen *et al.*, 2004].

Microstructuring by ultra-short pulsed lasers is an especially attractive approach, because it leads to the formation of arrays of high-aspect ratio microcones (MCs) on solid surfaces. In particular, femtosecond lasers allow patterning through non-linear absorption processes, providing excellent control over the regularity and uniformity of 3D micron and submicron features [E. Stratakis, 2012]. This method exploits a number of phenomena taking place under the action of intense pulsed laser irradiation of crystalline Si in the presence of a reactive gas, in order to induce morphological, structural and compositional modifications on its surface. The resulting structures, apart from their unique (conical) morphology, also exhibit improved optical, electronic and wetting response. Proper

tuning of the laser (such as laser fluence, repetition rate, etc.) and reactive gas parameters (such as pressure) can lead to the formation of structures with different morphologies [V. Zorba *et al*., 2006]

One of the most useful properties of ultrafast laser induced modification is the limited size of the affected volume. Ablation with laser pulses is induced by optical breakdown, which generates plasma near the laser focus. Because the plasma recombines before thermal effects set in (thermal diffusion, shock wave propagation, and cavitation) as was explained in 1.7.2, ablation of the substrate is confined, at least initially, to a small volume. Although the intensity required to initiate breakdown is fairly high, the short duration of the pulse allows the threshold intensity to be achieved with a lower intensity. The combination of localized excitation and low threshold fluence can greatly reduce the extent of collateral damage to surrounding areas, so that the size of the affected material can be microscopic—very close to the diffraction-limited focusing volume. As a consequence, three-dimensional structures constructed using nonlinear absorption laser structuring techniques provide excellent control over micro- and submicron scales.

Additional advantages of laser structuring include the high fabrication rate, noncontact interaction, applicability to many types of materials, such as ceramics, metals, and polymers, and reproducibility. It can be used to shape materials both laterally as well as into the depth of the material, hence allowing the manufacture of structures with complex geometries, including 3D shapes or structures with varying wall shapes and etch depths, and various aspect ratios on the same substrate, which represents a great difficulty for planar clean-room techniques. Furthermore, lasers can be easily incorporated to computer-assisted fabrication systems for complex and customized 3D matrix structure design and manufacture [E. Stratakis, 2012].

2. Problem statement and aim of the present PhD thesis

2.1 Problem statement

The final identity and behavior of a cell is shaped by the molecular and mechanical composition of its surroundings, which include the contact area with the other cells and the extra-cellular space or matrix (ECM), formed by biomolecules configured in different geometrical arrangements. Molecular cues have tight established roles in promoting cellular functions, i.e. proliferation, differentiation, etc. However, there is growing evidence that topographical and rigidity cues in the extracellular environment act synergistically with these molecular cues. Like chemical cues, physical cues do not elicit a stable response, but rather a response that depends on the sensory makeup of the cell.

The first attempt to investigate the effect of topographical cues on cellular functions stems already since 1911 with the sophisticated Harisson's experiments. Cells growing on a spider web followed the fibers of the web and therefore Harisson reported for the first time the ability of the substratum to influence cell orientation, migration and cytoskeletal organization. The phenomenon was described as stereotropism or physical guidance. Later on, in 1934, P. Weiss in an attempt to describe the tendency of the cells to orient themselves along anisotropic (topographical) features of the surface (such as fibers/ridges), established the term ''contact guidance'' [S. Moore and M. Sheetz, 2011].

With the emergence of micro- and nanofabrication techniques, a plethora of approaches for engineering or tailoring surfaces in a controllable manner are now available. Using techniques such as photolithography, microcontact printing, microfluidic patterning, electrospinning and self-assembly, 3D topographical features of tailored geometry, roughness and orientation, complemented by the desired spatial resolution at micron and submicron scales, can be realized on material surfaces [J. Voldman *et al*., 1999; T. Park and M. Shuler, 2003; H. Andersson and A. van den Berg, 2004]. Patterning of culture surfaces has triggered the development of new types of cell culture substrates, where the effect of topographical cues on cellular responses can be carefully and specifically investigated and/or controlled, depending on the field of interest. Numerous studies with such culture substrates have shown that many cell types (i.e. macrophages, fibroblasts, osteoblasts, etc.) react strongly to microtopography.

Changes in cell functions, like cell adhesion, alignment, morphology (cytoskeletal organization), proliferation, gene expression and differentiation have been reported [E. Martinez *et al.*, 2009].

Unlike other tissue types, which consist of cells with a much more homogeneous structure and function, the nervous tissue spans in a complex multilayer environment whose topographical features display a large spectrum of morphologies and size scales. Cell bodies vary greatly in size and shape between the different cell types [E. Kandel *et al.*, 2000]. The great diversity of morphologies is interrelated with a wide functional multiplicity. In the nervous tissue, a change in cell morphology induced by specific geometric patterns of its surroundings is correlated with emergent functions at the cellular or tissue level and is very important during early nervous system development as well as peripheral nerve regeneration.

Because of the necessity of a multilayer environment, the well established flat tissue culture surfaces are proven to be insufficient for studying the effect of the topography of the surroundings on nerve cell morphology and function. In an attempt to approach the complexity of the topographical milieu of nerve cells, it is necessary to shift to more complex 3D micropatterned surfaces.

Different approaches (regarding the material, fabrication technique, cell type and assay) have been used in order to fabricate surface micropatterned substrates, where the effect of topography on nerve cell responses could be studied. By restricting the physical area on which neurons can attach and grow and therefore, controlling growth pattern, surface micropatterned substrates can be used to promote selective development and migration of different cells or cellular compartments [T. Pearce and J. Williams, 2007]. An example of surface patterning for studying neurons includes the use of electrode sites, to control positioning of the cell bodies on a multielectrode array in order to enhance signal detection. Another example is the separation of nerve cell compartments (i.e. cell body from axon, etc.) in the case of microfluidic/cell culture platforms for the *in vitro* study of separate nerve cell compartments and their biochemical features. In the clinical field of neurobiological research, implantable scaffolds with cell-guiding topographical elements promoting *in vivo* tissue regeneration have been fabricated.

The approach used in the present study involves the fabrication of microconical structured silicon surfaces by ultra-short pulsed laser processing. These microconical silicon substrates have been used as cell culture platforms in previous work of the group. It was shown that controlling surface roughness and wettablity of the micropatterned Si substrates, fibroblast cell adhesion could be tuned [A. Ranella *et al.*, 2010]. In another study, it was shown that cortical neurons could form an elaborate web of cytoplasmic processes in the absence of neuroglial elements [E. Papadopoulou *et al*., 2010]. To this respect, the question of the present study was focused on how the cells of the peripheral nervous system (both neurons and neuroglia) can be grown and respond to the underlying surface topography.

2.2 Aim

The aim of the present study was to investigate the cellular growth on laser micropatterned Si substrates (comprising arrays of microcones -MCs) fabricated by ultra-short pulsed laser processing. Using increasing laser fluence, three types of micropatterned Si surfaces, which exhibit different geometrical characteristics (denoted as low, medium and high roughness substrates, respectively), have been fabricated and characterized as to surface morphology, wetting properties and surface chemistry. These three micropatterned Si substrates together with the unpatterned flat Si have been applied to *in vitro* cell cultures. The cell models used included PC12 cells, dissociated primary cells of the PNS, dorsal root ganglion (DRG) explants and cocultures of dissociated sympathetic neurons and Schwann cells. PC12 cells were used in order to study the growth and differentiation pattern after treatment with NGF (neuritogenesis) on the micropatterned Si substrates. Dissociated primary cells of the PNS were used in order to investigate the topographic guidance of neural outgrowth and network formation of dissociated superior cervical ganglion (SCG) sympathetic neurons and the effect of (surface) topography on Schwann cell morphology. Finally, the organotypic dorsal root ganglion (DRG) explant model was used in order to study the topography-dependent neurite outgrowth and Schwann cell migration from DRG explant.

2.3 Flow Sheet

Figure 2.1 illustrates the flow sheet of the experimental design of the present PhD thesis.

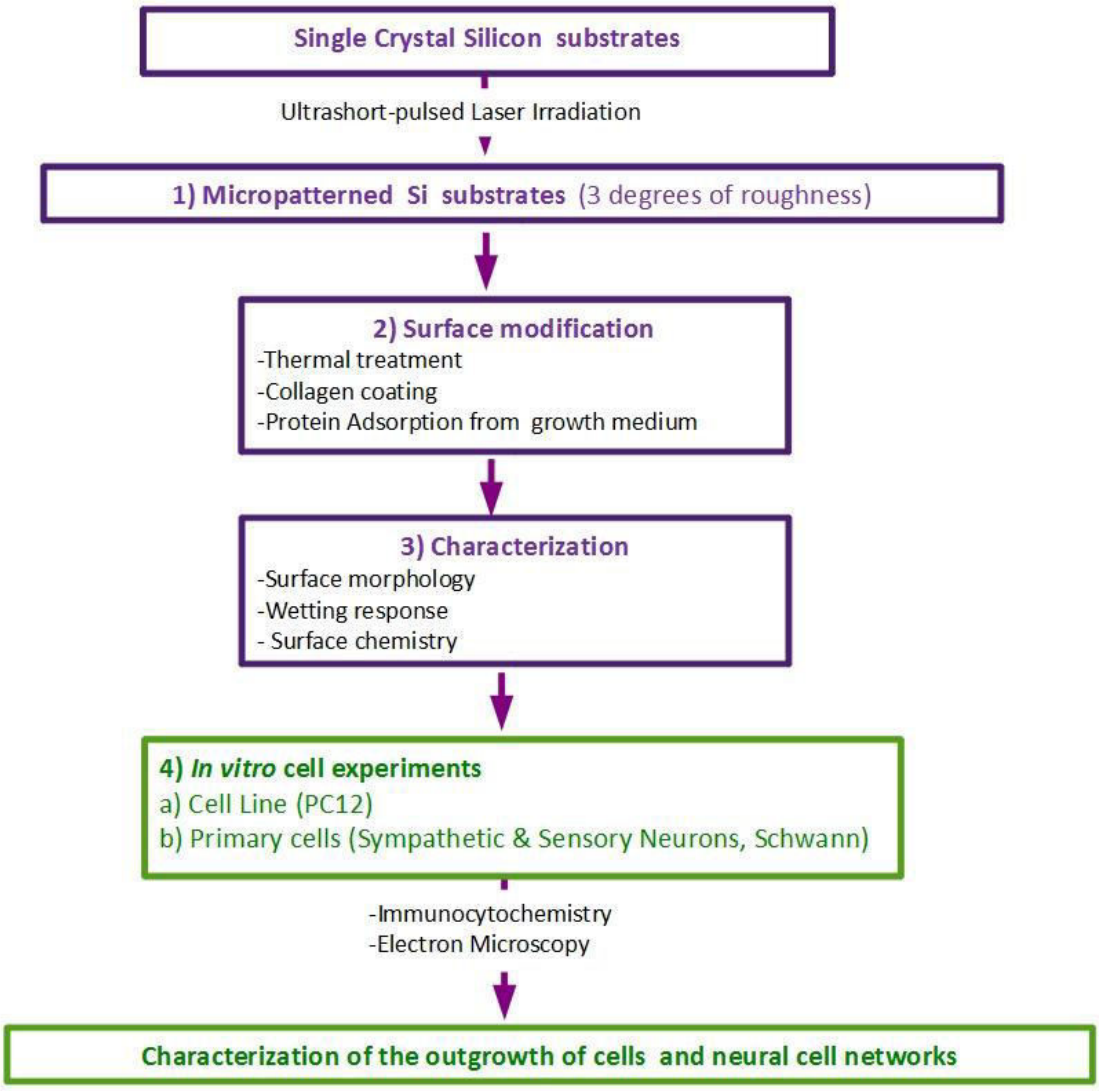

Fig. 2.1: Flow sheet of the experimental design of the PhD thesis

3. Experimental Part: Materials & Methods

3.1 Micropatterned Si substrates

3.1.1 Fabrication of micropatterned Si substrates by ultra-short pulsed laser processing

Single crystal n-type Silicon (1 0 0) wafers were subjected to laser irradiation in a vacuum chamber evacuated down to a residual pressure of 10^{-2} mbar. A constant sulfur hexafluoride (SF_6) pressure of 500 Torr was maintained during the process through a precision microvalve system. The irradiating laser source was constituted by a regenerative amplified Ti:Sapphire (λ = 800 nm), delivering 150 fs pulses at a repetition rate of 1 kHz. The sample was mounted on a high-precision X–Y translation stage normal to the incident laser beam. The laser fluence used in these experiments was in the range 0.68–1.50 J/cm^2. In some cases micropatterned Si surface/substrate (5 ×5 mm^2) contained three bands, each fabricated at a different laser fluence value.

3.1.2 Characterization of micropatterned Si substrates

The solid surface, or more exactly the solid-gas or solid-liquid interface, has a complex structure and complex properties dependent upon the nature of solids, the method of surface preparation, the interaction between surface and the environment. Properties of solid surfaces are crucial to surface interaction. Characterization of a material's surface properties is needed, in order to relate important surface characteristics to biological responses. Chemical, topographic, mechanical and electrical properties may all influence the way proteins and cells interact with a material. Surface analytical techniques include the Contact Angle Analysis, X-Ray Photoelectron Spectroscopy, Fourier Transform Infrared, Secondary Ion Mass Spectroscopy, Scanning Electron Microscopy and Atomic Force Microscopy, etc. and provide information about the outermost one to ten atomic layers of a material. Unfortunately, there is no technique capable of providing all needed information. The different surface characterization techniques provide complementary information regarding the surface characteristics [B. Bhushan, 1990; K. Dee *et al*., 2002].

The micropatterned Si substrates were investigated regarding their morphological, chemical and wetting characteristics, using the following characterization techniques.

3.1.2.1 Scanning electron microscopy (SEM)

3.1.2.1.1 Technique

Scanning electron microscope (SEM) is a type of microscope that uses an electron beam to

illuminate the specimen and produce a magnified image. The beam of electrons is produced at the top of the microscope (electron gun), follows a vertical path through the column of the microscope, makes its way through electromagnetic lenses which focus and directs the beam down towards the sample. The beam passes through pairs of scanning coils or pairs of deflector plates in the electron column, typically in the final lens, which deflect the beam in the x and y axes so that it scans over a rectangular area of the sample surface. The focused beam of high-energy electrons generates a variety of signals at the surface of solid specimens. The signals that derive from electron-sample interactions reveal information about the sample, including external morphology or surface topography, chemical composition and other properties, such as electrical conductivity. The spatial resolution of SEM depends on the size of the electron spot, which in turn depends on both the wavelength of the electrons and the electron-optical system which produces the scanning beam. Depending on the instrument, the resolution ranges between 1 and 20 nm. [N. Cortadellas *et al*., 2012]

3.1.2.1.2 Experimental process

Micro-structured surfaces were morphologically characterized by scanning electron microscopy (SEM). SEM was performed on a JEOL 7000 field emission scanning electron microscope with an acceleration voltage of 15 kV.

3.1.2.2 Wetting properties via contact angle measurement

3.1.2.2.1 Technique

Contact angle analysis involves measuring the angle of contact (θ) between a liquid and a surface. The phenomenon of contact angle can be explained as a balance between the cohesive force among the liquid molecules and the adhesive force between the surface and the liquid molecules. When a drop of liquid is placed on a surface, it will spread to reach a force equilibrium, in which the sum of the interfacial tensions in the plane of the surface is zero: $\cos\theta = (\gamma_{sv} - \gamma_{sL}) / \gamma_{LV}$

where γ_{sv} represents the solid-vapor surface tension, γ_{sl} represents the liquid-solid surface tension, and γ_{lv} represents the liquid-vapor surface tension. The energetics at each of the interfaces causes the droplet (usually water in testing of biomedical materials) to assume a particular shape (different degree of spreading). Calculations based on measured contact angle values yield an important parameter—the solid surface tension, which quantifies the wetting characteristics of a solid material. Depending on the contact angle value, a surface can be characterized as hydrophilic ($<90^o$) or hydrophobic ($>90^o$) (Fig. 3.1). There are a number of ways to measure the contact angle including sessile drop, captive air bubble

method, capillary rise method. Contact angle analysis provides a first screening of material surface and gives an insight into how the surface will interact with the external world. It indirectly measures surface energy, roughness, contamination, etc. and directly surface wettability. Wettability (or wetting response of a surface) is very critical in the early stages of many interfacial phenomena, such as cell - biomaterials interactions, because it can determine protein adsorption which precedes and influences cell adhesion, or biofilm immobilization (on surfaces). In this context, quantitative contact angle has been used to predict the performance of (vascular) grafts or implants, and the adhesion of cells to surfaces [K. Dee *et al*., 2002; B. Ratner *et al.,* 2004; J. Temenoff and Mikos, 2008].

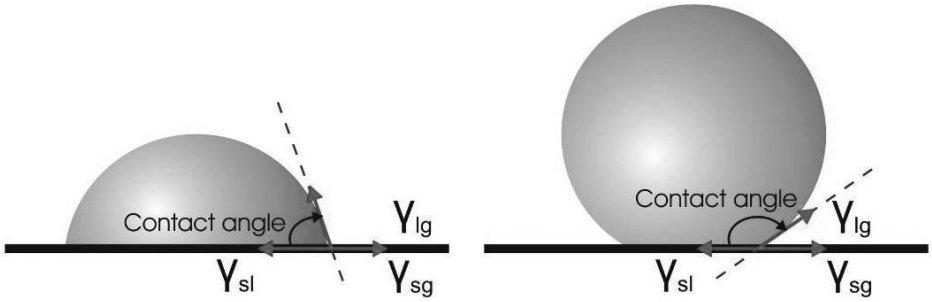

Figure 3.1: A sessile liquid drop on (a) a hydrophilic and (b) a hydrophobic surface [V. Zorba, 2007]

3.1.2.2.2 Experimental process

Static contact angle measurements were performed using an automated tension meter, using the sessile drop method. A 2-3 µl distilled, deionized Millipore water droplet was gently positioned on the surface, using a microsyringe, and images were captured to measure the angle formed at the liquid–solid interface. The surfaces being measured had a surface area of at least 5x5 mm^2. All experiments were carried out under normal atmospheric conditions and at an ambient temperature of 20^oC. The mean value was calculated from at least five individual measurements. Successive measurements were reproducible within ± 1^o.

3.1.2.3 X-ray Photoelectron Spectroscopy

3.1.2.3.1 Technique

X-ray Photoelectron Spectroscopy (XPS), also known as Electron Spectroscopy for Chemical Analysis (ESCA), is a widely used technique to investigate the chemical composition of surfaces. In X-ray photoelectron spectroscopy, irradiation of a sample material with monoenergetic soft x-rays causes

electrons to be ejected, according to the photoelectric effect. In this type of spectroscopy, X-ray absorption causes the removal of an electron from one of the innermost atomic orbital (not the valence shell). Electrons ejected from the surface are energy filtered via a hemispherical analyzer (HSA) before the intensity for a defined energy is recorded by a detector. Because the energy of an X-ray with particular wavelength is known, and because the emitted/ejected electrons' kinetic energies are measured, the electron binding energy of each of the emitted electrons can be determined, according to the following equation:

$$E_{\mathbf{binding}} = E_{\mathbf{photon}} - (E_{\mathbf{kinetic}} + \phi)$$

where $E_{binding}$ is the binding energy (BE) of the electron, E_{photon} is the energy of the X-ray photons being used, $E_{kinetic}$ is the kinetic energy of the electron as measured by the instrument and φ is the work function of the spectrometer [B. Ratner *et al*., 2004 ; J. Temenoff and A. Mikos, 2008].

Since core level electrons in solid-state atoms are quantized, the resulting energy spectra exhibit resonance peaks characteristic of the electronic structure for atoms at the sample surface. In this way, identification of the elements in the sample can be made directly. The relative concentrations of elements can be determined from the photoelectron intensities. An important advantage of XPS is the ability to provide information on chemical states from the variations in binding energies, or chemical shifts of the photoelectron lines, providing an insight into the chemical environment of the atoms at the surface [CasaXPS, 2011].

XPS technique offers several key features, making it ideal for structural and morphological characterization of ultra-thin oxide films. The relatively low kinetic energy of photoelectrons (< 1.5 keV) makes XPS inherently surface sensitive in the range (1-10 nm). Secondly, the energy of the photoelectron is not only characteristic of the atom from which it was ejected, but also in many cases is characteristic of the oxidation state of the atom.

3.1.2.3.2 Experimental process

The XPS-measurements of the substrates have been performed at the Institute of Chemical Engineering Sciences (ICE-HT) of FORTH.

Spectral analysis with X-ray Spectroscopy was carried out with the LHS-10 system of SPECS company, using monochromatic AlKα as an excitation source (h ν = 1486.6eV). XPS measurements have been performed at room temperature in ultra high vacuum conditions (10^{-9} mbar). A hemispherical electron analyzer was operated in fixed analyzer transmission (FAT) mode by selecting a constant pass energy of 36 eV throughout the measurements. Under these conditions, the full-width at half-maximum

(FWHM) of theAg3d line was confirmed to be 0.9 eV. The analysis area was a rectangle with a surface area of 2.5x4.5mm^2.

3.1.3 Qualitative and quantitative characterization of the micropatterned substrates' topography via image processing analysis

An image processing algorithm (ImageJ, National Institutes of Health, Bethesda, MD, USA) was implemented in order to determine the topological characteristics of the micro-patterned substrates - including roughness features, density (D), aspect ratio (A), height (h), and base diameter (d) - from top, side-view and cross-sectional SEM images. The aspect ratio was calculated by dividing the height by the radius of the cone's base. The roughness ratio, r, was calculated by dividing the actual, unfolded, surface area of spikes by the total irradiated area. The mean value was calculated from statistics performed at 10 individual surfaces in each case. The data were subjected to one-way ANOVA, followed by Tukey test for multiple comparisons between pairs of means.

In order to quantify the extent of orientation of the silicon cones/spikes morphology, SEM images were analyzed. Top view electron microscopic images of the micropatterned Si substrates were taken digitally and opened using ImageJ. The images have been inverted, thresholded (using the same threshold value for all images) and the major axis for each spike with their respective endpoints (a and b) (for each major axis) have been graphically selected. The x and y coordinates for each endpoint have been calculated and in turn the angle of the line (ab), were defined as:

angle : = ATAN(change in Y)/(change in X).

This was repeated for all the spikes in each image. These were all stored in an Excel spreadsheet. With the aid of the frequency function, for this resulting set of angle values and a given set of bins (0-10^o, 10-30^o, 30-60^o and 60-90^o), the number of values that occurred in each interval were counted. At least 60 spikes for each roughness type have been used for the analysis.

3.1.4 Surface modification of the laser micropatterned silicon substrates by different experimental approaches

N-type Silicon (100) substrates have been laser irradiated at low, mid and high laser fluence, according to the Paragraph 3.1. The substrates have been immersed in 10% HF solution for 30min, rinsed with nanopure water and dried with nitrogen flow. In order to study the effect of surface topography modifications to cell growth, three different treatments have been performed. The substrates were further used for characterization. For each case, untreated micropatterned Si substrates have been used as a control.

3.1.4.1 Thermal treatment

Flat and micropatterned Si substrates of all types of roughness were subjected to a different sequence of treatment steps:

i) Thermal treatment at 1000 ^{o}C for 30 min in air environment within a box furnace,

ii) Thermal treatment within an autoclave (high pressure saturated water vapor at 121 °C for around 15–20 minutes) and

iii) The i) treatment followed by the ii).

The latter two conditions represent the standard conditions for the sterilization of substrates used in the present study for the cellular assays. The substrates were further processed to characterization. For each case, untreated micropatterned Si substrates have been used as a control.

3.1.4.2 Collagen coating

Micropatterned Si substrates of all types of roughness were subjected to a different sequence of treatment steps:

1) a. Thermal treatment in an autoclave (see Paragraph 3.1.4.1) / b. immersion in 2% collagen solution (in 70% ethanol aqueous solution) / c. drying under Nitrogen (N_2) flow
2) a. Thermal treatment in an autoclave (see Paragraph 3.1.4.1) / b. immersion in 2% collagen solution / c. rinse with phosphate buffered saline (PBS) / d. drying under N_2 flow
3) a. Thermal treatment in a tube furnace (see Paragraph 3.1.4.1) / b. thermal treatment in an autoclave / c. immersion in 2% collagen solution / d. drying under N_2 flow
4) a. UV for 2hrs / b. immersion in 2% collagen solution / c. drying under N_2 flow

These conditions represent the treatment steps for the in vitro assays with cells, where protein coating of the surfaces was necessary (according to literature). The substrates were further processed to characterization. For each case, untreated micropatterned Si substrates have been used as a control.

3.1.4.3 Protein Adsorption from growth medium

Flat and micropatterned Si substrates of all types of roughness were subjected to a different sequence of treatment steps:

1) a. Thermal treatment in an autoclave (see Paragraph 3.1.4.1) / b. immersion in 10% fetal bovine serum (in DMEM growth medium solution) / c. drying under Nitrogen (N_2) flow

2) a. Thermal treatment in an autoclave (see Paragraph 3.1.4.1) / b. immersion in 10% fetal bovine serum (in DMEM growth medium solution) / c. rinse with phosphate buffered saline (PBS) / d. drying under N_2 flow.

The substrates were further processed to characterization. For each case, untreated micropatterned Si substrates have been used as a control.

3.2 Animals used

Sprague dawley rats and C57/BL6 mice were used for the experiments. Animals were housed in a temperature-controlled facility on a 12h light/dark cycle, fed by standard chow diet and water ad libitum in the Animal House of the Institute of Molecular Biology and Biotechnology (IMBB-FORTH, Heraklion, Greece).

3.3 Biochemical Materials

3.3.1 Growth media & supplements

For the cell culture, the following growth media have been used: Dulbecco's modified Eagle's medium (DMEM; Invitrogen, Grand Island, NY, USA); Dulbecco's modified Eagle medium (DMEM)–F12, (GIBCO/Life Technologies 22320-022); Roswell Park Memorial Institute (RPMI 1640, GIBCO/Life Technologies 32404-014); Hank's Balanced Salt Solution (HBSS). The culture media were supplemented with horse serum (HS; Invitrogen, Carlsbad, CA, USA) and/or fetal bovine serum (FBS; Biosera, Sussex, UK). The following antibiotics have been used: penicillin / streptomycin (GIBCO/ Life Technologies 15140-122).

3.3.2 Growth factor

Nerve growth factor (NGF; 2.5 S, Millipore, Billerica, MA, USA) has been used for nerve cell differentiation at the concentration of 50 & 100 ng /ml.

3.3.3 Antibodies

PC12 cells were immunostained using the following antibodies: anti-neuron-specific βIII

isoform of tubulin monoclonal antibody (MAB1637; 1:900 in PBS–BSA 2%; Millipore, Billerica, MA, USA) detected by an FITC conjugated secondary antibody (1:200 PBS–BSA 2%;Biotium, USA). Tetramethyl rhodamine isothiocyanateconjugated phalloidin (1:400 in PBS–BSA 2%; Biotium) has been used to stain F-actin.

Primary nerve cells were immunostained using the following antibodies: Schwann cells were stained with anti-S100b (1:500 Abcam, Rab Mab ab52642), neurons were stained with anti-NF200kD (1:10000 Abcam, Chicken polyclonal ab4680) and fibronectin with an anti-rat fibronectin antibody (1:100 rabbit polyclonal Ab2047 Millipore, Billerica, MA, USA). Alexa Fluor 546 goat anti-rabbit IgG (MoBiTec A-11010) or Alexa Fluor TM 488 goat anti-mouse IgG (MoBiTec A-11001) were used as secondary antibodies.

Cell nuclei were stained using 4 0 ,6-diamidino-2phenylindole dihydrochloride (DAPI; 1:1000) or TOPRO.

3.3.4 Chemicals

5-fluorodeoxyuridine (FdU) with uridine (Sigma – Aldrich Chemie GmbH, Munich, Germany) have been used as anti-mitotic agents Cells were detached from the substrate and dissociated into single cell suspensions with trypsin 0,25% (Gibco//Life Technologies, Cat. No.15090) and/or 1% collagenase Type 1 (C0130, Sigma-Aldrich Chemie GmbH, Munich, Germany). Type I collagen (A1048301 Sigma-Aldrich Chemie GmbH, Munich, Germany) has been used for coating the substrates. Paraformaldehyde (PFA; SigmaAldrich Chemie GmbH) and Triton X-100 (Merck KgaA, Darmstadt, Germany) have been used as fixative and permeabilizing agents, respectively. Antifade reagent containing DAPI for the staining of nuclei (ProLong®Gold reagent; Molecular Probes, Eugene, OR, USA) was also used.

3.4 *In vitro* experiments with cells- PC12 cell line

3.4.1 Cell Culture

The rat pheochromocytoma PC12 cell line (ATCC-LGC, Rockville, MD, USA) was maintained in DMEM supplemented with 10% HS and 5% FBS (complete medium) at 37°C in a 5% CO_2 atmosphere. In order to minimize interassay variability, low passage number (P2–10) cells were used throughout the study. The collagen-coated MC-structured Si surfaces were placed in 48-well plates and covered with PC12 cells at a density of 0.75×10^5cells/ml. The cells were allowed to adhere in complete culture medium and 24 h later this was either replaced by fresh complete medium or with

differentiation medium (DMEM supplemented with 50 ng/ml NGF; 2.5 S, Millipore, Billerica, MA, USA). Complete or differentiation medium was replaced every 2 days. PC12 cells were also grown on collagen-coated flat silicon wafers (negative control condition). Standard polystyrene (PS) tissue culture coverslips (positive control; Sarstedt) were used in order to monitor the progress of the cell culture, since Si substrates are not optically transparent and therefore cannot be viewed via a light microscope. A minimum of three replicates were used for each experiment.

3.4.2 Characterization

The cells cultured on the micropatterned Si substrates have been subjected to immunocytochemical assays for the study of cell outgrowth and differentiation. Quantitative information (regarding cell number, differentiation, neurite length, etc.) was assessed using an image-processing algorithm (ImageJ) based on fluorescence microscopy images. The morphology of PC12 cells was analyzed by scanning electron microscopy.

3.5 In vitro experiments with cells- Primary cells

In vitro experiments with primary cells have been performed in collaboration with Paschalis Efstathopoulos and Alexandra Kourgiantaki in the laboratory of Pharmacology, which is directed by Prof. A. Gravanis at the Department of Basic Sciences (Faculty of Medical School, University of Crete).

3.5.1 Cell culture

All cells were cells were seeded onto silicon scaffolds in 48 well-plate culture dishes and were cultured at 37 ^{o}C in a 5% CO2 atmosphere.

3.5.1.1 Schwann cells

Schwann cell primary cultures were prepared from sciatic nerves of P2-P4 rat pups. Upon dissection, nerves were enzymatically triturated in a Trypsin 0,25% and 1% collagenase Type 1 (sigma C0130) in HBSS solution for 30min at 37^{o} C. The enzymes were deactivated by adding DMEM containing 10% FBS to the cells and the sciatic nerves were mechanically dissociated into single cell suspensions. 10 ^{5} cells were seeded onto silicon scaffolds and cultured for 4 – 6 days until fixation for further analysis, with medium replacement every 2 days. In some experiments, Poly-D-lysine (PDL)

coating has been used. Schwann cells had a purity of more than 90%, and in these primary cultures only S100-positive Schwann cells were evaluated.

3.5.1.2 Dissociated Superior Cervical Ganglia Neuronal Cultures

Superior cervical ganglia (SCG) were dissected from newborn (P0–P1) rat pups and dissociated in 0.25% trypsin for 30 min at 37°C. After their dissociation, SCG neurons were re-suspended in RPMI culture medium 1640 containing 10% FBS, 100 units/ml penicillin, 0.1 mg/ml streptomycin, 10mM antimitotic agent FdU with uridine, and 50 or 100 ng/ml NGF). 10^4 cells were plated on collagen coated 48-well plates or silicon scaffolds and cultured for 7 days until fixation for further analysis. Medium was changed every 2 days.

3.5.1.3 Co-culture of Dissociated DRGs and Schwann cells

To test the extent to which Schwann cells affect the growth of SCG neurites on the micro-structured Si substrates, SCGs were co-cultured with Schwann cells that were first- seeded on the substrates as outlined above. Specifically, Schwann cells were grown on the micro-patterned Si substrates for 4 days until confluent. Dissociated SCGs were then pipetted onto these substrates, pinned down and cultured for an additional 4 days in the presence of 100ng/ml NGF.

3.5.1.4 Dorsal root ganglia (DRG) preparation and explants

Mouse embryos (embryonic day (E) 13.5) were dissected from pregnant mothers. DRGs from the lumbar region (L1–L4) were collected in cold PBS, then seeded onto the micro-structured Si substrates (2 – 3 DRG per substrate) and incubated in growth medium DMEM–F12 supplemented with 10% FBS. Explants were incubated 3-5 days *in vitro* (DIV) until fixation for further analysis

3.5.2 Characterization

The cells grown on the micropatterned Si substrates have been subjected to immunocytochemical analysis for the study of cell outgrowth, migration and network formation. Quantitative information (regarding cell number, outgrowth orientation, neurite width, neural network

type etc.) was assessed using an image-processing algorithm (ImageJ) based on fluorescence microscopy images. The morphology of the migrating Schwann cells and the outgrown neurites from the DRG explants were analyzed by scanning electron microscopy.

3.6 Qualitative & quantitative evaluation of cell cultures

3.6.1 Immunocytochemistry

3.6.1.1 Technique

Immunocytochemistry (ICC), by definition, is the identification of a tissue constituent in situ by means of a specific antigen–antibody interaction, where the antibody has been tagged with a visible label. Antibodies are proteins produced by the vertebrate immune system as a defense mechanism against infection. They are unique among proteins because they are made in billions of different forms, each with a different binding site that recognizes a specific target molecule (or antigen). Labeled with fluorescent dyes, antibodies are invaluable for locating specific molecules in cells by fluorescence microscopy. The precise antigen specificity of antibodies in combination with the large spectral range of available fluorophores allows simultaneous imaging of different cellular, subcellular or molecular components. Therefore, cell staining is a powerful method to localize a particular molecule of interest [S.-Y. Mao *et al*., 1995; B. Alberts *et al*. 2002, J. Lichtman and J.-A. Conchello, 2005].

ICC pretreatment comprises fixation and permeabilization of cells for the antibody access. Then, the sample with the cell is incubated with proper antibody that recognizes a specific antigen. This primary antibody, the antibody that binds to the protein, can be conjugated directly with a fluorescent molecule or chromogenic enzyme. This procedure is known as direct ICC. Alternatively, in indirect ICC, the cell sample is post-incubated with a secondary antibody that recognizes the primary antibody conjugated with a fluorescent molecule or chromogenic enzyme allowing the scientist to visualize the expression of the protein. The stained material is finally visualized using a fluorescence microscope [M.Carter and J. Shieh, 2010].

3.6.1.2 Experimental process

The detailed steps of the immunohistochemical analysis are described separately for PC12 and primary cell as follows:

PC12 cells were double-stained for F-actin and ß-tubulin. After 4 and 7 days of culture, the cells were fixed with 4% PFA for 15 min and permeabilized with 0.1% Triton X-100 in PBS for 3–5

min. The non-specific binding sites were blocked with 2% BSA in PBS for 30 min. The neuron-specific ßIII isoform of tubulin was detected by incubating the cells with the MAB1637 monoclonal antibody (1:900 in PBS–BSA 2%; Millipore, MA, USA) for 1 h at RT and subsequent labelling with goat–anti-mouse FITC conjugate secondary antibody (1:200 PBS–BSA 2%; Biotium, USA) for 45 min at RT. Simultaneously, the cells were incubated with tetramethyl rhodamine isothiocyanateconjugated phalloidin (1:400 in PBS–BSA 2%; Biotium) for the F-actin staining. The samples were then washed with PBS and mounted on coverslips with antifade reagent containing DAPI for nuclei staining.

In the case of primary cells, after removal of the medium, cells were fixed with 4% paraformaldehyde in PBS 0.1M blocked for 1h RT in PBS 0.3% Triton X-100 and incubated overnight at 4^{o}C with primary antibodies blocking buffer. Schwann cells were stained with anti-S100b (1:500 Abcam, Rab Mab ab52642), while neurons were stained with anti-NF200kD (1:10000 Abcam, Chicken polyclonal ab4680). Additionally, fibronectin which is expressed by non neuronal cells (glial cells & fibroblasts) was detected using an anti-rat fibronectin antibody (1:100 rabbit polyclonal Ab2047 Millipore). After 3 washes with PBS, specimens were incubated for 1h at RT Alexa Fluor 546 goat anti-rabbit IgG (MoBiTec A-11010) or Alexa Fluor TM 488 goat anti-mouse IgG (MoBiTec A-11001) secondary antibodies, diluted 1:500 in PBST. The cells were washed and nuclei counterstained with 4 0,6-diamidino-2phenylindole dihydrochloride (DAPI; 1:1000) or TOPRO (1:5000). The substrates were mounted on coverslips with antifade reagent containing DAPI for nuclei staining.

Results were evaluated with a Zeiss Axiophot epifluorescence microscope coupled to an on-line digital camera (Axiovision software).

3.6.2. Scanning electron microscopy (SEM)

3.6.2.1 Technique

The basics on Scanning electron microscope (SEM) technique have been presented in Paragraph 3.1.2.1.1. Electron microscopy is increasingly being used in cell biology. In order for a biological specimen to be imaged with SEM, a special preparation of the specimen is required. Since the specimen is exposed to a very high vacuum in the electron microscope, there is no possibility of viewing it in the living, wet state. Therefore, the specimen to be examined has to be fixed, dried, and coated with a thin layer of heavy metal. The specimen is then scanned with a very narrow beam of electrons. The SEM technique provides great depth of focus; moreover, since the amount of electron scattering depends on the angle of the surface relative to the beam, the image has highlights and

shadows that give it a three-dimensional appearance [B. Alberts *et al*., 2002]. In this context, SEM provides a very important information regarding the 3D cell outgrowth on substrates with different topographies, which is proven to be very useful in the research fields of tissue engineering and biomaterial design [L. Smith *et al*; 2010].

3.6.2.2 Experimental process

The morphology of the cells (either PC12 or primary cells) growing on the patterned surfaces was analyzed by SEM. After culture termination, the cells were washed with 0.1M sodium cacodylate buffer (SCB) and then incubated in the same solution for 15 min. After repeating this step twice, the cells were fixed using 2% glutaraldehyde, 2% formaldehyde in 1% SCB fixative buffer for 1 h at 4°C. All surfaces were then washed twice (for 15 min each time) with 1% SCB at 4°C, dehydrated by immersion in serially graded ethanol solutions (50–100%) and incubated for 15 min in dry 100% ethanol. Prior to electron microscopy examination, the samples were sputter-coated with a 10 nm gold layer (Humme Technics Inc, Alexandria, Virginia USA). SEM analysis used a JEOL 7000 field emission scanning electron microscope at an acceleration voltage of 15 kV.

3.6.3 Quantitative evaluation via image processing

Quantitative information (regarding cell number, neurite length, etc.) was assessed using an image processing algorithm (ImageJ; National Institutes of Health, Bethesda, MD).

3.6.3.1. Cell numbers (survival/proliferation)

Numbers of cells (PC12 cells, Schwann cells and neurons) that have been grown on the micro-patterned silicon substrates were determined by counting cell nuclei stained with DAPI. Nuclei number was assessed with ImageJ v1.36, using the "Cell Counter" plugin. The results represent the means of at least three different experiments (n= ~30 fields of view for each roughness type and time of culture).

3.6.3.2. PC12 cell differentiation on the micro-patterned Si substrates

Quantitative information (regarding cell number, neurite length, etc.) was assessed using an image-processing algorithm (ImageJ). Cell numbers and neurite length were measured manually. The number of differentiated cells was determined by visual examination of the field. A differentiated cell was considered to display at least one neurite with a length equal to the cell body diameter. The differentiation ratio was defined as the percentage of differentiated cells after treatment in the presence

of NGF over the total number of cells in the field. Neurite growth was determined by manually tracing the contour length of the longest neurite per cell for all cells in a field that had an identifiable neurite. Neurite length was the distance from the edge of the cell soma to the neurite tip. The mean length of the longest neurite per cell in each band of the microstructured area (low, medium or high roughness) was calculated.

3.6.3.3. Schwann Cell outgrowth orientation on the micro-patterned Si substrates

To determine Schwann cell orientation on the different micro-patterned silicon substrates, the cell nucleus orientation was measured, according to respective literature [L. Margolis et al., 1975; A.Nedzved et al., 2005; D. Thompson and H. Buettner, 2006]. Elliptical-shaped cells were outlined by hand and the major and minor axis of each cell ellipse was manually traced. The angle of the cell nucleus was then determined using the major axis of the cell ellipse. The orientation angle of the nucleus was measured as the angle between the major axis of the ellipse and the vertical axis of the image plane (Oy). Its values ranged between 0^o, signifying a perfectly aligned cell nucleus, to 90^o for a vertical cell nucleus. Only the absolute values have been considered, therefore no discrimination between leftward or rightward divergence from the Oy axis was taken into account. This was repeated for all the nuclei in each image. The values from all fields of views were inserted in a spreadsheet. The orientation of the cell nuclei with respect to the x-axis was binned into 30◦ intervals ranging from 0^o to 90^o to generate an orientation frequency, f, for the i_{th} interval i=1,2,3 (using the Frequency Function). The orientation angle has been calculated from at least 500 cell nuclei for each roughness type.

3.6.3.4. Axonal outgrowth orientation on the micro-patterned Si substrates

Assuming each axon (stained with anti-NF) connecting two somatas (stained with DAPI) as a vector, the orientation angle of this vector has been calculated and used as an index of the axonal outgrowth orientation. The orientation angle of each axon was measured as the angle between the axonal vector and the vertical axis of the image plane. Its values ranged between 0^o, signifying a perfect alignement to 90^o for a vertical outgrowth. Only the absolute values have been considered, therefore no discrimination between leftward or rightward divergence from the Oy axis was taken into account. This was repeated for all the axons in each image. The values from all fields of views were inserted in a spreadsheet. The orientation of the axons with respect to the y-axis was binned into 30◦ intervals ranging from 0^o to 90^o to generate an orientation frequency, f, for the i th interval i=1,2,3

(using the Frequency Function). This procedure was repeated for n experiments (to get the standard error). The orientation angle has been calculated from at least 300 axons for each roughness type.

Axonal fasciculation was determined by measuring the axonal thickness of NF positive axons from fluorescence microscopy images of high magnification (x 63 objective). For each axon the average thickness of the values in at least two points has been calculated. The axonal thickness was binned into 2 μm intervals ranging from 0 to 14 μm to generate an orientation frequency, f, for the i th interval i=1,2..-6 (using the Frequency Function). The axonal fasciculation has been calculated from at least 80 axons for each roughness substrate type.

3.6.4 Statistical Analysis

For statistical analysis, the data were subjected to one way ANOVA followed by Tukey tests for multiple comparisons between pairs of means, using commercially available software (SPSS 21, IBM). Statistically significant difference between experimental results was indicated by $p < 0.05$. In all cases, the results are expressed as means ± standard error (SE).

4. Results

4.1 **Fabrication of and characterization of microconically structured Si surfaces**

Nervous tissue comprises a very complex three-dimensional tissue environment whose topographical features span through a large spectrum of morphologies and size scales. In order to study the effect of platform architecture on nerve cell growth and differentiation, ultra-short pulsed laser structuring was applied on crystalline silicon (Si) wafers. This technique offers the advantage of patterning Si surfaces with periodic arrays of topographical features of microscale size, while offering high accuracy and reproducibility [E. Stratakis, 2012]. By varying the laser energy per unit area (fluence), substrates exhibiting different roughness ratios were obtained. At low laser fluencies, the irradiated surfaces comprised submicron-sized ripples, while at increased laser energy, quasi-periodical arrays of conical microstructures (denoted as microcones -MCs- or spikes) were formed (Figure 4.1B).

In this study, three types of patterned surfaces exhibiting different MC morphologies were fabricated using three different laser fluence values. As shown in Figure 4.1, each culture substrate consisted of these three microstructured areas, irradiated using 0.68 J/cm^2 (low roughness), 0.95 J/cm^2 (medium /mid roughness) and 1.50 J/cm^2 (high roughness), interspaced by an unstructured area (Fig. 4.1 A). Thus, each scaffold contained all three types of patterned surfaces, allowing direct comparison of cell growth preferences. As calculated from scanning electron microscopy (SEM) images, MCs' density decreases with increasing laser fluence and its value ranges from to 10^6 to 10^7/cm^2 (MC density is 9.75±1.54 and 2.50±0.26 on low and high roughness substrates, respectively). While spike density was lower in the high roughness structures, the MCs height increased. More specifically, MCs height varied from 1.26 ± 0.28 μm in the low roughness structures to 8.63 ± 1.17 μm in the high roughness structures (Table 4.1). It is also interesting to note that, although medium to higher roughness MCs maintained practically the same aspect ratio, their interspike distance increased in a geometrically justifiable manner (Figure 4.1C, Table 4.1). Indeed, comparing two series of conical spikes with the same aspect ratio but different heights, it was apparent that when MCs height increased by a factor of two, the interspike distance doubled as well.

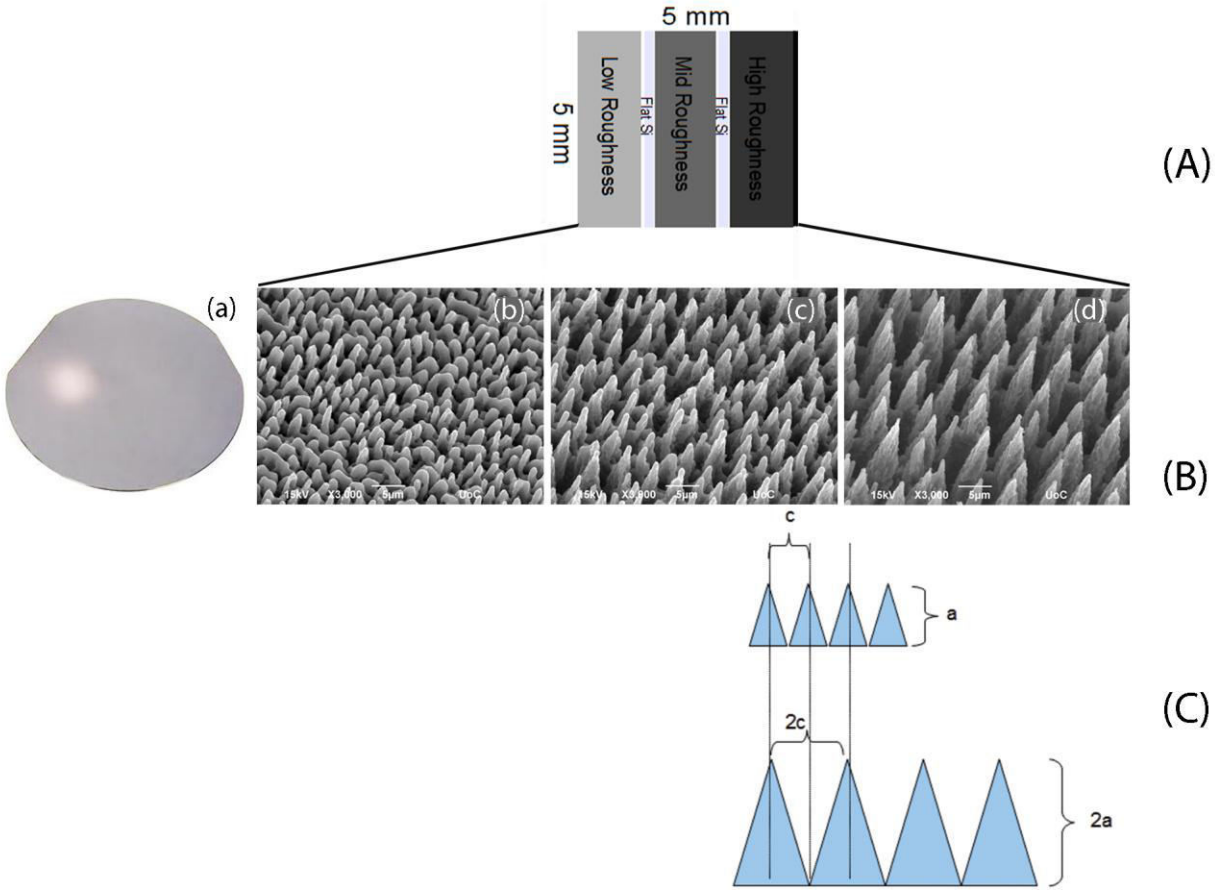

Fig.4.1: General characteristics of the laser patterned Si substrates: (A) schematic illustration of a laser patterned micro-structured Si substrate (5mm x 5mm) consisting of three bands of different roughness (low, mid, high). (B) Picture of a polished Si wafer (a); side SEM views of the as-prepared Si spikes surfaces structured at three different laser fluencies: 0.68 J/cm^2 (low roughness) (b), 0.95 J/ cm^2 (mid roughness) (c), and 1.50 J/ cm^2 (high roughness) (d). (C) Schematic illustration of a geometrical model for the underlying surface topography based on the lateral cut views of the laser patterned surfaces. Abbreviations in (C) are a: spike height, c: interspike distance.

Table 4.1: Geometrical characteristics of the different micropatterned Si substrates. *

Type of Roughness	**Density D+STDEV (*10^6/cm^2)**	**Height, a ± STDEV (µm)**	**Base diameter, b ± STDEV (µm)**	**Aspect Ratio, A ± STDEV**	**Interspike Distance, c ± STDEV (µm)**	**Roughness Ratio, r ± STDEV**
Low	9.75±1.54	1.26±0.28	1.87±0.60	1.41±0.27	1.73±0.28	1.74±0.23
Medium	5.01±0.19	3.76±0.42	2.17±0.25	3.51±0.52	2.06±0.53	3.65±0.49
High	2.50±0.26	8.63±1.17	4.78±1.03	3.73±0.80	4.48±0.96	3.83±0.76

* Geometrical characteristics of the different substrates used for this study, calculated out of the scanning electron microscopy (SEM) images with the aid of image processing software (ImageJ). The mean values were calculated from at least ten individual measurements. The data were subjected to ANOVA followed by Tukey test

for multiple comparisons between pairs of means. The difference in height between surfaces of low, medium and high roughness surfaces was highly significant ($p < 0.001$). The difference in base diameter and interspike distance between surfaces of low and high roughness surfaces was highly significant ($p < 0.001$). The difference in roughness ratio between surfaces of low and medium/high roughness surfaces was highly significant ($p < 0.001$).

Top SEM views revealed an elliptical base of the microcones which was more pronounced as the laser fluence/ surface roughness are increased. In order to quantify the (extent of the) orientation of the microcones, the orientation angle of the microcone with respect to the vertical axis of the image plane was measured from such SEM images. According to this analysis, low roughness Si substrates displayed a broad range of orientation angles (23, 26, 24 and 27% of the microcones had angles in the range of 0-10 ^{o}, 10-30^{o}, 30-60^{o} and 60-90^{o}, respectively). On the contrary, the majority of conical features in the medium and high roughness substrates were mostly parallel aligned (68% and 80 % of the microcones, respectively, were oriented at an angle of 0-10^{o}). Therefore, although at the lower laser fluences the spikes did not seem to possess a preferred orientation, the increase of laser fluence resulted in an orientation of parallel alignment of microcones. It can be postulated that the topography attained can be described as semiperiodical discontinuous (arrays of oriented microcones) comprising an anisotropic feature (elliptical base).

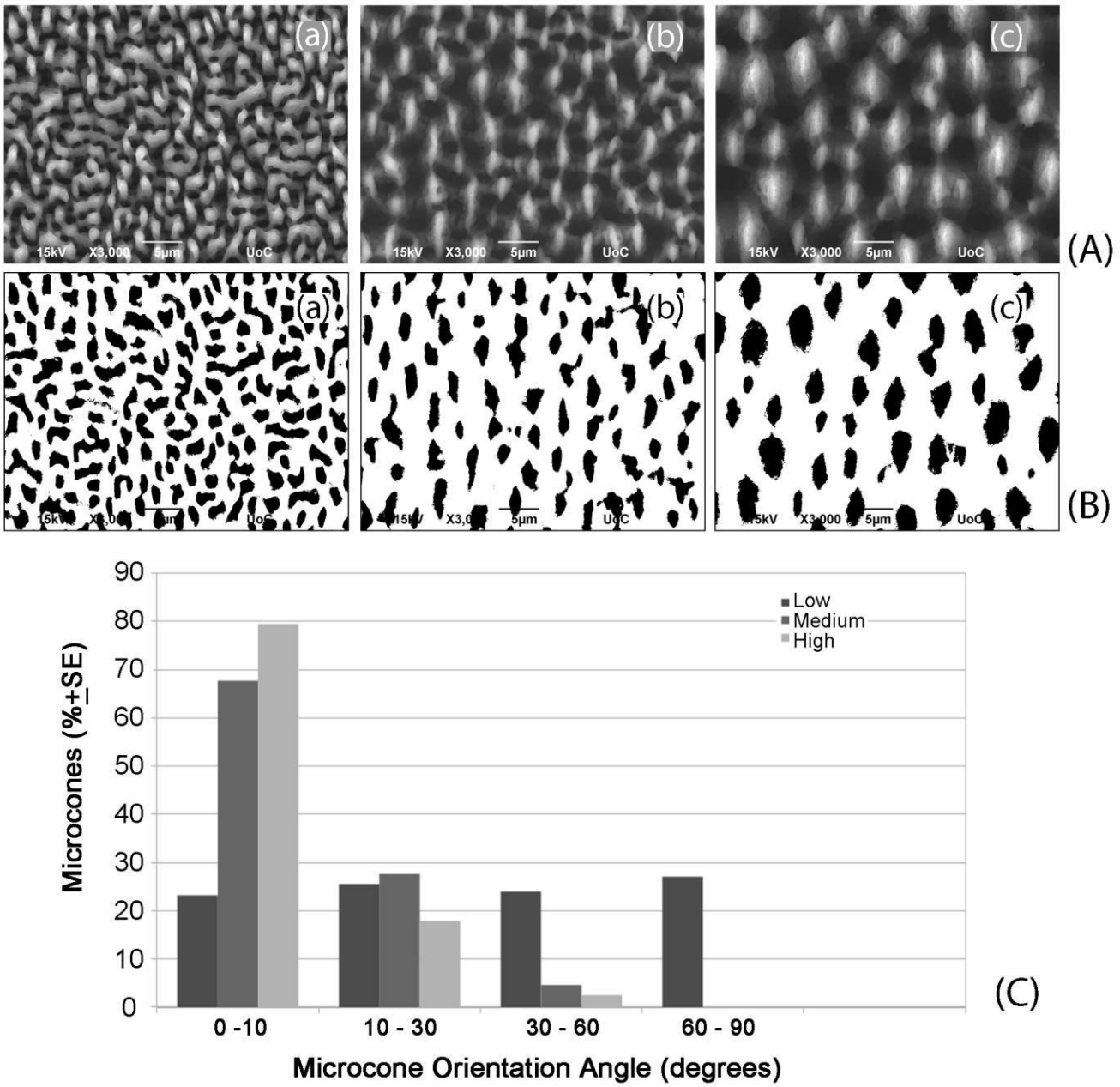

Figure 4.2: Quantitative evaluation of microcone orientation. (A) Scanning electron microscopy images (Top view) of micropatterned Si substrates of different roughness: low (a), medium (b) and high (c). (B) The same images after thresholding and binarizing. (C) Microcone orientation expressed in terms of the orientation angles' (frequency) distribution. The orientation angle of the microcone/spike was measured as the angle between the major axis of the ellipse and the vertical axis of the image plane. The number of features exhibiting an orientation angle value within a specific range is expressed as percentage of microcones $\pm$ standard error of the mean. At least 60 spikes for each roughness type have been used for the analysis.

Following this description, Table 4.1 should be corrected accordingly. Table 4.2 lists the geometrical characteristics of the different micropatterned Si substrates with according to this

geometrical model.

Table 4.2: Geometrical characteristics of the different substrates. *

Type of Roughness	Height, a ± STDEV (µm)	Base major axis, b + STDEV (µm)	Base minor axis, b' + STDEV (µm)	Aspect Ratio, A ± STDEV	Interspike Distance, c ± STDEV (µm)	Roughness Ratio, r ± STDEV
Low	1.26±0.28	1.96±0.35	1.11±0.20	1.91	2.59±0.72	1.74±0.23
Medium	3.76±0.42	3.57±0.43	1.98±0.34	3.14	4.71±0.37	3.65±0.49
High	8.63±1.17	7.25±0.72	3.78±0.77	3.76	6.50±0.84	3.83±0.76

* Geometrical characteristics of the different substrates used for this study, calculated out of scanning electron microscopy (SEM) images with the aid of image processing software (ImageJ). The mean values were calculated from at least ten individual measurements. The data were subjected to ANOVA followed by Tukey test for multiple comparisons between pairs of means. The difference in height between surfaces of low, medium and high roughness surfaces was highly significant ($p < 0.001$). The difference in base diameter and interspike distance between surfaces of low and high roughness surfaces was highly significant ($p < 0.001$). The difference in roughness ratio between surfaces of low and medium/high roughness surfaces was highly significant ($p < 0.001$).

The enhancement in microcone roughness was accompanied by a decrease in surface hydrophilicity (Fig. 4.3) [V. Zorba et al., 2006]. Fig.4.3 shows the static contact angles of 3 µl nanopure water drops in contact with flat Si (a), low (b), medium (c) and high (d) roughness micropatterned Si surfaces. While flat Si surface is hydrophilic ($\theta = 74^{o}$), low and medium roughness were hydrophobic (110^{o} & 124^{o}, respectively). High roughness Si micropattered surface was superhydrophobic (152^{o}). Therefore, by solely changing the surface roughness, the wetting response of the surface could be tuned in a controllable manner.

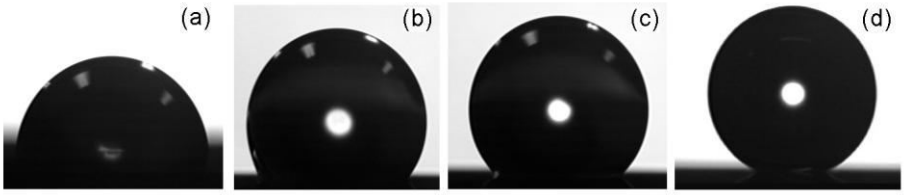

Fig.4.3: Photographs of water droplets on the respective patterned Si surfaces of different roughness: flat (a), low (b); mid (c) and high (d) roughness.

4.2 Effect of surface modification on the morphological and chemical characteristics of the micropatterned silicon substrates

Regardless of the intrinsic features of a biomaterial, the primary effects *vis-a-vis* biocompatibility depend on their surface, which comes in direct contact with the biologic material. Consequently, the properties of the outermost layers of a material are critically important in determining both biological responses to implants and material responses to the physiological environment. The knowledge of the surface properties of the culture substrates provides a good insight into how the substrate properties can influence cell adhesion and protein adsorption. Therefore, when a new biomaterial is being developed, an in depth characterization of its surface properties needs to precede the biological studies, where the material's surface properties will be correlated to biological responses [K. Dee *et al*., 2003].

4.2.1 Effect of thermal treatment

The micropatterned silicon substrates were subjected to different thermal treatments. In order to characterize the surface properties of the different micropatterned substrates regarding the surface chemistry and wetting response, static contact angle and X-ray photoelectron spectroscopy (XPS) elemental analysis measurements, respectively, have been performed after the following micropatterned Si substrate manipulations: 1) thermal treatment in an autoclave (saturated steam/water vapor of 1 atm at 121 °C) (AC substrates), 2) thermal treatment in a tube furnace (at 1000^{o}C for 30 min) (O substrates), 3) thermal treatment in a tube furnace and post-treatment in the autoclave (OA substrates). Micropatterned silicon substrates without any treatment have been used as control (C substrates).

In order to monitor the changes in wetting properties of the micropatterned Si substrates subjected to different thermal treatments, the wetting angles have been measured in all cases. The corresponding contact angles are listed in Table 4.3. Before any thermal treatment all three micropatterned silicon substrates were hydrophobic ($\theta > 90^{o}$) compared to the flat silicon substrate ($\theta = 74^{o}$). This hydrophobic response increased with increasing roughness in a monotonic way, i.e. the higher the substrate roughness the higher the contact angle. More specifically, low and mid roughness substrates were hydrophobic ($\theta = 110^{o}$ & 124^{o}, respectively) while the high roughness one was superhydrophobic ($\theta=152^{o}$).

Following thermal treatment in the autoclave conditions, all substrates (both flat and micropatterned) became more hydrophilic/less hydrophobic. Flat Si showed a remarkable decrease in contact angle (i.e. an increase in hydrophilicity) of 33^{o} (from ~74^{o} to ~ 41^{o}). However, the micropatterned surfaces exhibited a more pronounced hydrophilic response. Indeed, the water drop completely wetted the micropatterned region without spreading beyond the borders of it towards the

flat surface ("pool effect" configuration). In this case, the static contact angle was close to zero and the surface is regarded as superhydrophilic. The observed inhibition of the water droplet from spreading towards the flat surface, can be due to the large difference in the contact angle values between the flat and the micropatterned area, which reflects a similar variation in the respective surface energy values Remarkably, the spreading rate of the drop (i.e. how fast the drop spreads out the micropatterned surface) was increased with increasing roughness in a monotonic way, i.e. the higher the substrate roughness the higher the spreading rate.

Following contact angle measurements, all substrates were immersed into 10% hydrofluoric acid (HF) solution for 15 minutes, and the respective wetting angles were measured again. According to the measurements, listed in Table 4.3 (CAF column), the contact angles of all measured surfaces were practically recovered to their initial values before thermal treatment (C column). In particular, the contact angle of the low, mid and high roughnesss substrates rose up to 107, 122 & 150^{o}, respectively. Therefore, the hydrophilic and superhydrophilic rough micropatterned substrates had switched back into their hydrophobic and superhydrophobic state, respectively.

After thermal treatment in a tube furnace (at 1000^{o}C for 30 min), all substrates (both flat and micropatterned) became more hydrophilic. However, this decrease in hydrophobicity was more striking as the roughness increased. More specifically, while flat Si showed a (small) decrease in contact angle (i.e. an increase in hydrophilicity) of 50^{o} (from ~74 to ~ 29^{o}), low, mid and high roughness substrates showed a decrease of 89^{o} (from ~110 to ~ 21^{o}), 103^{o} (from ~124 to ~ 21^{o}) and almost 150^{o} (from 152 to 0^{o}), respectively. The water drop wet completely the surface. Therefore, the hydrophobic (low and mid roughness) and superhydrophobic (high roughness) micropatterned substrates had switched into hydrophilic and superhydrophilic surfaces, respectively.

Table 4.3: Contact angle values after different treatment steps*.

Substrate Type	**Wetting angle After different treatments (°)**				
	C	**O**	**AC**	**OA**	**CAF**
Flat	74	29	41	29	75
Low roughness	110	21	Superhydrophilic	Superhydrophilic	107
Mid roughness	124	21	Superhydrophilic	Superhydrophilic	122
High roughness	152	0	Superhydrophilic	Superhydrophilic	150

* Successive measurements were reproducible within ± 1°. (Abbreviations indicate the different treatment procedures: C: After fabrication/ before thermal treatment (Control); O: after thermal treatment in a tube furnace (at 1000°C for 30 min); AC: After thermal treatment in autoclave; OA: after thermal treatment in a tube furnace and post-treatment in the autoclave); CAF: After immersion in 10% HF solution

In order to characterize the surface chemistry of the different micropatterned substrates, XPS elemental analysis has been performed on the micropatterned Si substrates of high roughness(Fig. 4.4, Fig. 4.5 and Table 4.4). The Si_{2p} core level spectrum from the control (C) silicon substrate shows two distinct peaks: one at 100.0 eV and one at 103.6 eV. According to literature, the first peak is attributed to the bulk silicon (Si_{bulk}) and the second one to the fourth oxidation state (Si^{4+}) of the native oxide being formed on the silicon. The latter peak corresponds to the SiO_4 tetrahedron, as in SiO_2 (as it was shown in Fig. 1.16 of Paragraph 1.7.1) [M. Morita *et al.*, 1990, M. Kisa, 2004]. This, so called native oxide, is a layer of oxide which is built up on the surface, when a clean Si surface is exposed to atmosphere at room temperature [A. Bayati *et al.*, 1991]. The oxide film, developed under such conditions, soon ceases to thicken, because it forms a solid barrier between the metal and atmospheric oxygen through which ions have difficulty to move. Therefore, although the control (C) micropatterned Si substrate had not been subjected to any thermal treatment, a native oxide layer has been formed on its surface.

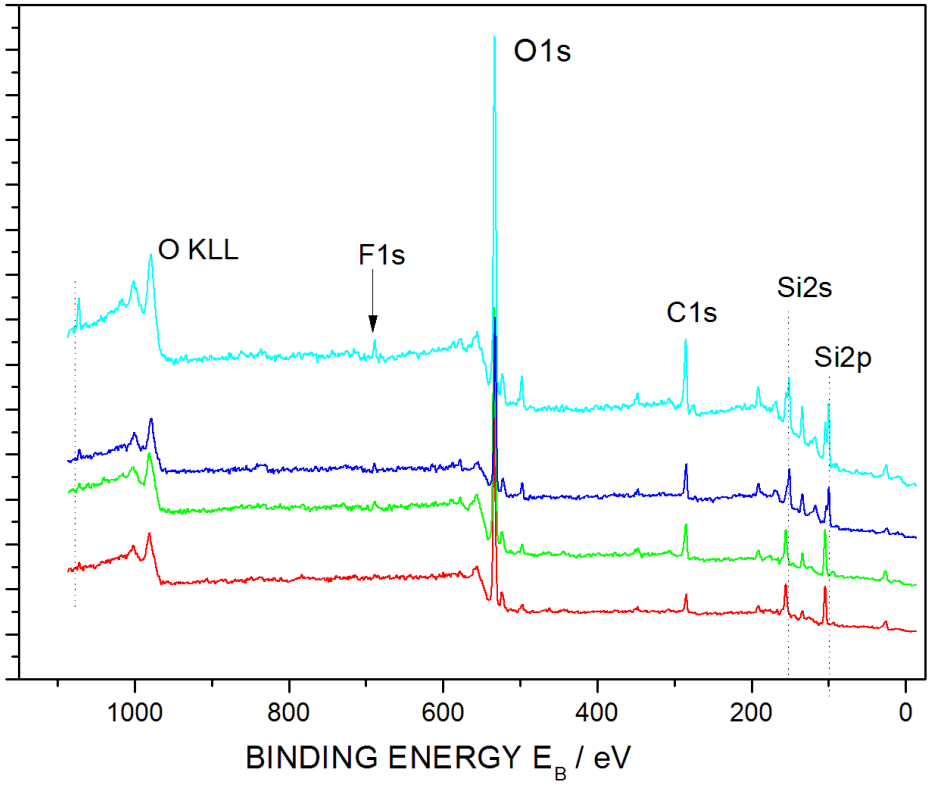

Fig. 4.4: Wide XPS scans of micropatterned Si substrates after different treatments: autoclave (AC substrate)

(cyan), control (C) (blue) and after post treatment (OA) (green) and (O sample) (red) silicon substrates

Regarding the silicon surface after thermal treatment in an autoclave (AC substrate), the Si_{2p} core level spectrum also showed two distinct peaks: one at 100.1 eV and one at 104.6 eV. These peaks were (also) attributed to the bulk silicon (Si^0) and the oxidation state (Si^{4+}), respectively. The first peak did not shifted compared to the respective one of the C sample. On the contrary, the value (104.6 eV) of the peak for the oxidative state (Si^{4+}) was shifted by 1eV to higher Binding Energies (B.E.) when compared to the C sample (103.6 eV). Furthermore, the (Si^0) peak was lowered in AC sample compared to the C sample. These results were quantitatively evaluated by the $I_{Si(0)}$ / $I_{Si(+4)}$ ratios. $I_{Si(0)}$ / $I_{Si(+4)}$ was calculated as 2.37 and 1.35 for C and AC sample, respectively.

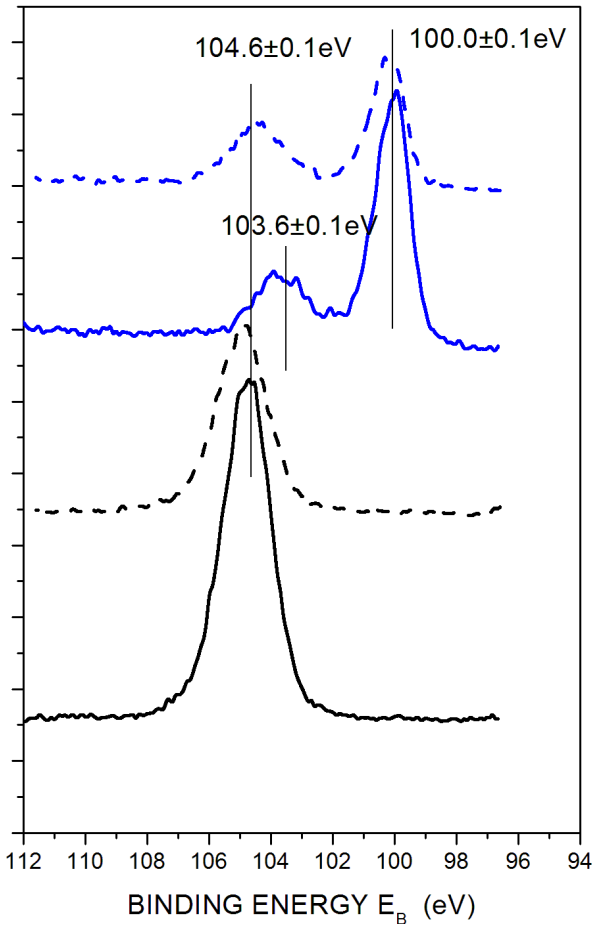

Fig. 4.5: Si_{2p} XPS spectra of micropatterned Si substrates after different treatments: autoclave (AC substrate) (dashed blue), control (C) (blue) and after post treatment (OA) (dashed black) and (O sample) (black) silicon substrates

Thermally treated Si substrates at 1000°C exhibited only one peak. More specifically, thermally

oxidized substrates before (O sample) and after post treatment (OA) showed a peak at 104.7 & 104.8 eV, respectively (Fig. 4.5). These peaks were attributed to the oxidation state (Si^{4+}).

Table 4.4: The binding-energies of Si_{2p} photoemission peak for the high roughness substrate*.

Substrate Type	Binding Energy (± 0.1 eV)	
	Si^{+4}	Si^{0}
C	103.6	100.0
AC	104.6	100.1
O	104.7	-
OA	104.8	-

*(Abbreviations indicate the different treatment procedures- C: After fabrication/ before treatment (Control); O: after thermal treatment in a tube furnace (at 1000°C for 30 min); AC: After thermal treatment in autoclave; OA: after thermal treatment in a tube furnace and post-treatment in the autoclave)

In order to explain the nature of the oxides being formed on the different micropatterned substrates, the principles of the oxidation process have been taken into consideration and explained in detail in Paragraph 1.7.1. In this context, XPS analysis confirmed that on both the control substrate (C) and AC samples, a thin natural oxide (SiO_2) layer was formed. In the case of AC, this thin layer was slightly thicker compared to the C, as indicated by the shift towards higher B.E.s and the decrease of the $I_{Si(0)}/I_{Si(+4)}$ ratio. When the micropatterned Si substrates had been thermally treated in a tube furnace at high temperature, a thick SiO_2 layer was formed, as confirmed by the striking presence of a Si^{+4} peak and the absence of the Si^0 peak. As explained in 1.7.1, when the oxide layer is thick enough, the oxide films exhibit only the XPS shift characteristic of bulk SiO_2 in the region of approximately 104.0 eV. The thickness of this oxide layer could be estimated from the presented results to be approximately 100nm.

It has to be mentioned that except from the main peaks of Si and O, some other peaks could be seen in the wide scans (Fig. 4.4). These were attributed to fluorine (F) and carbon (C). Regarding the peak for fluorine, this could be attributed to fluorine radicals. The detection of fluorine in the surface was due to the environment (500 Torr SF_6 gas) under which the laser irradiation was taking place. It has been demonstrated that for intense femtosecond irradiation at 800nm, gas-phase photodissociation of SF_6 produces fluorine radicals. These radicals react with silicon and form SiF_x compounds [V. Zorba, 2007]. The high concentration of carbon on the surface is probably due to the fact that the sample was not cleaned before the analysis and originates from contamination of the surface after autoclaving.

4.2.2. Effect of collagen coating

Preadsorption of certain kinds of proteins onto a solid substrate greatly increases adhesiveness to many kinds of cells. Such proteins are called adhesion proteins [B. Ratner *et al*., 2004] and include collagen, fibronectin, polyDlysine, laminin, etc. For the *in vitro* assays using cell types, such as PC12 cells, collagen preadsorption of the surfaces is usually necessary [L. Greene et al., 1998; Andrea M. Vincent and Eva L. Feldman, 2010]. In this respect, micropatterned silicon substrates were immersed into a 2% rat tail collagen solution. In order to characterize the wetting properties of the different micropatterned substrates, static contact angle measurements have been performed after the following micropatterned Si substrate manipulations: 1) thermal treatment in an autoclave and immersion in collagen solution (AL substrates), 2) thermal treatment in an autoclave, immersion in collagen solution and then rinse with PBS (ALR substrates), 3) thermal treatment in a tube furnace, thermal treatment in an autoclave, immersion in collagen solution and finally rinse with PBS (OL substrates) and 4) UV sterilization and immersion in collagen solution (UL substrates). Micropatterned Si surfaces were surrounded by a large flat Si area. Micropatterned silicon substrates without any treatment have been used as control (C substrates).

In order to study how the wetting properties of the micropatterned Si substrates changes after the different treatments, the wetting angles of the differently treated surfaces have been measured (Table 4.5). Before any thermal treatment all three micropatterned silicon substrates were hydrophobic ($\theta > 90^o$) compared to the flat silicon substrate ($\theta = 74^o$). This hydrophobic response increased with increasing roughness in a monotonic way, i.e. the higher the substrate roughness the higher the contact angle. More specifically, low and mid roughness substrates were hydrophobic ($\theta = 110^o$ & 124^o, respectively) and high roughness was superhydrophobic ($\theta>150^o$).

Thermally treated substrates in an autoclave became less hydrophobic after their immersion in collagen solution and without further rinse (AL substrates) (Table 4.5, AL column). More specifically, flat Si showed a (small) decrease in contact angle (i.e. an increase in hydrophilicity) of 18^o (from ~75 to ~57^o). The micropatterned surfaces, however, exhibited a distinct wetting response. The water drop wet completely the micropatterned region and didn't extend beyond the borders towards the flat surface ("pool effect" configuration). In this case, the static contact angle could not be measured and the surfaces were regarded as superhydrophilic. This difference in contact angle values between the flat and the micropatterned surface, which reflects a difference in the respective surface energy values, inhibited the water drop from extending towards the flat surface. Remarkably, the spreading rate of the

drop increased with increasing roughness in a monotonic way, i.e. the higher the substrate roughness the higher the spreading/wetting rate. Thermally treated substrates at 1000^{o}C (OL substrates) and UV treated (UL substrates) exhibited a similar response (Table 4.5, OL and UL column, respectively). Flat Si became more hydrophilic, while all micropatterned substrates became superhydrophilic.

On the contrary, when the thermally (in an autoclave) treated substrates were rinsed with PBS after their immersion in the collagen solution (ALR substrates), this distinct wetting response of the micropatterned surfaces was lost. More specifically, when positioning the water drop on the micropatterned surface, the water volume spread beyond the borders of the rough surface and into the flat Si surface. This was observed for all types of roughness. In these cases, the surfaces can be regarded as superhydrophilic, while it seems that there was practically no surface energy difference between the flat and the micropatterned surface. This could be attributed to absence of a conformal layer of the collagen on the surface and the presence of hydrophilic channels that drive the water volume towards the flat surface. In this case, it seems as if surface roughness plays no role.

Table 4.5: Contact angle values after different treatment steps.*

Substrate Type	**Wetting angle After different treatments (°)**				
	C	**AL**	**ALR**	**OL**	**UL**
Flat	74	57	51	52	42
Low roughness	110	Superhydrophilic	Superhydrophilic	Superhydrophilic	Superhydrophilic
Mid roughness	124	Superhydrophilic	Superhydrophilic	Superhydrophilic	Superhydrophilic
High roughness	152	Superhydrophilic	Superhydrophilic	Superhydrophilic	Superhydrophilic

*Successive measurements were reproducible within ± 1°. (Abbreviations indicate the different treatment procedures: C: After fabrication/ before thermal treatment (Control); AL: after thermal treatment in an autoclave and immersion in collagen solution; ALR: after thermal treatment in an autoclave, immersion in collagen solution and then rinse with PBS, OL: after thermal treatment in a tube furnace, thermal treatment in an autoclave, immersion in collagen solution and finally rinse with PBS and UL: after UV sterilization and immersion in collagen solution

4.2.3 Effect of serum protein adsorption

The majority of cell types require the addition of serum in the culture medium to ensure survival and growth *in vitro*. When a surface is exposed to a protein solution, like serum, it becomes

coated within seconds to minutes, with a monolayer of proteins. Hence, the host cells do not "see" the material, but instead they "see" a dynamic layer of proteins adsorbed on the surface (Paragraph 1.3.2). To this respect, micropatterned silicon substrates were immersed into growth medium solution (GM) supplemented with 10% fetal bovine serum (FBS), which was the standard culture medium used herein. In order to characterize the wetting properties of the different micropatterned substrates, static contact angle were evaluated after the following micropatterned Si substrate manipulations: 1) thermal treatment in an autoclave and immersion in GM (AS substrates) and 2) thermal treatment in an autoclave, immersion in GM and then rinse with PBS (ASR substrates).

In order to study how the wetting properties of the micropatterned Si substrates change after the protein adsorption, the wetting angle has been measured. The corresponding wetting angles are listed in Table 4.6 and compared to the respective values before immersion in the protein solution. Thermally treated flat substrates became less hydrophobic after their immersion in GM solution and without rinse (AS substrates) (Table 4.6, AS column). However, the water drop had not a constant shape in the whole surface, which implies that the proteins form the serum had been absorbed on the surface in a non homogeneous manner. Regarding the micropatterned surfaces, all became superhydrophilic, independent of roughness type. More specifically, when positioning the water drop on the micropatterned surface, it spread beyond the borders with the flat surface. This was observed for all roughness types. In these cases, the surfaces are regarded as superhydrophilic. The same wetting response was observed after rinsing the substrates with PBS (ASR substrates) (Table 4.6, ASR column).

Table 4.6: Contact angle values after different treatment steps.*

Substrate Type	**Wetting angle After different treatments (°)**		
	C	**AS**	**ASR**
Flat	74	Non homogenous drop shape (Strange irregular shape)	Non homogenous drop shape (Strange irregular shape)
Low roughness	110	Superhydrophilic	Superhydrophilic
Mid roughness	124	Superhydrophilic	Superhydrophilic
High roughness	152	Superhydrophilic	Superhydrophilic

* Successive measurements were reproducible within ± 1°. (Abbreviations indicate the different treatment

procedures: C: After fabrication/ before thermal treatment (Control); AS: after thermal treatment in an autoclave and immersion in the growth medium solution (GM);

4.3 In vitro experiments with cells- PC12 cells

4.3.1 Effect of surface roughness on PC12 cell growth

As an initial attempt, PC12 cells were used to assess whether the laser-structured rough Si substrates could support cell growth in the absence of growth factor after 4 and 7 days of culture. Cell growth was assessed by qualitative (via imunocytochemistry and scanning electron microscopy-SEM) and quantitative (computer-based image analysis of DAPI nuclear staining) morphological methods. It was shown that the oxidized structures did not support PC12 cell growth, since minimal adhesion was observed (data not shown). Therefore, further analysis concentrated on the non-oxidized non-coated or collagen coated substrates. Morphological analysis with SEM showed that PC12 cells were grown on all three roughness types, while sharing the same morphological characteristics, including the relatively small and rounded shape cluster formation (Figure 4.6A). In order to quantitatively evaluate cell outgrowth on the different substrates, upon culture termination, scaffolds were stained with DAPI and the number of nuclei/mm^2 surface area was evaluated using ImageJ (Figure 4.6B). The mean cell number in each band of the microstructured area (flat, low, medium and high roughness) was calculated and expressed as a percentage over the total number of cells counted onto the whole microstructured area. Thus, after 4 days of culture, non coated substrates supported growth of 47.5% of the cells in the low-roughness band, 30.7% in the medium-roughness band and 18.9% in the high-roughness band, while only 5% in the flat band. At day 7 of culture, the percentage of cells on the low-roughness band increased to 51.8%, while on the other bands cell growth did not show any statistically significant change (Figure 4.6Ba). Thus, in the absence of NGF, although PC12 cells did not differentiate to develop neurites, they seemed to prefer the low-roughness structures for growth. Using the collagen coated substrates, cells were shown to grow better on the medium-roughness bands (47.3% of total cells) at day 4 of culture, while they did not seem to have any preference on band roughness at day 7 of culture (Figure 4.6Bb). It is interesting to note that at day 4 of culture MC surfaces were largely preferred to flat ones (two- to eight-fold higher proliferation; Figure 4.6B), while flat surfaces could not support cell growth after day 7 of culture.

A detailed report of the absolute values of the cell density range for the different rough surfaces at the different culture times follows: For non coated substrates the cell number varied from 620 to 3301N_{cells}/ mm^2 for low, from 525 to 1522N_{cells}/ mm^2 for medium and from 295 to 783N_{cells}/ mm^2 for high roughness substrates (4DIV). The cell number varied from 319 to 1871N_{cells}/ mm^2 for low, from 145 to 1490 N_{cells}/ mm^2 for medium and from 70 to 1219 N_{cells}/ mm^2 for high roughness substrates (7DIV). For collagen-coated substrates the cell number varied from 131 to 1660 N_{cells}/ mm^2 for low,

from 408 to 1576 N_{cells}/ mm^2 for medium and from 75 to 1345 N_{cells}/ mm^2 for high roughness substrates (4DIV). The cell number varied from 601 to 1988 N_{cells}/ mm^2 for low, from 1037 to 2052 N_{cells}/ mm^2 for medium and from 141 to 2566 N_{cells}/ mm^2 for high roughness substrates (7DIV).

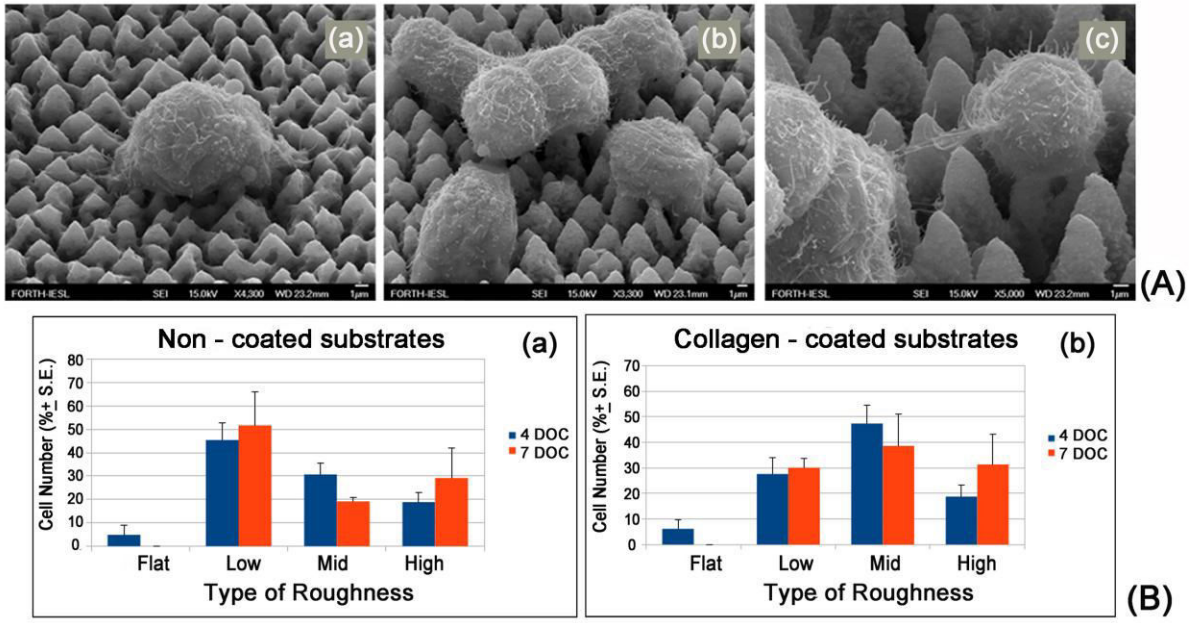

Figure 4.6: PC12 cells in their undifferentiated state. (A) SEM images of PC12 cells in their undifferentiated state on Si micro-patterned surfaces of low (a), medium (b) and high roughness (c). (B) Numbers of PC12 cells growing on three-band laser-patterned Si substrates for 4 and 7 days of culture (DOCs) in the absence of stimulus. PC12 cells were cultured on non-coated substrates (a) or collagen-coated substrates (b). Upon culture termination, the scaffolds were stained with DAPI and the number of nuclei/mm ^{2} surface area was evaluated using ImageJ analysis software. The results are expressed as percentages of cell numbers in each patterned band area compared to the total three-band area (± standard error of the mean, SE). The results represent the means of five different experiments (n=30 fields of view for each roughness type and time of culture).

4.3.2 Effect of surface roughness on PC12 cell growth in the presence of NGF

PC12 cells were placed onto the Si structures and induced to differentiate towards the neuronal lineage by stimulation with NGF, which is considered to be the classical inducer of PC12 cell differentiation into a sympathetic neuron phenotype [L.Greene and A. Tischler, 1976]. NGF (50ng/ml) induced differentiation of PC12 cells was assessed by qualitative (via immunocytochemistry, SEM) and quantitative (computer-based image analysis) morphological methods.

Qualitative analysis included immunocytochemical staining for specific protein expression and

morphology assessment using SEM imaging. Immunocytochemical studies indicated that cells growing on the low and medium roughness MCs could differentiate towards the neuronal cell lineage, showing increased, flattened cellular bodies, sprouting neuritic processes. These processes expressed neuron-associated βIII-tubulin (green staining in Figure 4.7A, 4.7Ba, 4.7Bb), with the distal end regions showing thin filaments sprouting outwards the expressed actin (red filaments in Figure 4.7A, 4.7Ba, 4.7Bb). Such actin-based extensions that facilitate axon development and guidance could represent the terminal filopodia of growth cones. On the contrary, despite the presence of NGF stimulus, cells did not appear to differentiate on the MC surfaces of the highest roughness. In this case, the cells displayed round morphology, were covered with microvilli, exhibited short or no processes and grew to form cell clusters (Figure 4.7Bc), resembling untreated PC12 cells. This differential cell response in the presence of NGF on the different substrates was also confirmed by SEM imaging, showing that at low (Figure 4.7.Ca, 4.7Cd) and medium (Figure 4.7Cb, Ce) roughness parts of the substrates, the cells mostly exhibited a bipolar shape, forming an elegant neurite network, while at the highest roughness (Figure 4.7Cc, Cf) the cells mostly maintained their round shape.

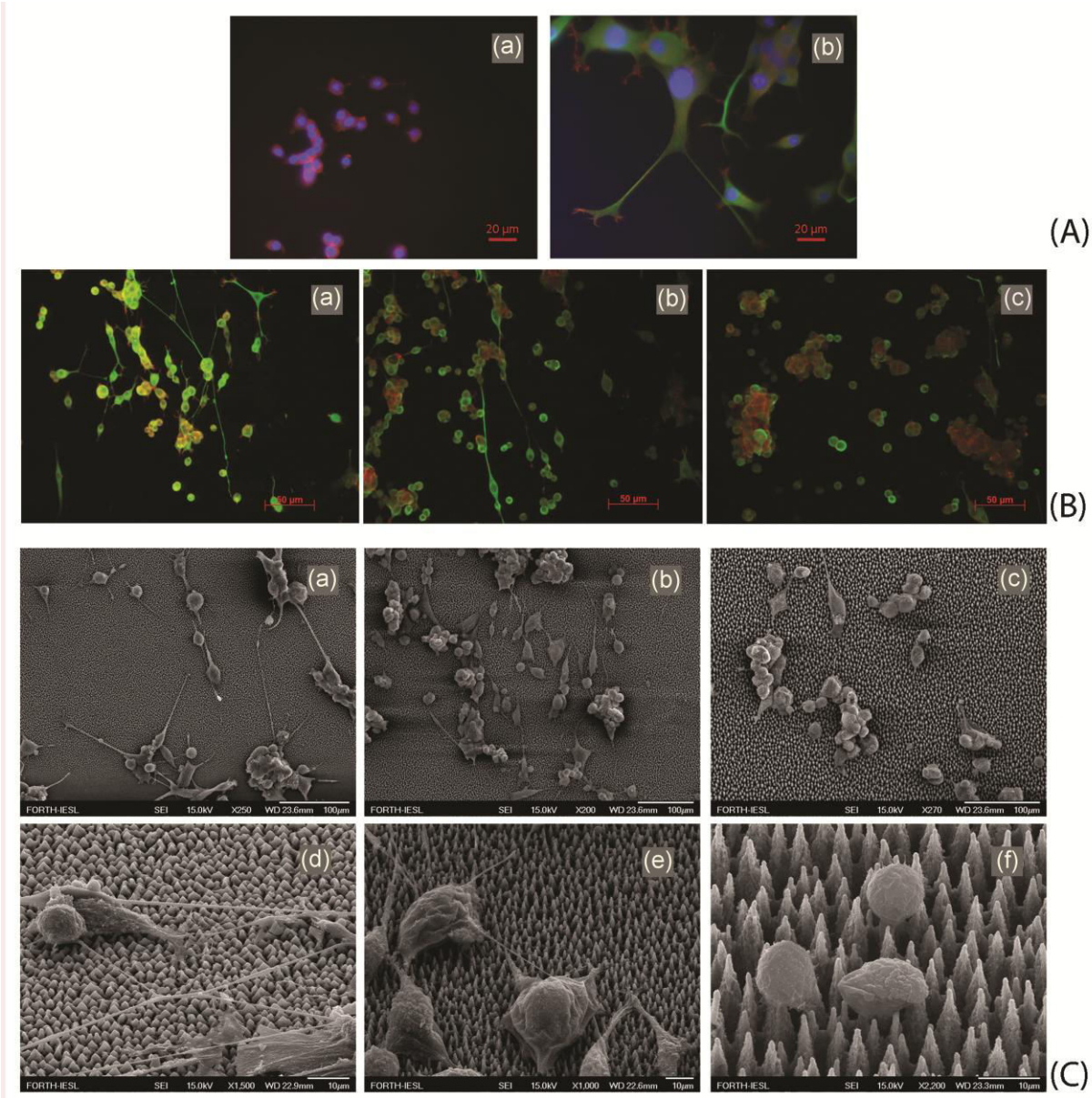

Figure 4.7: (A) Effect of NGF on PC12 cell morphology: Morphological analysis of PC12 cells with fluorescence microscopy before (i) and after (ii) treatment with NGF. Double labeling with beta-tubulin(green) and actin (red) of PC12 cells; blue: DAPI nuclear staining (4 Days of Culture). (B, C) Effect of surface roughness on PC12 cell differentiation: Confocal microscopy (B) and SEM images (C) of NGF-treated PC12 cells on collagen coated micropatterned Si substrates of different roughness after 4 Days of Culture: low roughness substrates (i) & (iv); medium roughness substrates (ii) & (v); high roughness substrates (iii) & (vi).

In order to quantitatively evaluate PC12 cell differentiation, the percentage of differentiated cells and neurite lengths in the presence of NGF were estimated. As already noted in the Methods section, the percentage of differentiated cells was calculated from the ratio of cells displaying neuron-like processes over the total number of cells. The results showed that, for the collagen coated

substrates, cell differentiation was promoted only by patterned surfaces of low and medium roughness (26.4% and 18.3% at day 4 of culture and 24.9% and 12.66% at day 7 of culture, respectively), whereas it was strongly inhibited on surfaces of high roughness (only 4.14% and 0.96% at days 4 and 7 of culture, respectively; Fig. 4.8). Similar results were obtained with the non-coated substrates (data not shown). Therefore, it is important to note that the observed differentiation ratio was independent of the substrate's biochemical coating, since non-coated and collagen coated substrates gave similar results.

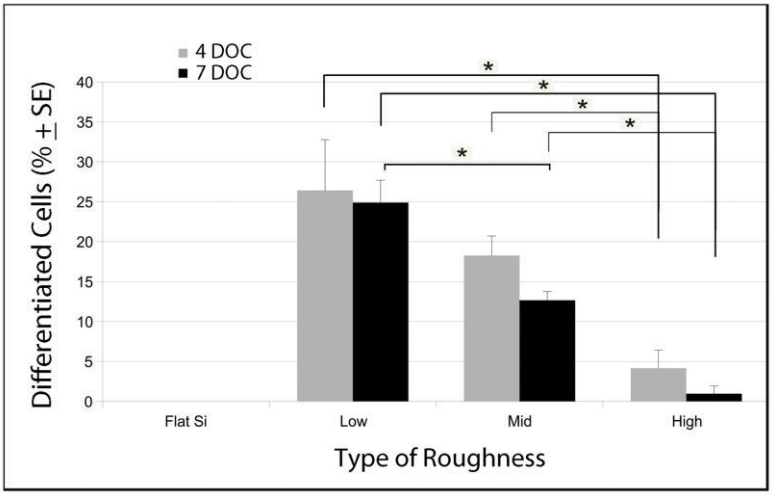

Figure 4.8: Effect of NGF treatment on differentiation: NGF-induced differentiation and growth of PC12 cells on laser patterned Si substrates coated with collagen. PC12 cells were treated with 50ng/ml NGF for 4 and 7 days (DOC). Cells with at least one neurite with a length equal to the cell body diameter were counted and expressed as percent of the total number of cells in a field (± SE,Standard Error of the Mean). The significance levels (p) were calculated using the ANOVA followed by Tukey test for multiple comparisons between pairs of means (*: $p<0.01$, n=30 cells for each roughness type and time of culture). The difference between surfaces of low and medium roughness and the flat surface was highly significant ($p< 0.001$).

Neurite lengths of differentiated cells grown on the collagen-coated substrates at day 4 of culture were shown to be higher at low roughness (66.7 ±9.6 μm as compared to 41.1±3.7μm and 28.0 ± 4.2 μm at medium and high roughness, respectively), while at day 7 of culture low and medium roughness were shown to support equally well longer neurite growth (79.0 ± 7.4 μm and 82.7 ± 12.3 μm as compared to 30.1 ±5.5 μm at high roughness, respectively) (Table 4.7). It has to be noted that at high roughness MCs the number of cells analysed from the images was very small (n=8 and n=11 for 4 and 7 DIV, respectively), since, as previously mentioned, this surface could not support PC12 cell differentiation. Non-coated surfaces of low and medium roughness could equally well support neurite growth at day 4 of culture, while no neurites grew on high-roughness substrates (data not shown). In

this case, at day 7 of culture neurite growth was limited, since differentiation was obtained in only a few cells (data not shown).

Table 4.7: Effect of NGF treatment on neurite growth.

Roughness* Type	**4 DOC $L_{neurite} \pm$ S.E. (µm)**	**7DOC $L_{neurite} \pm$ S.E. (µm)**
Low	66.7 ± 9.6	79.0 ± 7.4
Medium	41.1 ± 3.7	82.7 ± 12.3
High	28.0 ± 4.2	30.1 ± 5.5

* NGF-induced differentiation and growth of PC12 cells on laser patterned Si substrates coated with collagen. PC12 cells were treated with 50ng/ml NGF for 4 and 7 days (DOC). The length of the longest neurite was determined for cells with at least one identified neurite. The results are expressed as mean length (± SE, Standard Error of the Mean). Experiments were repeated at least five times using cultures prepared on separate days (n=30 cells for each roughness type and time of culture).

It has also to be mentioned that although differentiated cells grew on top of the surfaces, it seemed that they sensed the scaffold features via the tips of their neurite extensions (Fig. 4.9).

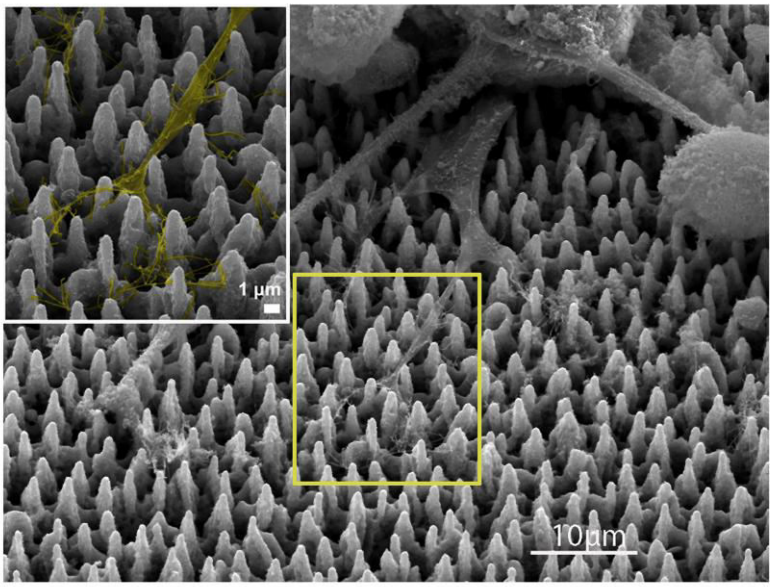

Figure 4.9:'Sensing' substrate roughness: SEM image of differentiated PC12 cells after NGF treatment on laser-patterned Si substrates. Inset is a higher magnification image focusing on sprouting filopodia (pseudocoloured)

4.4. *In vitro* experiments with cells- Primary cells

4.4.1 Effect of surface roughness on Schwann cell growth and morphology

As an initial attempt, Schwann cells were used to assess whether the laser-structured rough Si substrates could support cell growth without the need for protein coating. Cell growth was assessed by qualitative (via imunostaing with p75) and quantitative (computer-based image analysis of DAPI nuclear staining) morphological methods. It was shown that all three micro-patterned Si substrates could equally well support the growth of Schwann cells (Figure 4.10). In order to quantitatively evaluate cell outgrowth on the different substrates, upon culture termination, scaffolds were stained with DAPI and the number of nuclei/mm^2 surface area was evaluated using ImageJ (Figure 4.11). All micropatterned substrates could equally well support Schwann cell growth. Precisely, after 5 days of culture, 792 $\pm$147 and 808$\pm$126 cells/mm^2 developed on the medium and high roughness substrates, respectively. However, this growth rate was not significantly higher compared to the flat substrate (705$\pm$111 cells /mm^2). The weakest growth performance was seen on the low roughness substrates (515$\pm$140 cells /mm^2).

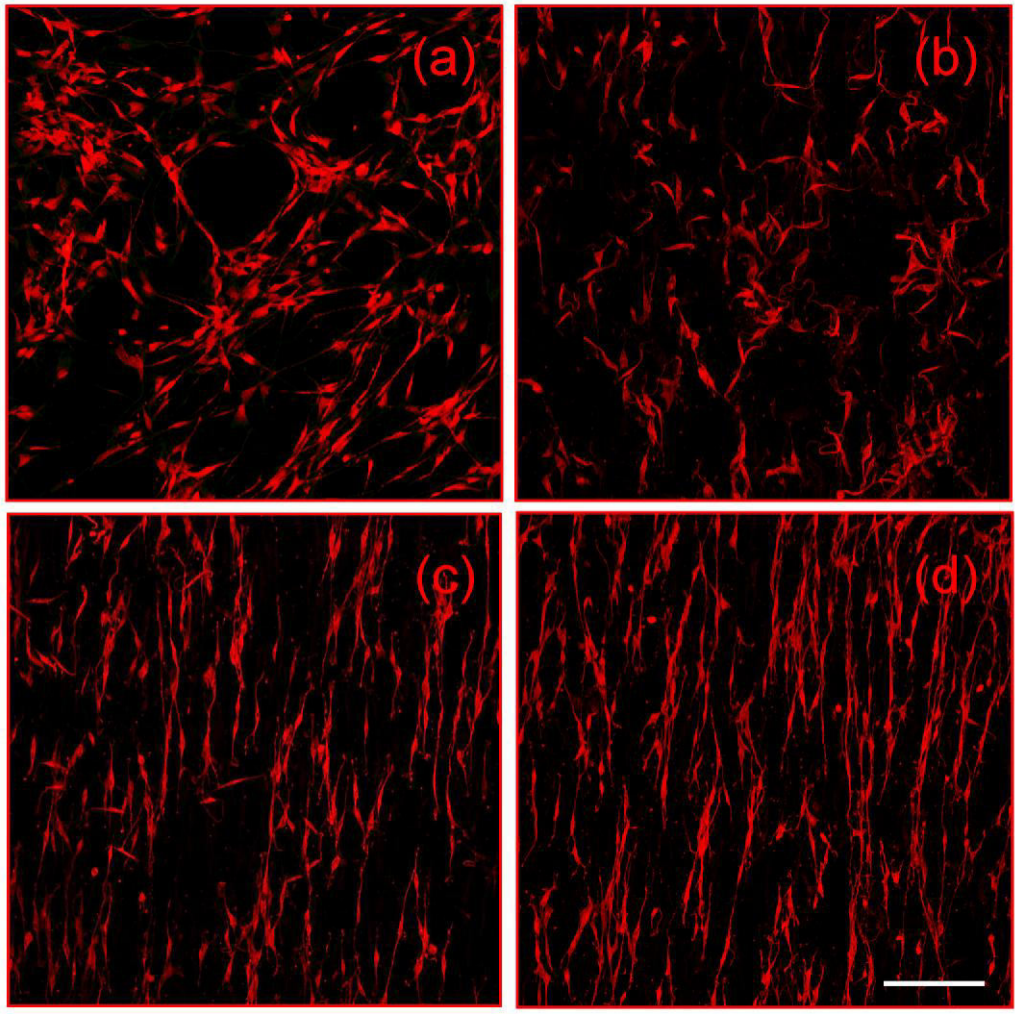

Fig. 4.10: Effect of substrate/surface roughness/topography on Schwann cell outgrowth. Confocal microscopy images of p75 positive Schwann cells grown on different silicon substrates for 5 days of culture: Flat (a), low (b), medium (c) and high (d) roughness Si substrates.Scale bar: 75 μm

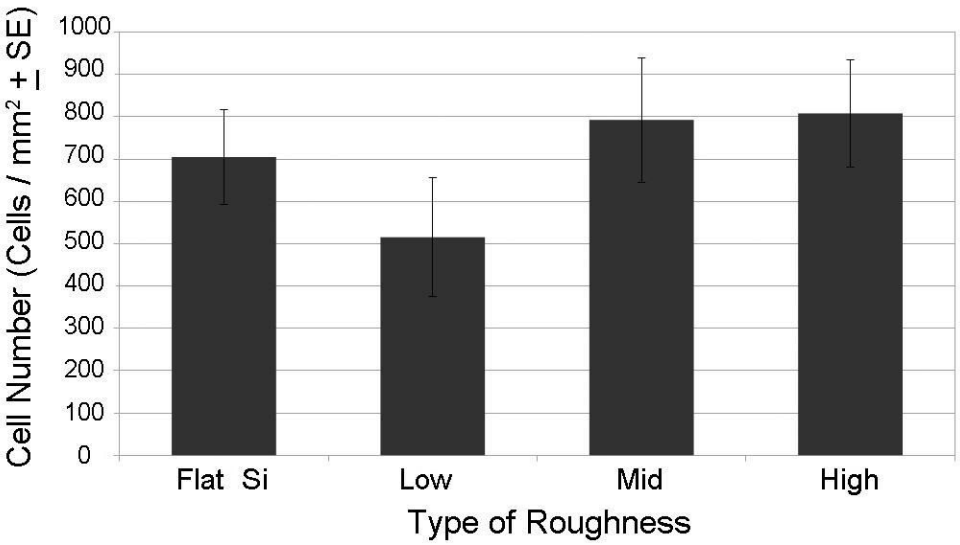

Fig.4.11: Numbers of Schwann cells grown on flat Si and laser micropatterned Si substrates of different roughness for 5 days of culture without coating. The results are expressed as cells/mm^2 (± standard error of the mean, SE) and represent the means of 3 different experiments (n=30 fields of view for each roughness type)

Remarkably, substrate roughness affected the growth orientation pattern of Schwann cells Fig. 4.10). In order to quantify this observation, the orientation of the cell nuclei was determined by measuring the angles between the major axis of the nuclear ellipse and the vertical axis of the image plane (Figure 4.12A). According to this analysis, Schwann cells displayed a broad range of orientation angles on low roughness Si substrates (34.8, 34.8 and 32.4% of the cells were outgrown at angles of 0-30^o, 30-60^o and 60-90^o, respectively). This response was similar to the orientation distribution of the cells on the flat unpatterned Si (34.4, 41.4 and 24.2% of the cells were outgrown at angles of 0-30^o, 30-60^o and 60-90^o, respectively). On the contrary, the majority of the Schwann cells on the medium and high roughness substrates were mostly aligned (77.2% and 78.8 % of the cells had an orientation angle of 0-30^o values, respectively). Therefore, there was a preferred cell outgrowth orientation towards the substrates with increased roughness. It is interesting to note that the cells seemed aligned with the orientation of the microcone/spike on the surface, which was accordingly more pronounced as the roughness increased (Paragraph 4.1).

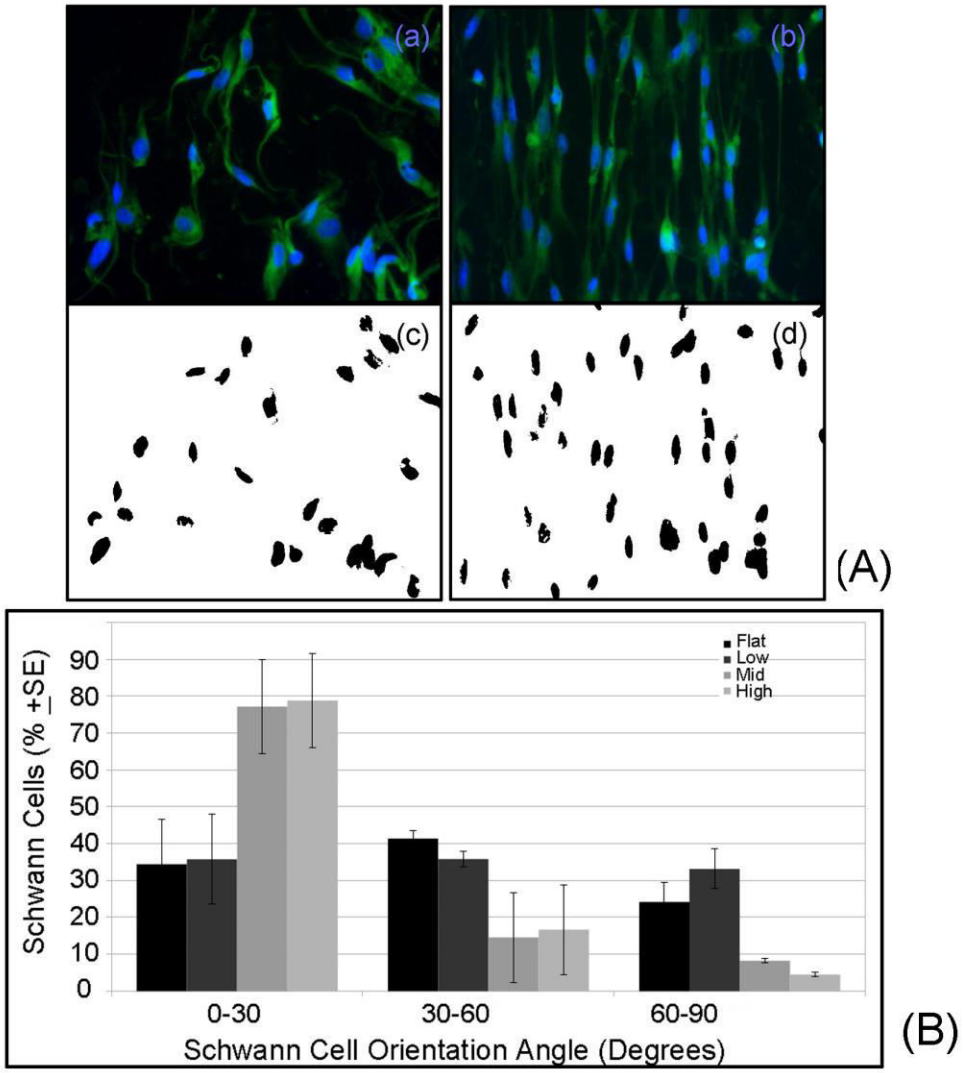

Fig. 4.12: Quantitative evaluation of Schwann cell outgrowth orientation. (A) Schwann cell visualization for image analysis: (a,b) composite fluorescence images showing both the entire Schwann cell body and its nucleus on a micropatterned Si substrate of low (a) and high (b) roughness substrate. Green fluorescence corresponds to FITC-conjugated anti-p75 staining, a Schwann cell marker. Blue fluorescence corresponds to DAPI, which stains the cell nucleus. The two fluorescent labels were imaged separately and overlayed to create the composite image. (c,d) Thresholded and binarized images showing the DAPI label of the Schwann cell nucleus. (B) Schwann cell orientation expressed in terms of the orientation angles' (frequency) distribution. The orientation angle of the nucleus, which was regarded as an ellipse, was measured as the angle between the major axis of the ellipse and the vertical axis of the image plane. The number of cells exhibiting an orientation angle value within a specific range is expressed as percentage of cells $\pm$ standard error of the mean. The results represent the means of three different experiments.

4.4.2 Effect of surface roughness on axonal growth and network formation of sympathetic dissociated neurons

The effect of microconical topography on neurite outgrowth and network formation was investigated using rat sympathetic neurons from the superior cervical ganglia. In order to quantitatively evaluate cell outgrowth on the different substrates, upon culture termination, scaffolds were stained with DAPI and the number of nuclei/mm^2 surface area was evaluated using ImageJ (Fig. 4.13). Although only a very few neurons could grow on the flat Si substrates (only 18.6 cells/mm^2), all micropatterned Si substrates did support the neuronal outgrowth. Thus, 107.3, 133.4 and 133.8 cells/mm^2 developed on low, medium and high roughness substrates, respectively, after 6 days of culture.

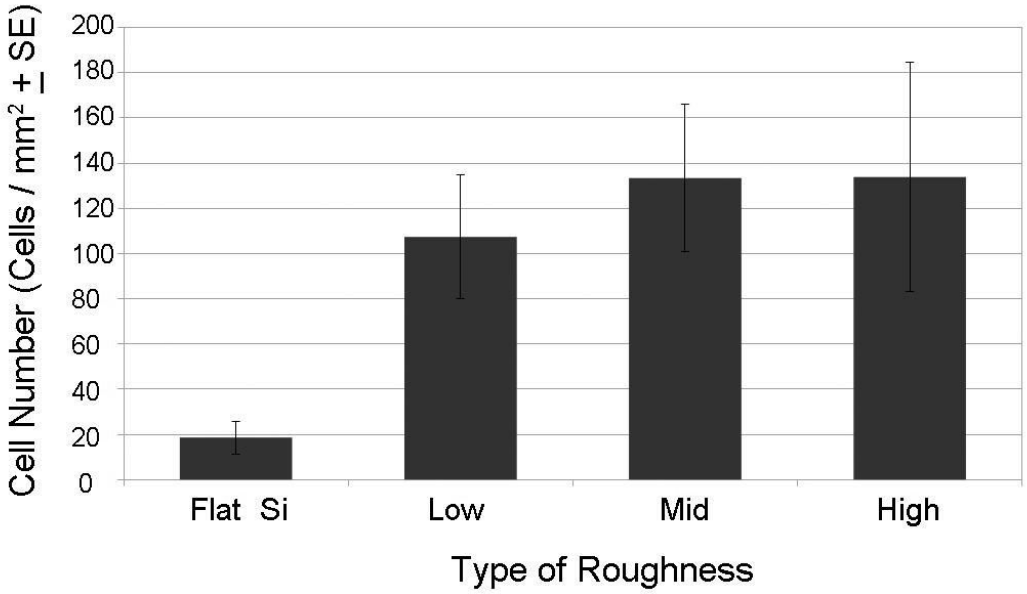

Fig: 4.13: Numbers of sympathetic neurons grown on flat and laser micropatterned Si substrates of different roughness for 6 days of culture (DOCs) after collagen coating. The results are expressed as cells/mm^2 $\pm$ standard error of the mean, SE) and represent the means of three different experiments (n=30 fields of view for each roughness type)

Sympathetic neurons and their neurites growing on the three different substrates were identified by neurofilament (NF200) immunoreactivity (Fig. 4.14). Impressive neuronal outgrowth and network formation could be observed on all three micropatterned silicon substrates of different roughness, however in a differential way. More specifically, the axons on the low roughness substrates (Fig. 4.14a) were shown to grow randomly, whereas the neurons on medium (Fig. 4.14b) and high (Fig. 4.14c) roughness substrates followed a parallel alignment growth pattern.

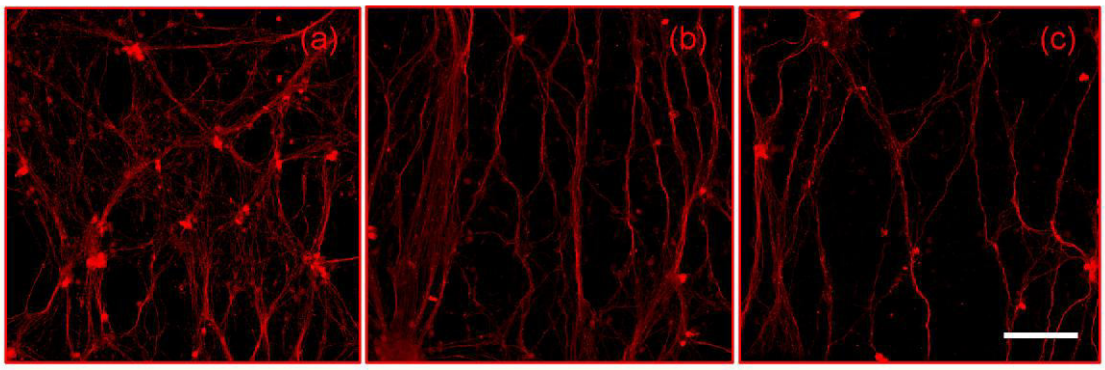

Fig.4.14: Effect of surface topography on neuronal growth. Confocal microscopy images of neurofilament positive sympathetic neurons grown on low (a), medium (b) and high (c) roughness micropatterned Si substrates for 6 days. Scale bar: 150 μm

In order to quantify this differentially oriented axonal outgrowth of neurons on the three substrates, the axon orientation angle has been measured (Fig.4.15) Although the growth was very sparse, the neurons on the flat Si substrates were equally distributed at all different angle orientations (30.2, 35.2 and 34.6% of the neurons had an orientation angle of 0-30^o, 30- 60^o and 60- 90^o values, respectively). Neurons on the low roughness substrates showed a slight orientation preference at 0-30^o angles (41.7, 35.1 and 23.2% of the neurons had an orientation angle of 0-30^o, 30- 60^o and 60- 90^o values, respectively). Neurons on medium roughness showed an increased preference to parallel alignment (58.5, 28.0 and 13.5 % of neurons had an orientation angle of 0-30^o, 30- 60^o and 60- 90^o values, respectively). Finally, the best conditions for parallel alignment was detected in the case of high roughness substrates (78.9, 15.3 and 5.8 % of neurons had an orientation angle of 0-30^o, 30- 60^o and 60- 90^o values, respectively). Thus, neuronal outgrowth orientation was highly influenced by substrate morphology and correlated with substrate roughness. It has to be noted that the cells seemed to follow and get aligned with the orientation of the microcone feature, which was accordingly more pronounced as the roughness increased (Paragraph 4.1).

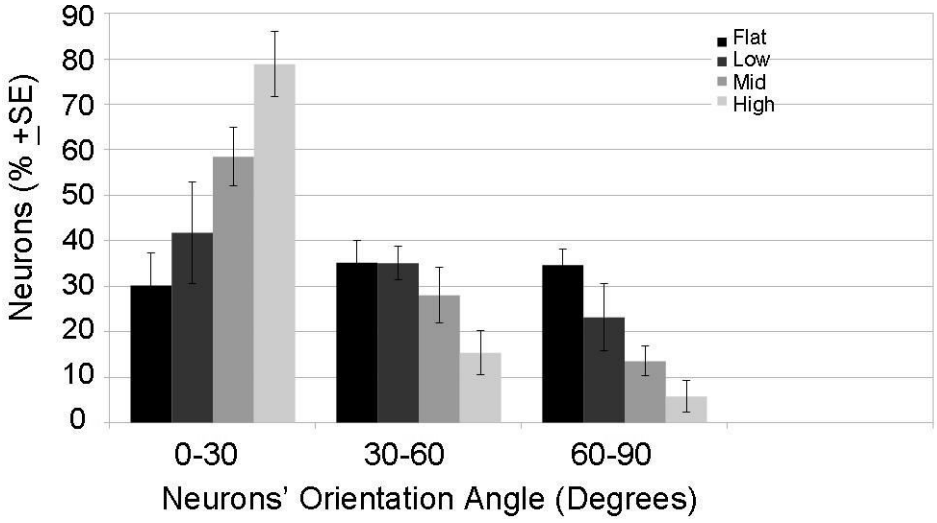

Fig.4.15: Quantitative evaluation of axonal outgrowth orientation. Axonal orientation is expressed in terms of the orientation angles' distribution. The orientation angle of each axon was measured as the angle between the axonal vector and the vertical axis of the image plane. The number of cells exhibiting an angle value within a specific range is expressed as percentage of cells ± standard error of the mean. The results represent the means of three different experiments

The neuronal network organization showed a striking influence by the different substrate morphology (Fig.4.16A). On the low (Fig.4.16Aa) and medium (Fig.4.16Ab) roughness substrates the network was dispersed and highly interconnected, consisting of mainly thin neurites with many branch points among them. On the contrary, the neurites grown on high (Fig.4.16Ac) roughness substrates were organized in thicker bundles and there were not so many connections among them. In order to quantify this fasciculation, the width of the axons (stained with anti-NF) on the low, medium and high roughness substrates have been measured and compared (Fig.4.16B). The majority of the axons on the low roughness substrates (~71%) had a diameter of 0-2.0 μm. The rest of the axons (23%) shared a diameter of 2-4 μm. The axonal growth on the medium roughness substrates showed a similar response with the one on the low roughness states (63% and 25% of the axons had diameters in the range of 0-2.0 μm and 2-4 μm, respectively). In the case of the high roughness substrates, only a small percent of the axons (~27%) had diameters in the range of 0-2.0 μm. Approximately 24, 14 and 13% of the axons had diameters in the range of 2-4.0 um, 4-6.0 μm and 6.0-8.0 μm, respectively. A smaller percentage of axonal bundles (9.4%) reached a thickness of 14 μm. Some few axons had also even thicker width (2.8%).

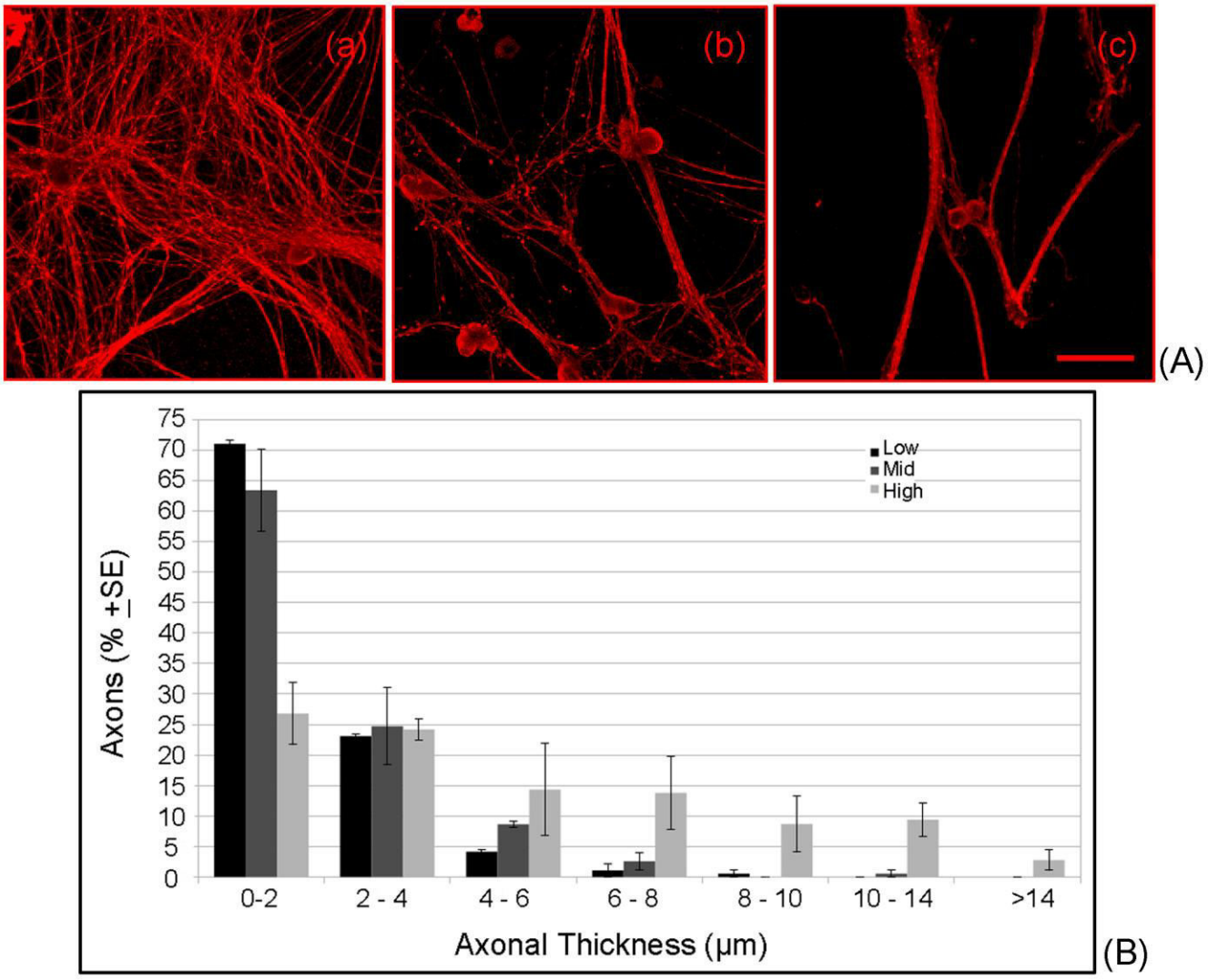

Fig.4.16: Quantitative evaluation of axonal fasciculation. Axonal thickness of NF positive axons grown on micropatterned Si substrates of different roughness is measured *via* the frequency distribution function. The number of axons with a thickness value within a specific range is expressed as percentage of cells (± standard error of the mean, SE). The results represent the means of three different experiments. Scale bar: 48 μm

4.4.3 Coculture of Dissociated DRGs and Schwann cells on microconical structured Si surfaces

As it was shown (Paragraph 4.4.2 and 4.4.3) when cultured alone, Schwann cells could grow on the micropatterned substrates without necessarily the need of protein coating and exhibited a roughness- dependent growth orientation. Sympathetic neurons could also grow on collagen coated micropatterned substrates, exhibiting a similar roughness-dependent growth orientation response. Since it is known that Schwann cells grow in proximity with axons [D. Pearse *et al*., 2004, N. Mahanthappa *et al*., 1996], affecting their outgrowth during development but also in response to injury, it was then

inquired to investigate such interrelation . In this context, in order to check whether oriented Schwann cells could drive the axonal outgrowth without the need for other biochemical cues [E. Anton *et al.*, 1994], coculture of dissociated SCGs and Schwann cells was performed.

SCGs were co-cultured with Schwann cells that were first seeded on the substrates as outlined above. Schwann cells and sympathetic neurons were identified by their S100 and Neurofilament (NF200) immunoreactivity, respectively. Schwann cells were grown on the medium roughness Si substrates, exhibiting parallel orientation. Sympathetic neurons grown on top of them followed Schwann cell orientation (Fig. 4.17).

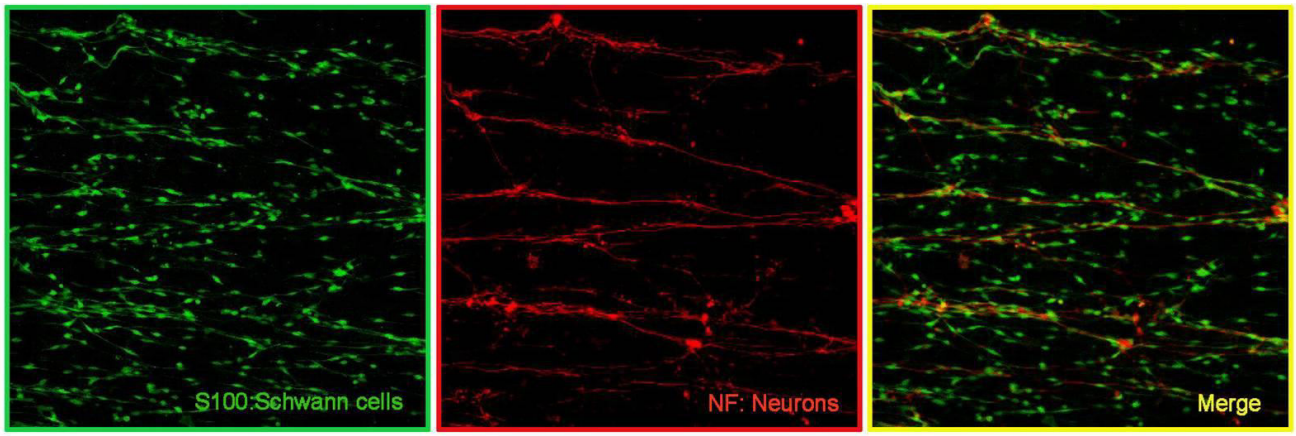

Fig.4.17: Effect of surface roughness on neuronal outgrowth. Confocal microscopy images of S100 positive Schwann cells and Neurofilament positive sympathetic neurons grown on medium roughness micropatterned Si substrates.

4.4.4 Effect of surface roughness on Schwann cell migration and neurite outgrowth from DRG explants

It was then inquired whether the observed roughness- dependent growth orientation could be reproduced in a naturally occurring coculture system, which included the organotypic culture of dorsal root ganglion (DRG) explants. Whole DRG explant culture is regarded as a well established model for evaluating cell migration and axonal outgrowth as it contains both cell populations that were examined in the present study. Schwann cell migration and axonal outgrowth was assessed by qualitative (via imunocytochemistry and scanning electron microscopy) and quantitative (image analysis of staining) morphological methods. It has to be mentioned that the micropatterned substrates had not been coated with any protein. In this way, the role of topography on cellular growth could be studied independently of any other exogenous biochemical cues.

Although the standard 2D culture surfaces and flat Si cannot support whole ganglion explant outgrowth without pre-coating, laser micropatterned silicon surfaces could support DRG growth, even without the need for collagen coating with an excellent (100%) reproducibility. DRG explants showed a nice outgrowth on all three types of substrates, however in a differential manner. While the outgrowth of DRG explants on the low roughness substrate appeared more circular in shape ("halo"effect), it was strikingly parallel oriented in the case of medium and high roughness substrates. In some cases, even the shape of the DRG explant was elongated as well, a behavior which has been described from other groups [J. Corey *et al*, 2007].

Both Schwann cell migration (stained for S100) and axonal outgrowth (stained for neurofilament200kD- NF) was very good on the micropatterned Si substrates. However, the orientation of both Schwann cell migration and axonal outgrowth varied among the different substrates (Fig.4.18). More specifically, the cells on the low roughness substrates migrated away from the DRG explants at all possible directions (Fig. 4.19a). In a similar way, the axons emanated from the DRG explants radially (Fig. 4.19b). However, on the medium (Fig. 4.20a) and high (Fig. 4.21a) roughness substrates, the Schwann cell migration exhibited a preferred parallel orientation towards a hypothetical horizontal axis. The outgrowing axons exhibited a similar response (Fig. 4.20b & 4.21b). The axons did not grow equally in all directions. Although at the beginning they extended from the explants radially, axonal outgrowth was then preferentially enhanced along a hypothetical elongation axis. In this respect, axons growing in all other directions got aligned with this specific preferred orientation.

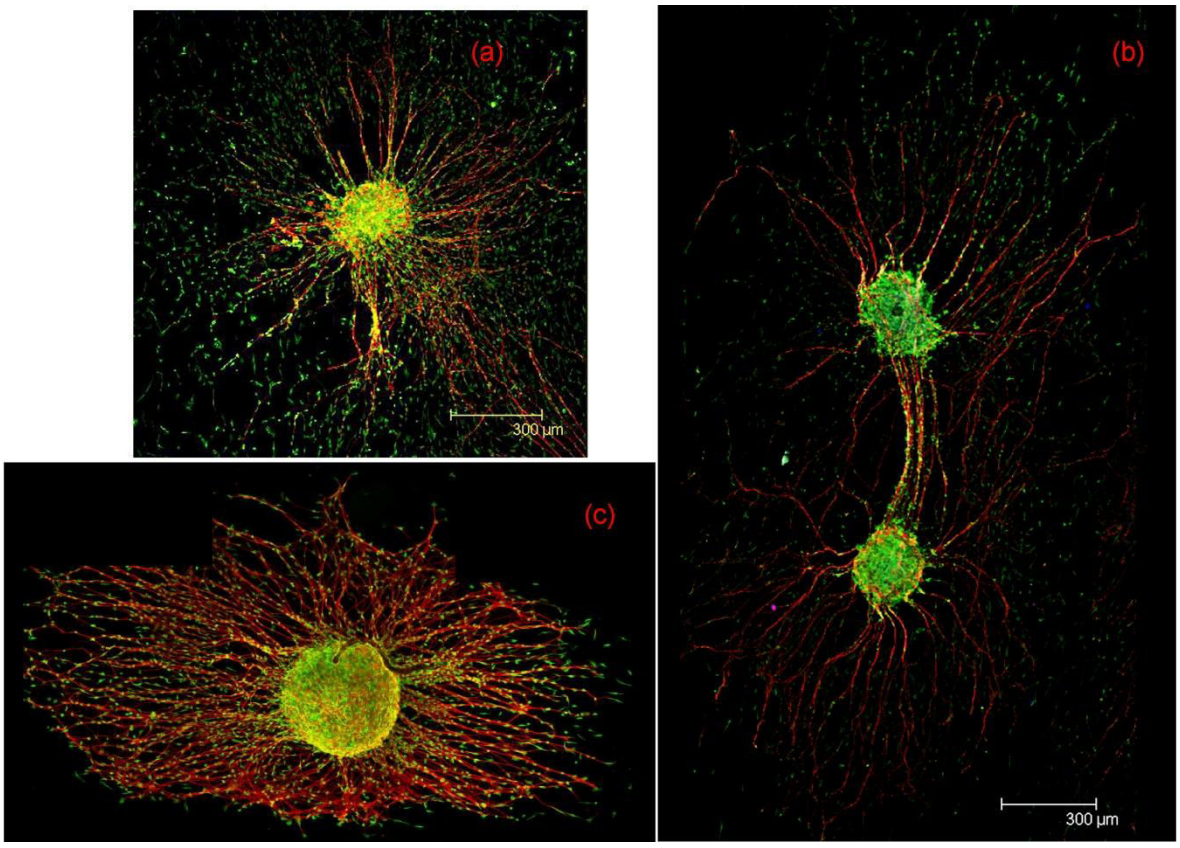

Fig. 4.18: Effect of surface roughness on Schwann cell migration and neuronal outgrowth. Confocal microscopy images of S100 positive Schwann cells (green) and Neurofilament (red) positive sympathetic neurons grown on low (a), medium (b) and high (c) roughness micropatterned Si substrates. Scale bar: 300 µm

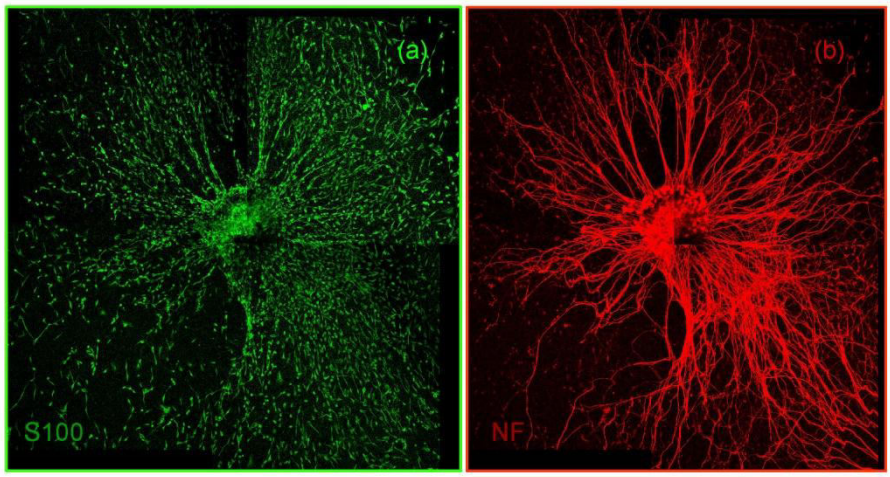

Fig. 4.19: Confocal microscopy images of S100 positive Schwann cells (a) and Neurofilament (NF) positive sympathetic neurons (b) grown on low roughness micropatterned Si substrates.

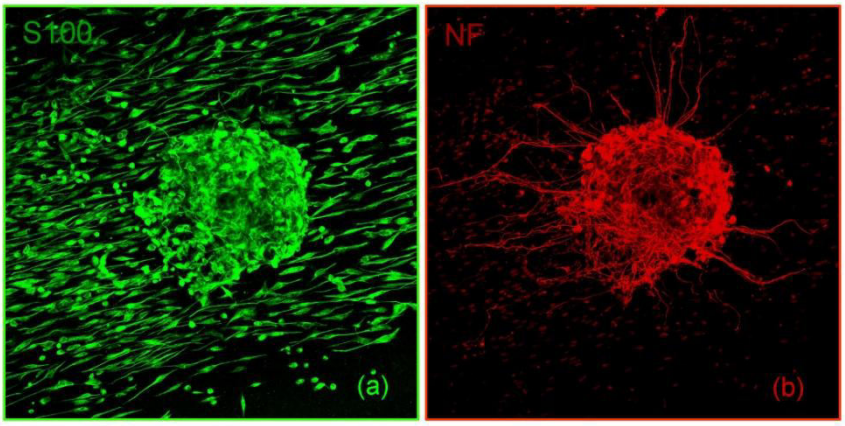

Fig. 4.20: Confocal microscopy images of S100 positive Schwann cells (a) and Neurofilament (NF) positive sympathetic neurons (b) grown on medium roughness micropatterned Si substrates.

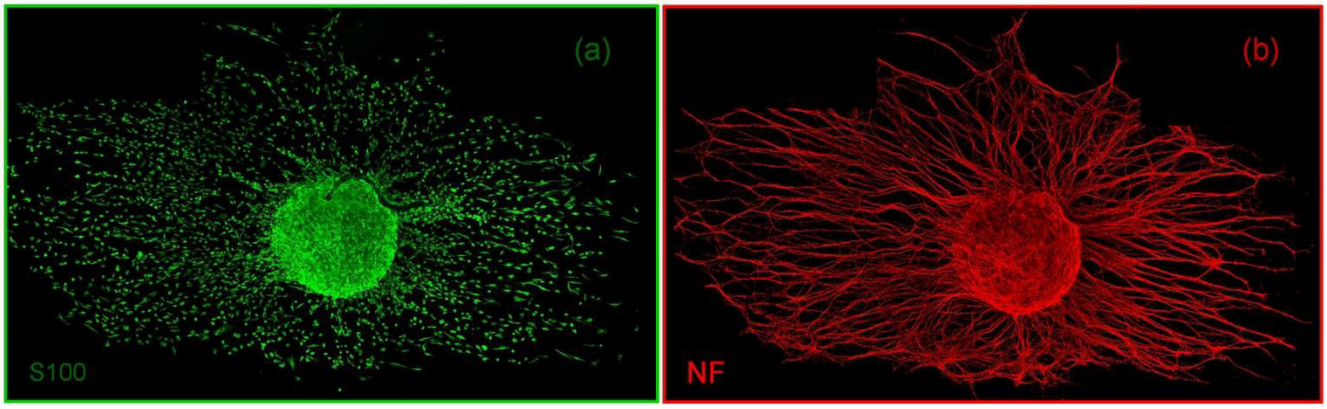

Fig.4.21: Confocal microscopy images of S100 positive Schwann cells (a) and Neurofilament positive sympathetic neurons (b) grown on high roughness micropatterned Si substrates.

4.4.5 Spatial relationship between neurites & non-neuronal cells from DRG explants on micropatterned Si substrates

The morphological analysis using scanning electron microscopy (SEM) revealed that migrating cells developed on top of the substrate's microcones. Moreover, the cells largely followed single microcone direction and migrated along the "corridor" created by the sequential lines of the microcones (Fig. 4.22 & 4.23). Already as the cells emanated from the explants, the migrating cells changed their orientation in a way following the direction of the underlying topography (Fig. 4.24a). On the contrary, when the cells reached a flat Si region at the borders of the micropatterned surface, they seem to lose this preferential orientation and continue to grow randomly to all directions (Fig. 4.15b). Since DRG explants were unable to grow on flat silicon substrates, such analysis could not be performed.

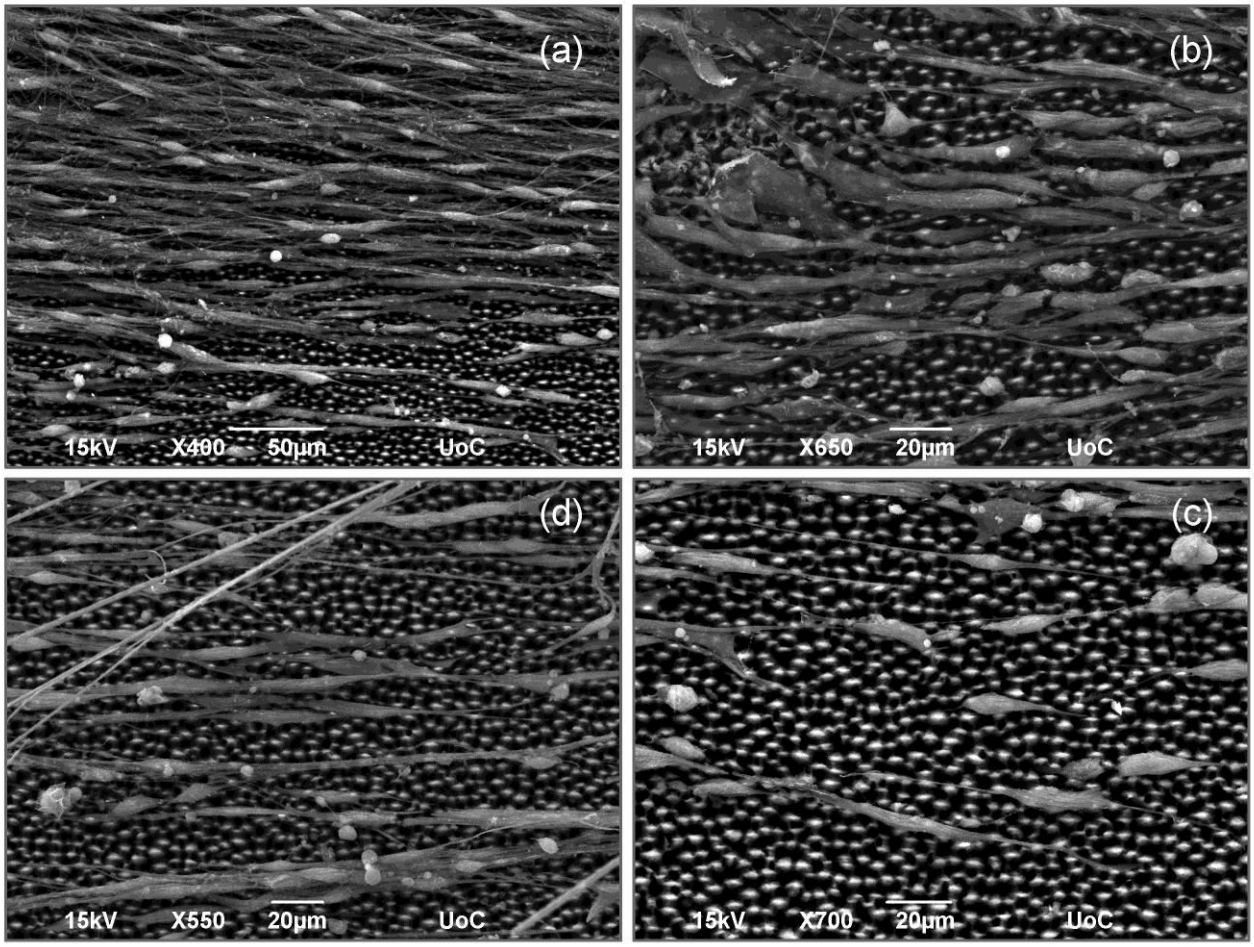

Fig. 4.22: Morphological investigation of migrating cells from DRG explants with scanning electron microscopy (SEM). DRG explants were cultured on micropatterned Si substrate of high roughness. Top views of different magnification (a-d) show cells of different morphologies grown on top of the spikes. Cells migrate preferentially along the hypothetical "corridor" created/ by the sequential lines of microcones.

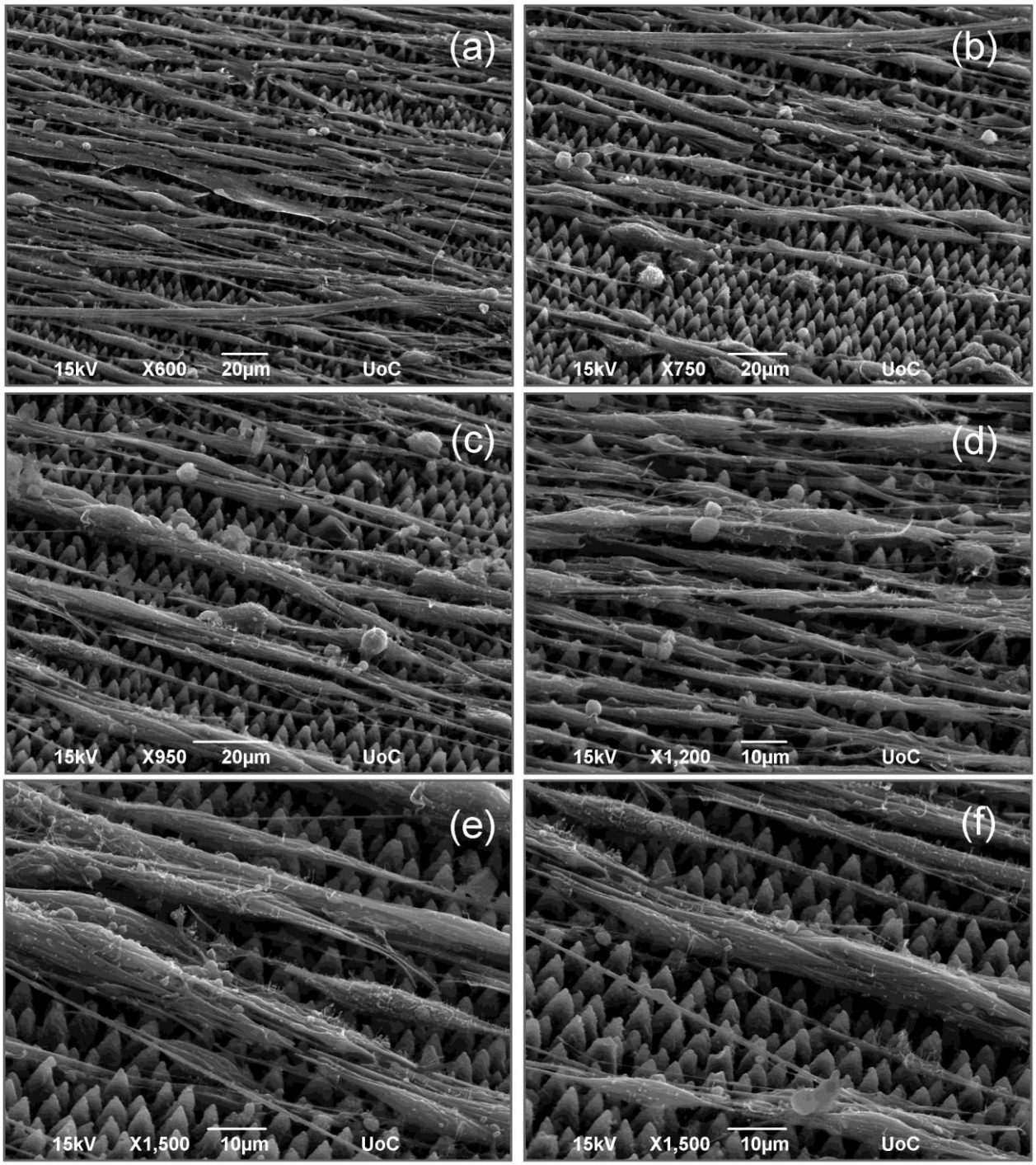

Fig.4.23: Morphological investigation of migrating cells from DRG explants with scanning electron microscopy (SEM). DRG explants were cultured on micropatterned Si substrate of high roughness. Tilted views (45^{o}) of different magnification (a-f) show cells of different morphologies grown on top of the spikes. Cells migrate preferentially along the hypothetical "corridor" created by the sequential lines of microcones.

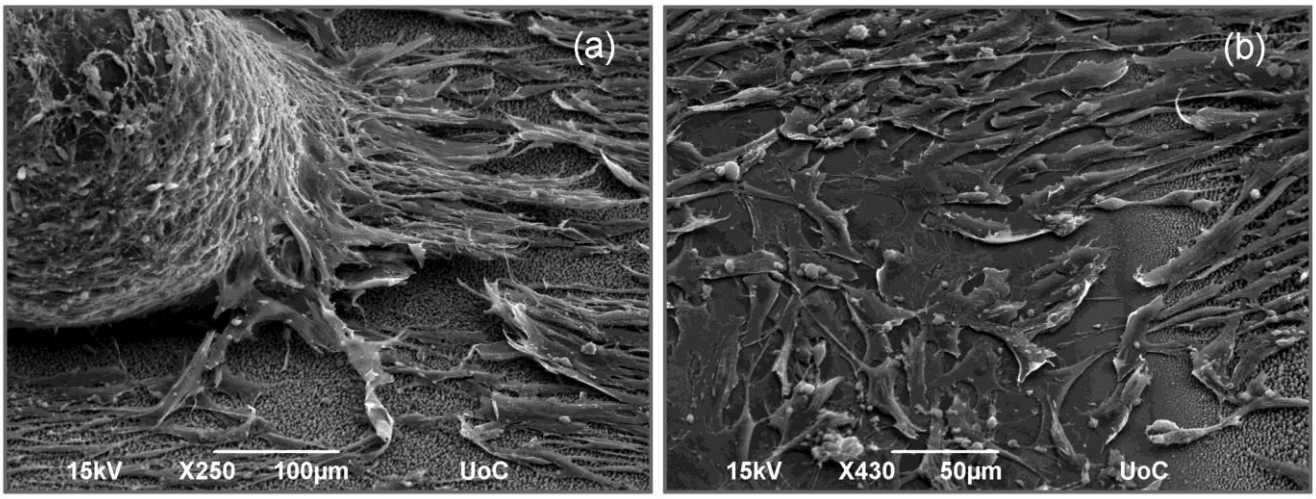

Fig. 4.24: Morphological investigation of migrating cells from DRG explants with scanning electron microscopy (SEM). Position close to the DRG explant, which is grown on a micropatterned Si substrate of high roughness, shows cells at the moment when they emanated from the DRG explant (a). A layer of cells that migrated from the explants developed along with the underlying anisotropic topography induced by the substrate. When the migrating cells reached the flat Si they lost the preferred orientation and were distributed randomly (b).

Electron microscopy analysis revealed the presence of two morphologically distinct types of migrating cells. The first (Fig. 4.25a) had features of typical fibroblasts, that is, diaphanous, amoeboid cell bodies and large, ellipsoid nuclei. The second included spindle-like cells. These were smaller (perikaryon 5-10 µm), darker and more elongated, often extending in tenuous spindle shapes with processes 100 µm or longer. The spindle-shaped migrating cells were single or assembled into cellular columns (Fig. 4.25b). Cells of both types proliferated and overwhelmed cultures in large numbers. Small, round elements (~5 µm diameter) were also visible.

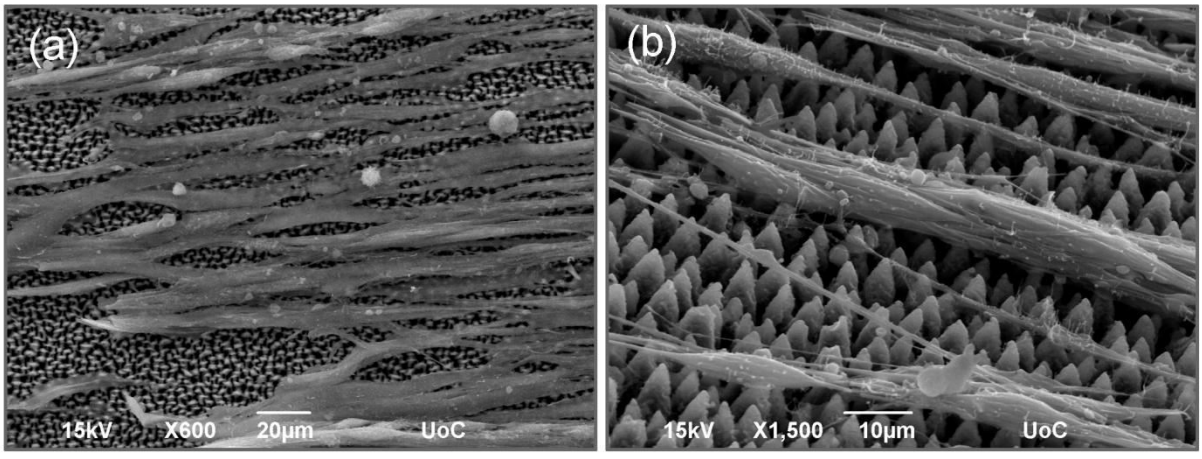

Fig.4.25: Different types of non-neuronal cells migrating from DRG explants on laser micropatterned Si substrate of medium roughness. Electron microscopy images of top view (a) and tilted view (45^{o}) (b).

Axonal outgrowth evolved in a distinct way. Neuronal axons had no direct contact with the substrate. The tips of the axons were attached to the migrating cells, and followed them as these were migrating away (Fig. 4.26). In this way, the axonal shaft remained hanged and had no contact with the surface level (“kite-surf” configuration or "guy rope" configuration). This distinct configuration was completely absent when the DRG explants were cultured on collagen coated standard tissue culture (TC) wells. In this case, the axonal outgrowth followed a more web-like morphology (Fig. 4.27). This distinct "guy rope" configuration of the DRG explant has been early described and correlated with the lack of appropriate underlying substrate coating [R. Bunge and M.Bunge, 1978]. Axonal outgrowth occurs by the progression of growth cones across the collagen surface. According to *P.Bunge & M. Bunge*, when the explant is bulbous rather than flattened, some axons must grow over the sides of the explant to reach the collagen surface before progressing into the outgrowth. Although the tips of these axons attach to the substrate, their shafts do not. This phenomenon may lead to the so called "guy rope" configuration, according to which the axons arisie well above the substrate surface and attach to the substrate, 0.2-1 mm away from the explant periphery [R. Bunge and M.Bunge, 1978].

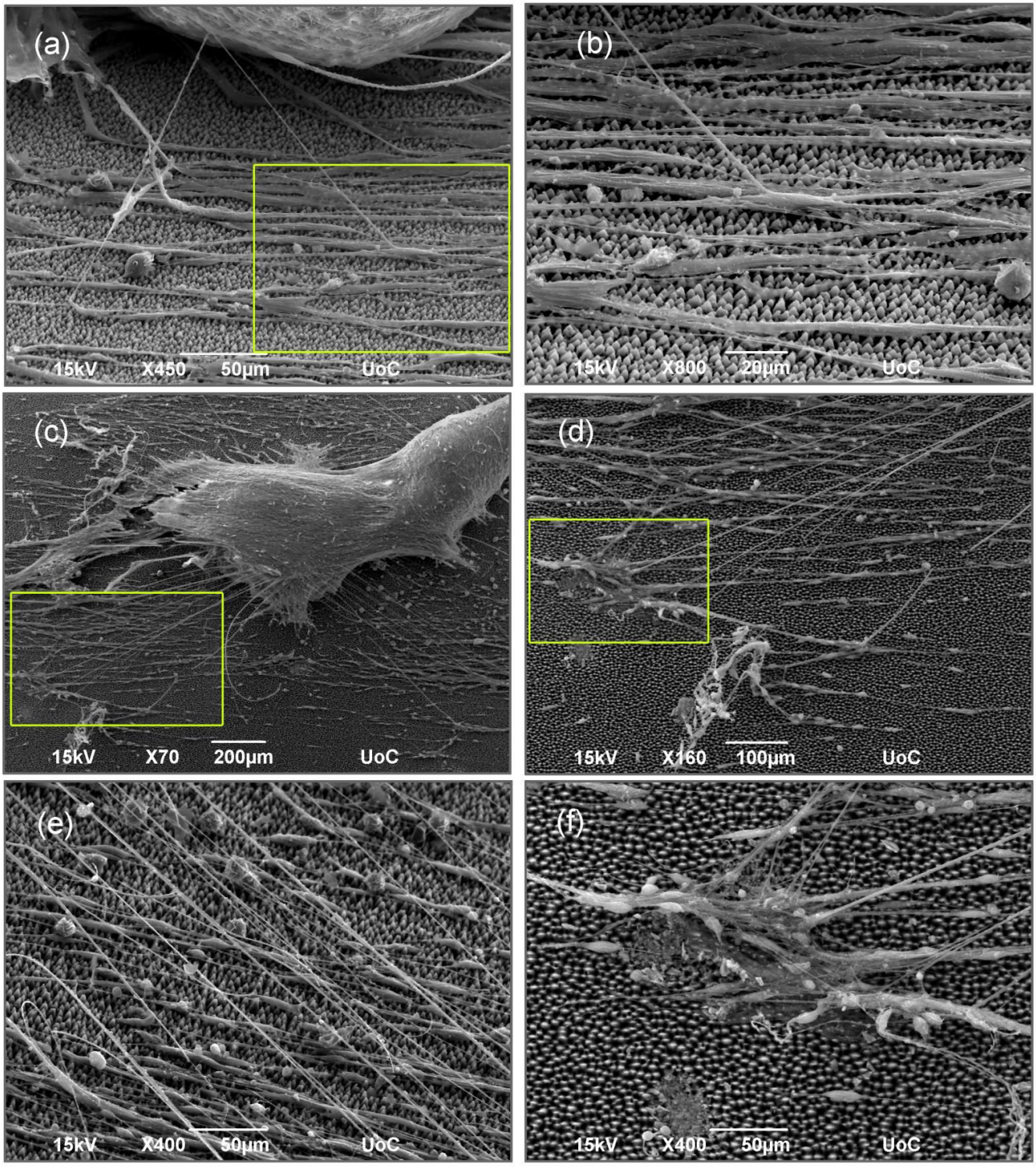

Fig.4.26: Morphological investigation of migrating cells and outgrowing axons from DRG explants using scanning electron microscopy (SEM). DRG explant was cultured on a micropatterned Si substrate of high roughness. Outgrowing axons were attached to and followed the migrating cells. A position close to the DRG explants shows axons emanating from the explants and following the migrating (a). b,d and f represent higher magnification views of the yellow-colored delineated regions of a, c and b, respectively.

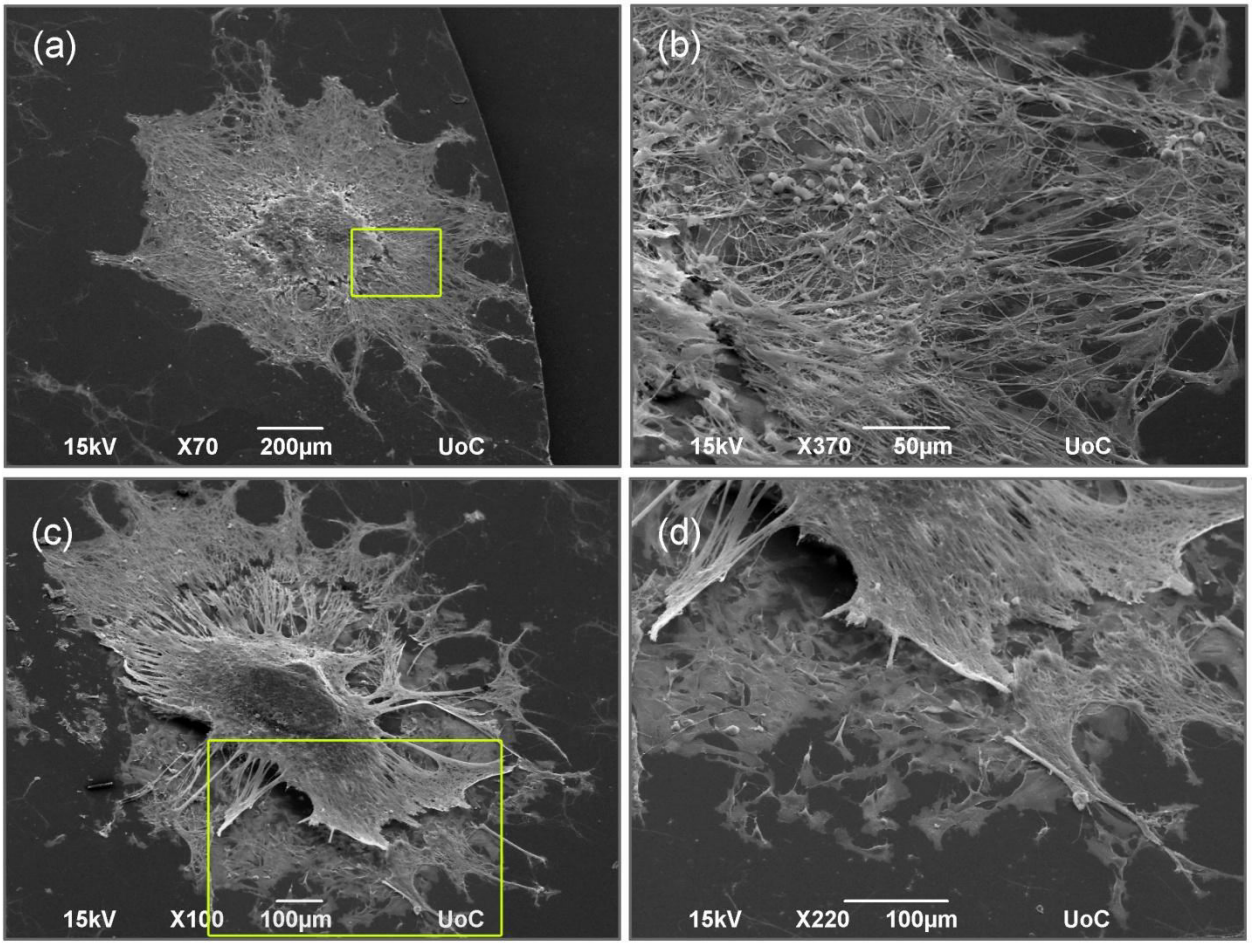

Fig. 4.27: Scanning electron microscopy images of DRG explant grown on collagen coated plastic coverslips: Top views (a & b) and tilted views (c and d). (b) and (d) represent higher magnification images of the yellow-colored delineated regions of (a) and (c), respectively.

In order to investigate the spatial relationship of the migrating cells and the outgrown axons on the micropatterned Si substrates, a series of optical sections using confocal microscopy were obtained. The different optical sections were taken from top (upper level of the DRG explants) to bottom (lower level of the Si substrate) and the various cell types in each section were identified (Fig. 4.28). Following this type of analysis, imaging from top to bottom only sections of NF positive axonal shafts could be seen (Fig. 4.28a-d). On the contrary, lower level sections of the micropatterned surface revealed a monolayer of parallel aligned S100 positive cells (Schwann cells) (Fig.4.28Be-f) which was free of axons (Fig.4.28Ae-f). Therefore, it seemed that the migrating glial cells created a "carpet" onto which the neurites could grow (Fig.4.29). This distribution was also confirmed by digital xz optical cross-section analysis (Fig.4.29a inset).

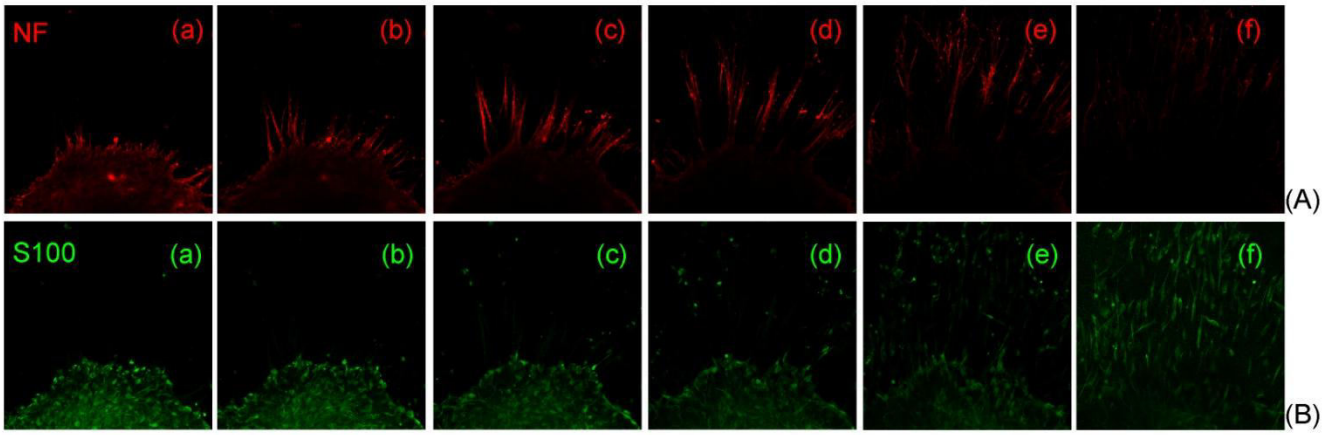

Fig.4.28: Image sequence of confocal microscope optical sections of Neurofilament (NF) positive sympathetic neurons (A) and S100 positive Schwann cells (B) grown on medium roughness micropatterned Si substrates. The different optical sections beginning from top (upper level of the DRG explants) to bottom (lower level of the Si substrate) are denoted as a to f, respectively.

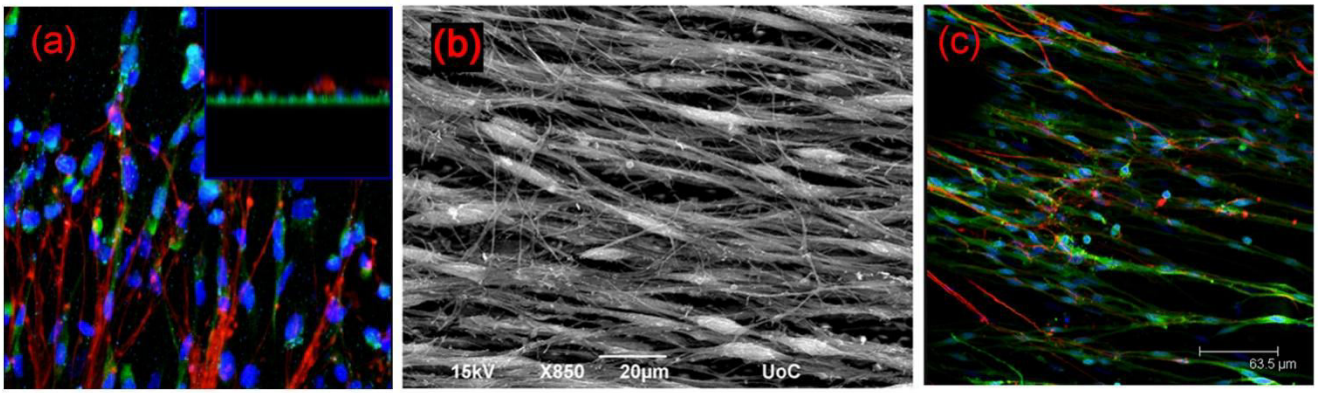

Fig.4.29: Spatial relationships between neurites and Schwann cells on medium roughness micropatterned Si substrates. Confocal microscopy image of Neurofilament positive sympathetic neurons (red), S100 positive Schwann cells (green) and TOPRO stained cell nuclei (blue) (a and c). The inset in (a) shows a digital xz optical section. Electron microscopy image illustrating the outgrowing neuritis on top of Schwann cells (b).

4.4.6 Organization of fibronectin and spatial relationships between axons/neurites & fibronectin on micropatterned Si substrates

Schwann cells modify their environment by synthesizing and secreting extracellular matrix (ECM) components, such as vitronectin, laminin and fibronectin. These components along with other molecular components are organized into basal laminae, which surround the mature Schwann cell-axon units. This rich and supportive environment provided by the Schwann cells is important for neurite outgrowth [R. Bunge and C. Fernandez-Valle, 1995]. Fibronectin laid down by glial cells was observed

by staining with fibronectin antibody, while the axons were stained with NF (Fig.4.30) In a DRG explant growing on a micropatterned Si substrate of medium roughness, the neuritis formed a very dense network, while a striking trend for anisotropic neurite outgrowth was observed (Fig.4.30a). Focusing on the fibronectin staining (Fig.4.30b), two types of fibronectin expression could be obtained: The first was associated with the migrating cells which showed intracellular or surface staining (Fig. 4.30c arrows). The second included extracellular fibrils of fibronectin (Fig.4.30c arrowheads), which might have been secreted by the non neuronal migrating cells (fibroblasts and Schwann cells). In order to provide an insight into the two different types of fibronectin expression, a series of optical sections using confocal microscopy were obtained. The different optical sections were taken from top (upper level of the DRG explants) to bottom (lower level of the Si substrate) and the expression of fibronectin at each section was evaluated (Fig.4.31).

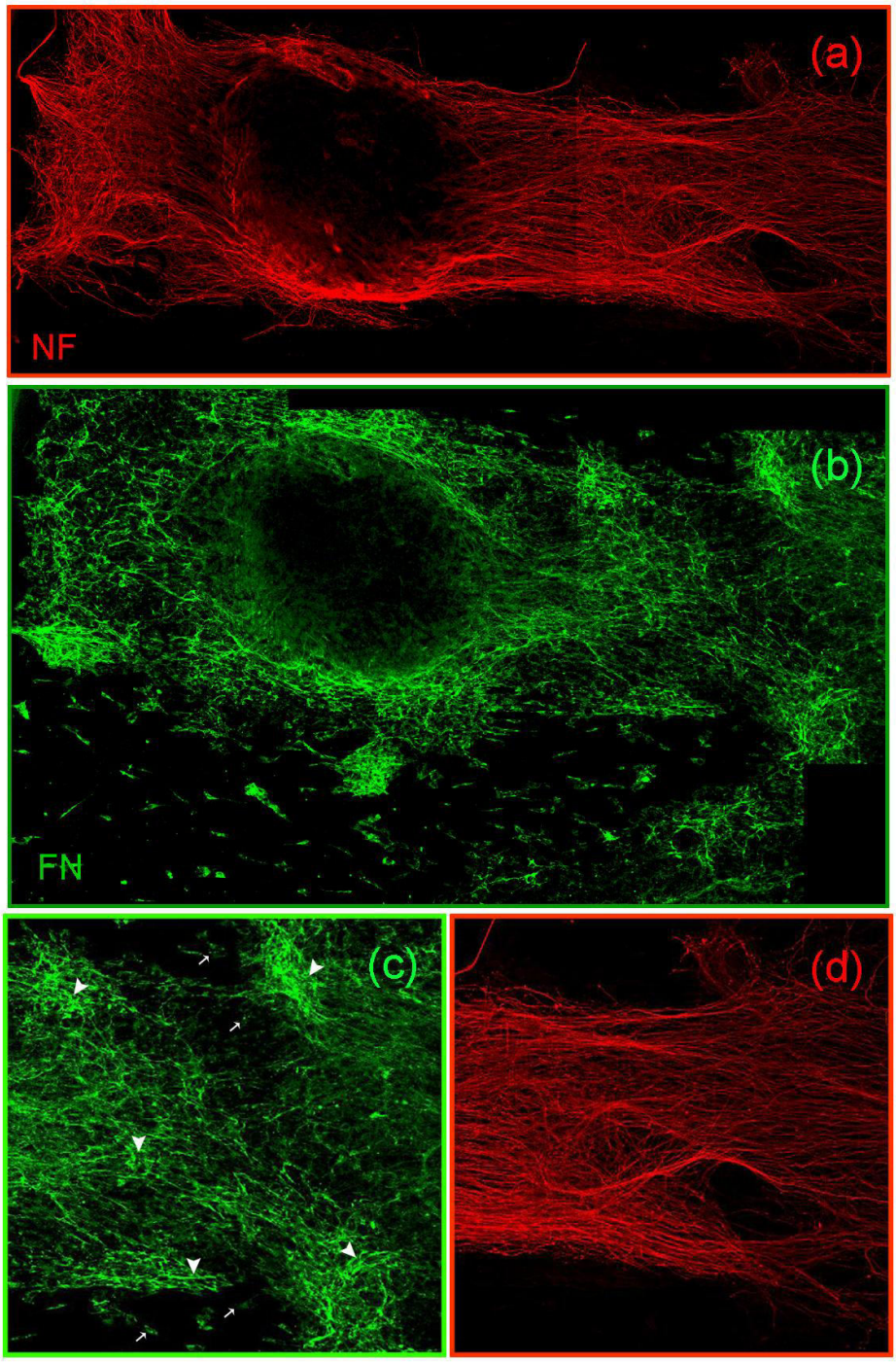

Fig.4.30: Representative montage of confocal microscopy images of Neurofilament (NF) positive sympathetic neurons (a) and Fibronectin (b) on medium roughness micropatterned Si substrates. A region from (b) illustrating the fibronectin expression (c). Arrows and arrowheads indicate the intracellular and surface expressed fibronectin, respectively. The respective region from (a) showing the NF positive sympathetic neurons (d).

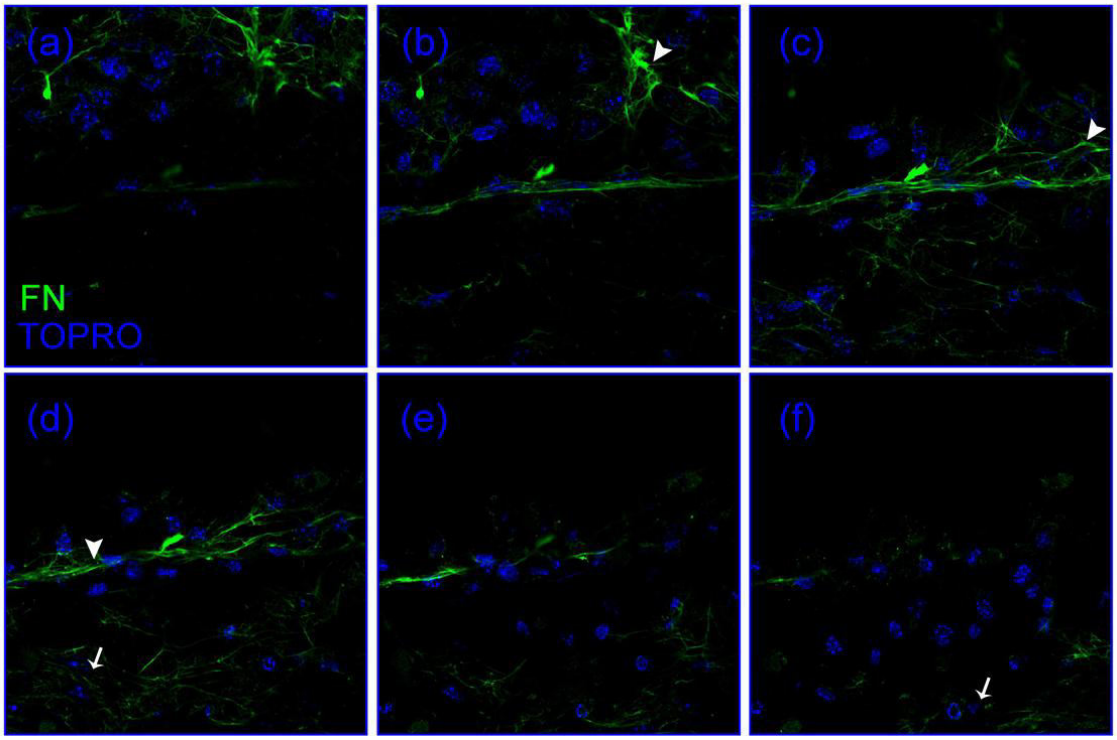

Fig.4.31: Image sequence of confocal microscope optical sections of Fibronectin (Fn) positive (green) and TOPRO positive (blue) cell nuclei on medium roughness micropatterned Si substrates. The different optical sections beginning from top (upper level of the DRG explants) to bottom (lower level of the Si substrate) are denoted as a to f, respectively. Arrows and arrowheads indicate the intracellular and surface expressed fibronectin, respectively.

In order to study the interrelationship of outgrown neurites and secreted fibronectin, confocal microscopy images of higher magnification were taken. The outgrowth of fibronectin, which was secreted by the non neuronal cells (Schwann and/or fibroblasts) was organized into many parallell fibers (Fig. 4.32a) in the region around the neighboring cells and seemed to follow the orientation of the outgrown neurites (Fig. 4.32b). Moreover, a series of optical sections using confocal microscopy analysis were obtained. The different optical sections were taken from top (upper level of the DRG explants) to bottom (lower level of the Si substrate) and the signal from Fn and neurofilament at each section was evaluated (Fig. 4.33). According to this analysis, going from top to bottom, NF positive axons and extracellular fibronectin fibrils exhibited the same orientation (Fig. 4.33a-d). At the lower levels of the sections (level of the micropatterned surface) only fibronectin fibrils were visible (Fig.4.33e-f). Therefore, axons were shown to grow within an interconnected network of Fn fibrils.

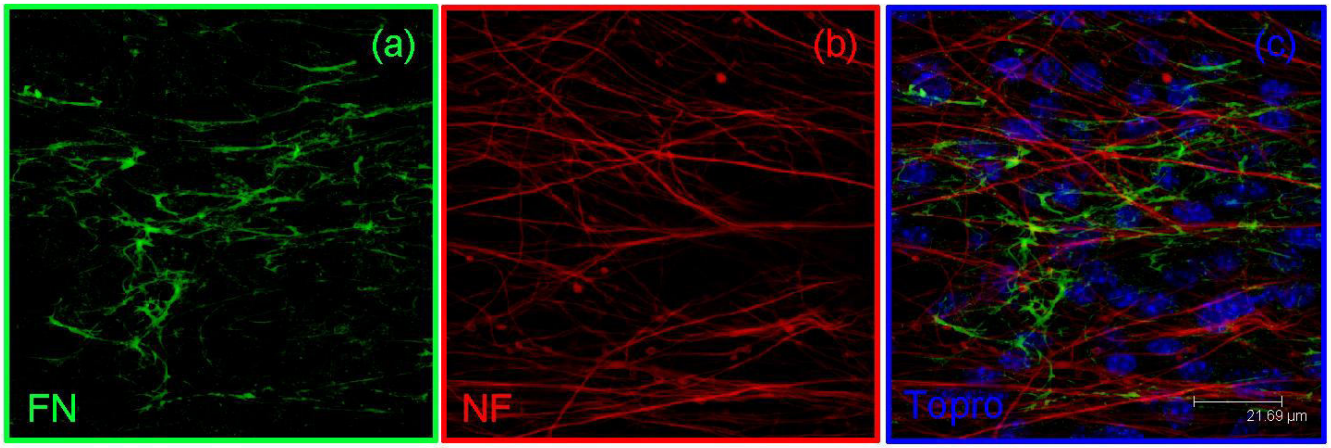

Fig.4.32: Fibronectin organization and axonal outgrowth: Confocal microscopy images of Fibronectin (FN) (a) and Neurofilament (NF) positive sympathetic neurons (b). Co-staining of Fn, NF and TOPRO (c). Scale bar: 21.69 µm.

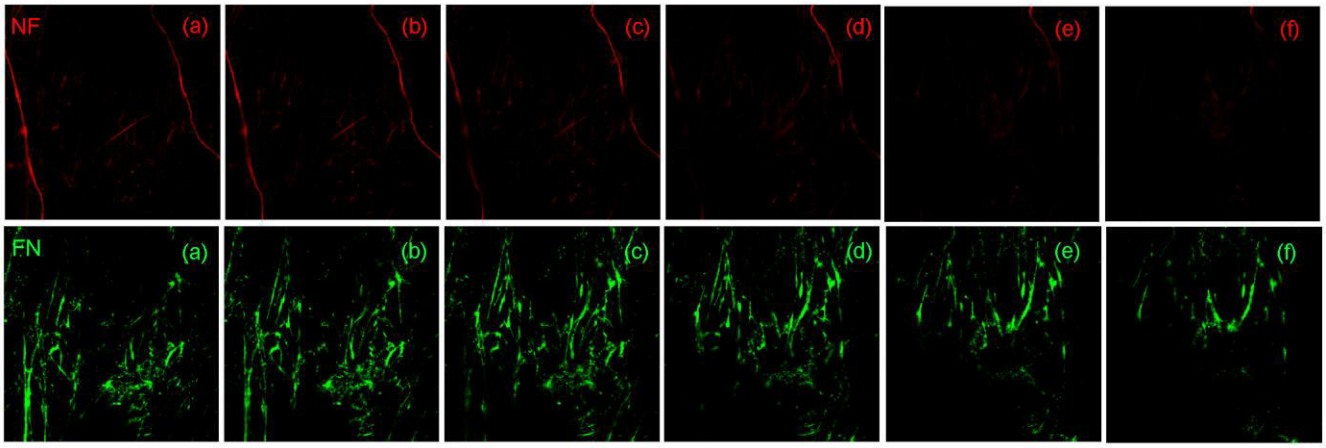

Fig.4.33: Image sequence of confocal microscope optical sections of Neurofilament (NF) positive sympathetic neurons and Fn grown on medium roughness micropatterned Si substrates. The different optical sections beginning from top (upper level of the DRG explants) to down (lower level of the Si substrate) are denoted as a to f, respectively.

5. Discussion

5.1 Micropatterned Si surfaces fabricated via ultrashort-pulsed laser processing as culture substrates for the study of cellular growth

The control of neuronal cell outgrowth is of critical importance in a wide spectrum of neuroscience applications including tissue engineering scaffolds and neuron electrophysiology studies. Although information regarding neuron cell outgrowth on more complex topographies remains limited, evidence of phenotype alteration in stem cells [L. McNamara *et al.* 2010; S. Ortinau *et al.* 2010] or neuronal cells [M. Schindler *et al.* 2006; G. Christopherson *et al.* 2009] upon culture on 3D scaffolds as compared to traditional flat substrates lacking structural cues, emphasize the necessity to shift from 2D to 3D or multi-scale culture models. Many geometrical surface models made of different materials have been developed as model scaffolds for the systematic exploration of the role of 3D surface topography on neuronal and neuroglial cell outgrowth and neural network formation. Such models can be useful to address basic neurobiological questions with the ultimate goal of providing mechanistic insight to guide the development of clinically relevant strategies for nerve repair. The majority of the geometries being used could be listed in two categories. The first includes the well-studied anisotropic continuous geometries, (i.e. alternating grooves and ridges, parallel fibers, etc.) and the second includes isotropic discontinuous geometries, i.e. pillars, posts, etc. (Table 1.8 & 1.9).

The aim of the present study was to investigate the cellular growth on laser micropatterned Si substrates (comprising arrays of microcones -MCs- with different geometrical characteristics). The following cell culture models have been used and the respective cell functions have been investigated. First, the PC12 cell model has been used in order to study the growth and differentiation pattern after treatment with NGF (neuritogenesis) on the micropatterned Si substrates (Paragraph 5.2). Furthermore, culture of dissociated primary cells of the PNS has been used. To this respect, the **topographic guidance of neural outgrowth and network formation of** dissociated SCG sympathetic neurons (Paragraph 5.3) and **the effect of (surface) topography on Schwann cell morphology** (Paragraph 5.4) have been investigated. Moreover, the organotypic dorsal root ganglion (DRG) explant model has been used and the **topography-dependent neurite outgrowth and Schwann cell migration from DRG explant has been studied** (Paragraph 5.5). Finally, coculture of dissociated sympathetic neurons and Schwann cells has been performed (Paragraph 5.7).

Micropatterning has been realized by **femtosecond pulsed laser direct writing of crystalline silicon (Si)** wafers. Upon increasing laser fluence, three types of micropatterned Si surfaces, exhibiting different microconical morphology of different geometrical characteristics (denoted as low, medium and high roughness substrates, respectively), have been fabricated, characterized and further used for the *in vitro* assays with cells (Fig. 4.1B). Analysis showed that **as substrate's roughness increased, microcone's density decreased and microcone's height increased** (Table 4.1). Interestingly, **as roughness increased (i.e. from low to high), an anisotropy in geometry was more pronounced** (Fig. 4.2). More specifically, low roughness surfaces comprised circular microcones without a preferred orientation. On the contrary, medium and high roughness surfaces consisted of elliptical microcones which presented a striking parallell aligned orientation. Accordingly, the base of each microcone was elliptical, with a long and a short axis; the long axis was perpendicular to the polarization of the laser light. Therefore, the suggested topography could be described as **semiperiodical discontinuous (arrays of oriented microcones) comprising an anisotropic feature (elliptical cross-section)**. This distinct morphology of the microcones attained can be attributed to the higher absorption of p-polarized light over s-polarized light [J. Carrey, 2004].

Moreover, the enhancement in MC roughness was accompanied by a decrease in surface hydrophilicity,that has been previously reported [V. Zorba *et al.,* 2006]. More specifically, when shifting from flat to high roughness, the Si surfaces became more hydrophobic. For culture experiments with cells, micropatterned Si have been directly sterilized using either an autoclave or a thermal treatment at 1000^{o}C. It was shown (Paragraph 4.2.1) that with both procedures a SiO_2 layer was formed on the Si surface, either as thin native or thick oxide layer in the first and second cases, respectively. Both procedures altered the surface energy and rendered the initially hydrophobic substrates to superhydrophilic, regardless of the surface roughness. A series of substrates had been coated with collagen solution. After coating, all micropatterned surfaces were superhydrophilic while their roughness was preserved. Therefore, all three micropatterned and flat Si substrates switched to superhydrophilic before their use as cell culture substrates (Paragraph 4.2). This means that **the biological responses** observed in the context of the *in vitro* experiments with cells **could be attributed to** one sole surface parameter, **the surface roughness**.

5.2 Topography of microconical silicon structures influence NGF-induced PC12 cell differentiation

PC12 cells were shown to largely prefer MCs surfaces for growth, as compared to flat substrates. In the absence of NGF stimulation, PC12 cells cultured on MCs maintained their round shape and small nucleus size, while clustering in a 3D manner, characteristics similar to those well documented by *Greene & Tischler* [L. Greene and A. Tischler, 1976]. In this case, it was shown that MC Si substrates could support PC12 cell adherence without any coating, while cell behavior could change upon altering the MCs surface energy using a chemical coating. Although cell growth was inhibited on oxide coated MCs, it became slightly improved on collagen-coated structures. The above results demonstrated the useful utilization of Si MCs in supporting nerve cell adherence and neurite growth.

Upon treatment with NGF, cells flattened and extended processes with tubulin-rich terminals, surrounded by actin-expressing lamellipodia and filopodia resembling the already described growth cones of primary neurons [C. Lin and P. Forscher, 1993; A. Mingorance-Le Meur *et al.,* 2009]. Although differentiated cells grew on top of the surfaces, it seemed as they "sensed" the surface roughness via the tip of their neurite extensions (Fig. 4.9). As previously proposed [K.Yamada *et al.,* 1970], the actin-based motile part at the growth cone of these filopodia could be responsible for probing. Although PC12 cells responded to the NGF treatment on the patterned Si surfaces, they displayed a differential behavior depending on the MCs topography. Since all three different rough surfaces were structured within a single substrate and placed in a single well, ensuring that all different rough surfaces were exposed to exactly the same culture conditions, it can be concluded that **upon NGF treatment, cell differentiation was promoted on low and intermediate roughness textures, whereas it was strongly inhibited on the highly rough ones.** Since this differential response was observed for different MCs' surface chemistries, the effect should be associated with MCs topography. This observation implied that the topographical cue imposed by specific MCs topology, restricted neuronal precursors to exit the cell cycle and differentiate.

Further insight into the topography-mediated inhibition of cell differentiation could be provided by focusing on the geometrical features of the MCs, presented in Table 4.1, in comparison with the cell size and shape observed by SEM imaging (Fig. 4.6A). In particular, in case of the high roughness surfaces the distance among MCs, *c*, is higher (4.48±0.96 μm)

compared to the low and mid roughness ones (1.73±0.28 μm and 2.06±0.53 μm, respectively). Accordingly, for low and mid roughness surfaces, undifferentiated cell bodies remained on top of the microstructures (Fig. 4.6A-a and -b), while on the high roughness ones cells could be "trapped" among MCs (Fig. 4.6A-c), because the size of undifferentiated cells is comparable to the interspikes' space. It thus appeared that among the different morphological parameters of MCs, the inter-spike distance could be considered as a critical characteristic affecting cell differentiation. On the contrary, cell differentiation appeared to be insensitive to the aspect ratio, *A*, since although both mid and high roughness surfaces exhibited similar *A*, they showed much different behavior as to cell differentiation. Based on these results, a geometrical model could be proposed, suggesting that there is a critical interspike distance over which cells are not allowed to elongate, develop extensions and finally differentiate. This distance should depend on the cell size. Indeed, in the case of low and mid roughness surfaces, PC12 cell bodies would lie on top of many MCs, while on highest roughness surfaces, exhibiting lower MC density and larger interspike space, the cells would merely stay onto a few or even trapped within spikes (Fig. 4.6A). In addition, the characteristics of cell differentiation on periodical arrays of Si MCs may exemplify an ergonomic way of neuritic sprouting, where neuritic extension would be dictated by the shortest interspike distance. Accordingly, for small interspike distances (spacing below ~2μm), the cells would spread readily, since they could reach MCs for establishing the next focal adhesion contacts in all directions and consequently the cells would acquire a flattened phenotype. Upon increasing MCs spacing, the probability of reaching the next MC/spike would decrease.

Another important observation that complies with previous reports [A. Ranella *et al.,* 2010] is that in the low and mid roughness surfaces, many filopodia sprouted from cellular bodies, whereas this was not the case for cells growing on the highest roughness surfaces. It can be suggested that the absence of such filopodia sproutings from the cells could inhibit the differentiation process. According to *L. Luckenbill Edds* [L. Luckenbill - Edds *et al.,* 1979], both control and NGF-treated PC12 cells shared the same sprouts, named as extensions, and the same machinery of organelles. However, after NGF treatment, these extensions stabilized into processes, filled with microtubules and elongated, resembling the morphology of growth cones in primary neurons. Therefore, it could be argued that for cells cultured on high roughness surfaces, the absence of the very first extensions disabled NGF from exerting its effect towards

cell differentiation.

A number of studies envisage correlating specific geometrical characteristics of the topography with the induced cell morphological changes as well as the effect of surface topography and neurotropic signals (such as NGF), on PC12 cell differentiation. Most of the proposed models imply continuous anisotropic topographical cues, in the form of alternating grooves and ridges [J. Foley *et al,.* 2005; M. Mahoney *et al.,* 2005; M. Cecchini *et al.,* 2007], or electrospun fibers [J. Lee *et al.,* 2009; X. Liu *et al.,* 2010]. According to these studies, the morphology of the differentiated cells depended on the dimensions of the features (width, height and interfeature distance). As an example, it can be stated that morphology could switch from bipolar to multipolar upon shifting from submicron- to- micron-width ridges [A. Ferrari *et al.,* 2011; L. Yao *et al.,* 2009]. An increasing number of studies highlight the sensitivity of cell morphology to vertically oriented structures at microscale [M. Bucaro *et al.,* 2012; W. Su *et al.,* 2013] and more recently to submicron and nanoscale [F. Haq *et al.,* 2007]. In these cases, a differential response could be obtained when shifting from micro- to submicron scale features. For example, arrays of pillars in the range of microscale patterned on Si wafer could support PC12 cell differentiation towards a highly branched neurite phenotype in the presence [Su *et al.,* 2013] or the absence of neurotrophic factors [M. Bucaro *et al.,* 2012]. On the contrary, gold nanopillars limited neurite outgrowth of PC12 cells compared to smooth substrates [F. Haq *et al.,* 2007]. To the best of our knowledge, the effect of microconical topography on the differentiation fate of PC12 cells into a neuronal phenotype has not been exploited. The results presented here suggest that **a specific type of discontinuous anisotropic topographical cue (microconical structures) could influence the differentiation fate of PC12 cells in the presence of optimal neurotropic signals.**

5.3 Topographic guidance of neural outgrowth and network formation

Topographic guidance of neurite outgrowth and axonal guidance has been investigated *in vitro* by a number of researchers using different culture substrates containing micropatterned features on the submicron-to micron scale. These studies have used either embryonic primary nerve cells, like hippocampal or spinal cord neurons or cell lines, like PC12 cells, as a model for the study of neurite differentiation mechanisms. Two types of geometries have mainly been used. The first consisted of an anisotropic continuous geometry of alternating microgrooved substrates,

which were made from different materials including polymers, such as PS [M. Cecchini *et al*., 2008], PLGA [Yao et al., 2009], PDMS [N. Li and A. Folch, 2005; J. Goldner *et al.*, 2006; N. Gomez *et al*., 2007] and hard materials, such as quartz [I. Nagata *et al*., 1993; A. Rajnicek *et al*., 1997;], Si [F. Johansson *et al*., 2006]. According to these studies, groove depth and width seemed to be the critical parameters for axonal guidance and oriented neurite growth. The majority of studies have used microgrooves with a depth size ranging from 0.2 to 69 μm. It was shown that as depth increased, the percentage of cells growing parallel to the microchannels increased [N. Gomez *et al.,* 2007]. Remarkably, when the groove depth was very shallow (14 nm), hippocampal neurons lost their parallel orientation tendency and grew perpendicular to the grooves [A. Rajnicek *et al*., 1997]. This study emphasized also the effect of cell origin (i.e. developmental age and species) on the morphogenetic events of contact guidance. More specifically, whereas Xenopus spinal cord neurites grew parallel to grooves independent of feature dimensions, rat hippocampal neurites regulated their direction of neurite growth depending on groove dimensions and developmental age.

In the studies where groove width was quite large (50-350 μm), an interesting effect of groove depth was reported: axons turned at the edges of deep grooves (22-69 μm) but not at the edges of shallow grooves (2.5-11 μm) on PDL coated PDMS micropatterned substrates. More specifically, in response to steps of depth of h =22–69 μm, the vast majority of axons appeared to be guided by surface topography by turning and either remaining inside the grooves or staying on the top surface (the ‘‘plateaus’’). Neurons on shallow grooves disregarded the topographical steps and could extend axons freely into and out of the grooves [N. Li and A. Folch, 2005]. However, this “turning response” was lost when substrate-attached neurons were grown on Matrigel-covered substrates containing topographical steps (deep grooves). Upon arrival at the edge, almost all of on-plateau axons preferred to extend into matrigel rather than turning along the PDL-coated groove edge. The “straightness” of the 3-D growth was similar to that of growth on PDMS plateaus: some axons crossed the gel and landed onto the opposing plateau while other axons grew into and gradually changed height in Matrigel. This study emphasizes the complexity of the contact guidance phenomenon, when cells are challenged with competing growth options, induced by biochemical and topographical cues.

Groove width is also critical. The majority of the studies have used microgrooved substrates with a (groove) width ranging from 0.1 to 350 μm. In the case of subcellular

(nanometer and single-micron) groove width, orientated growth was observed on all types of patterns, although the 100 nm wide grooves seemed to be somewhat less efficient, as compared to the patterns with larger widths [M. Cecchini *et al*., 2008; F. Johansson *et al*., 2006]. In the cases of cellular (tens of microns) to supracellular (up to hundreds of microns) scale, as the width decreased, the growth orientation of the neurites was promoted in a direction parallel to channel walls and the complexity of neuronal architecture was reduced [M. Mahoney *et al*., 2005]. However, it has to be mentioned that this response was also dependent on the cell size. Although PC12 cells were too large to sit inside the grooves of 5 and 10 μm features (2-3 μm deep), their neuritis showed a preference for growth in the microgrooves rather than on the spaces [L. Yao *et al*., 2009].

Though the vast majority of studies using grooved substrates report parallel alignment of neuronal cell bodies, neurites, in addition to other cell types, other types of guidance have been reported as well [D. Hoffman-Kim *et al*., 2010]. In particular, it has been demonstrated that submicron and micron grooves can elicit perpendicular contact guidance in CNS neuroblasts [I. Nagata *et al*., 1993] and rat hippocampal cells [A. Rajnicek *et al*., 1997; N. Gomez *et al*., 2007], in a manner dependent on surface feature sizes. Neurites undergoing this form of contact guidance extended at an angle perpendicular to the features, crossing over adjacent grooves and ridges rather than extending parallel to a single feature. When a cellular extension reaches a linear topographical discontinuity, it can either cross it or follow it. It appears that the frequency of the perpendicular orientation depended on the origin of neurons and also on the feature sizes of the microstructures. *Nagata et al*. showed that various types of CNS neuroblasts (dissociated from the cerebral cortex, olfactory bulb, septum, striatum, hypothalamus, tectum, hippocampus and brain stem), but not PNS neurons, oriented their processes and migrated both perpendicular and parallel to the axis of the microstructure. Perpendicular orientation was frequently observed when the microstructured grooves had depths between 0.3 μm and 0.8 μm and a width of 1 μm, which roughly mimics a tightly aligned neurite bundle [I. Nagata *et al*., 1993].

In addition to perpendicular contact guidance, a number of neuronal and glial cell types including DRG neurons, B104 neuroblastoma cells, hippocampal neurons, and Schwann cells, have been shown to span grooves of a dimension larger than the cell body, from 30 to 200 μm, anchored to the plateaus only by tension bearing cellular extensions, with no underlying support in a climbing phenomenon termed “cellular bridging” [J. Goldner *et al.,* 2006].

The second type of geometry used as a model to study the topographic guidance of Schwann cells is anisotropic continuous geometry of parallel oriented electrospun fibers made of different synthetic polymers, such as PLLA [F. Yang *et al*., 2005; J. Corey *et al*., 2007; M. Leach *et al*., 2011] or blend of synthetic and natural polymers, such as collagen/PCL [E. Schnell *et al*. 2007]. These studies investigate mainly the effect of parallel oriented submicron-to micron electorspun fibers on neurite elongation and outgrowth (i.e.length, etc.) of single identified neuron. The size of electrospun fibers can influence alignment, growth potential, and differentiation [D. Hoffman-Kim *et al*., 2011]. Yang et al. showed that NSC elongation and neurite outgrowth along the fiber direction was promoted on the aligned electrospun fibers independent of the fiber diameter (average diameters 250 nm and 1.25 μm). Interestingly, neurite length was higher on the nanoscale compared to the microscale aligned fibers [F. Yang *et al*., 2005]. DRG sensory and motor neurites followed single PCL and PLLA fibers of submicron diameter (0.5 μm) and sometimes crossed the space between adjacent fibers [E. Schnell *et al*. 2007; M. Leach *et al*., 2011].

Globally isotropic topographies have been presented to neurons in the form of nano- or micron-scale pillars, posts and holes as well nano-roughness. The feature height ranged from 1-10μm. According to these studies, spacing of the features was the critical parameter for oriented neurite outgrowth. As the spacing between pillars increased, the fidelity of alignment decreased. Hippocampal neurons were cultured on square-shaped silicon pillars of 0.5 or 2 μm diameter and spacing ranging from 0.5 to 5 μm. The neurites tended to span the smallest distance between pillars, aligning either at 0° or 90°, with the highest alignment with the larger pillars at the smallest spacing. As the spacing between pillars increased, the fidelity of alignment decreased, and at 4.5 μm spacing, the distribution of neuronal arbor was similar to that found on a flat surface [N. Dowell-Mesfin *et al*., 2004]. In another study, hippocampal neurons have been cultured on conical posts of 10-100 μm diameter and respective height of 1/10 of the diameter and the edge-to-edge spacing ranging from 10-200μm [J. Hanson *et al*., 2009]. In this study, microcone's diameter and spacing were found to be two critical parameters in the neuron outgrowth process. Neurite processes on surfaces with smaller features and smaller intercone spacings were aligned and connected in straight lines between adjacent pillars. However, as microcone diameters started to increase, neurites wrap around the post they were already attached; this was more evident as the spacing increased beyond 40 μm. Furthermore, neurite

processes on surfaces with more than 200μm inter-feature spacing exhibited random outgrowth and wrapping. Therefore, as the feature size and spacing was increased, a transition from aligned to random growth occurred.

There are also a (small) number of studies reporting neurite outgrowth on patterned surfaces of a more random roughness. Usually, these substrates are fabricated via chemical or physical etching and surface roughness is controlled by variable exposure time to chemicals or physical agents, like plasma. In these cases, roughness is often measured in terms of an average feature size, called R_a. Some studies of neurons on globally isotropic surfaces with nanoscale features have been performed, with mixed results. Attachement of hippocampal neurons grown onto nanotextured titanium nitride films with R_a values from 1.3 to 5.6 nm was reduced compared to PDL coated glass. In two different studies neuronal adhesion and survival were affected in a unimodal manner when cultured on nanotextured silicon. In the first study, an intermediate value of R_a = 64 nm promoted an optimal response of embryonic primary cortical neurons and both higher and lower roughness reduced this response [S. Khan *et al*., 2005]. In another study, substantia nigra neurons survived for over 5 days with normal morphology and expressed neuronal TH when grown on surfaces with an average roughness (R_a) ranging from 20 to 50 nm. However, cell adherence was adversely affected on surfaces with Ra less than 10 nm and above 70 nm [Y. Fan *et al*., 2002]. Though nanoscale materials have received a great deal of attention in recent years, it is not yet clear role they could play in directing neuronal growth for tissue engineered applications [D. Hoffman-Kim *et al*., 2011].

In the present study, P1 rat sympathetic neurons have been cultured on collagen coated laser micropatterned Si substrates and the effect of the suggested topography on their outgrowth has been studied. **Although very few neurons could grow on the flat Si substrates, all micropatterned Si substrates did support extended neuronal outgrowth.** Therefore, in the present study, the importance of surface roughness over nerve cell outgrowth and network formation is emphasized and found to be in accordance with the results using PC12 cells. Neurons could equally well grow on all rough substrates and form neuronal network (Fig. 4.13). However, axonal outgrowth pattern was dependent on the underlying topography. More specifically, **the axons on the low roughness substrates showed a higher randomness, whereas the neurons on medium and high roughness substrates exhibited a parallel alignment** (Fig. 4.14-15). Although a limited number of neurons could grow on non coated

micropatterned substrates, the same effect of topography-guided axonal orientation was detected in this case as well (data not shown).

Although they exhibited different orientations, axons on low and medium substrates shared similar diameters. In particular, the neuronal network on the low and medium roughness substrates was dispersed and highly interconnected, consisting of mainly thin neurites with many branch points among them. On the contrary, axons growing on high roughness substrates were thicker and more densely packed, as if they grow into bundles (Fig. 4.16). This distinct fascicle-type morphology of axons has not been broadly studied *in vitro* in in relation to the underlying topography. A morphological analog of such axonal bundles could be found in axonal fascicles. Axonal fasciculation refers to the tendency for neighboring axons to stick to each other as they grow aided by cell adhesion molecules. Axon fasciculation is one of the processes controlling topographic innervation during embryonic development. While axon guidance steers extending axons in the accurate direction, axon fasciculation allows sets of co-extending axons to grow in tight bundles [M. Tessier-Lavigne and C. Goodman, 1996]. Fasciculation is driven by a balance of attractive and repulsive forces on the axons relative to their surrounding environment. Due to the complexity of mechanisms involved in regulating the initiation of fasciculation and defasciculation, elucidating fasciculation *in vitro* models remains challenging.

5.4 The effect of (surface) topography on Schwann cell morphology

The effect of the present topographical model was in turn studied on Schwann cells due to their importance on neuronal growth and functions. More specifically, Schwann cells provide a rich and supportive environment for neurite outgrowth through the release of neurotrophic factors, expression of cell surface ligands and synthesis of extracellular matrix (ECM). They present both molecular and topographical guidance stimuli to damaged peripheral nerves and they play important roles in the development, function and regeneration of peripheral nerve.

To this respect, P1 rat Schwann cells were grown on the laser micropatterned Si substrates. Although surface roughness did not influence Schwann cell growth (i.e. the cells were equally well grown on both flat and rough substrates), cell morphology was strikingly influenced by surface roughness (Fig. 4.10-11). **Elliptical discontinuous pattern, which was more pronounced at medium and high roughness Si substrates, promoted oriented Schwann cell outgrowth along the major axis of the ellipse** (Fig. 4.12). Schwann cells seemed to follow and

get aligned with the orientation of the microcone feature, which was accordingly more pronounced as the roughness increased. On the contrary, **cells on flat and low roughness substrates**, which exhibited a discontinuous random pattern, **had a random orientation**, resembling the growth pattern of the cells on flat Si substrate. It seemed that Schwann cells may "sense" and get aligned according to the underlying topography.

Various patterning techniques have been used to investigate Schwann cell preference for specific topographical cues, independent of substrate biochemistry. Two types of geometries have mainly been elaborated. The first consists of an anisotropic continuous geometry of parallelly oriented electrospun fibers, which were made of different synthetic polymers, such as PCL [S. Chew *et al*., 2008; D. Gupta *et al*., 2009], PAN-MA [V. Mukhatyar *et al*., 2011], PLA [J. Corey *et al*., 2007] or blend of synthetic and natural polymers, such as collagen/PCL [E. Schnell *et al*., 2007] or silk fibroin/polyLLA-co-(e-CL)] [K. Zhang *et al*., 2012]. In all these studies, when Schwann cells were cultured on aligned electrospun fibers of submicron-to-micron diameter (0.3-1μm), both cell cytoskeleton and nuclei were elongated and aligned along the fiber axes. On the contrary, cells cultured on random fibers exhibited random orientation [E. Schnell *et al.,* 2007; S. Chew *et al*., 2008; D. Gupta *et al*., 2009; V. Mukhatyar *et al*., 2011; K. Zhang *et al*., 2012]. Remarkably, (in one study) this change in morphology was accompanied by a change in maturation, as was confirmed by the up-regulation of early myelination markers and down-regulation of markers of immature Schwann cells [S. Chew *et al*., 2008]. When Schwann cells were cultured on aligned electrospun chitosan fibers of wider diameter (15μm), they migrated spiralling along the fibers end to end and the long olivary cells encircled the fibers in a 3D fashion [Y. Yuan *et al*., 2004].

The second consists of an anisotropic continuous geometry of alternating microgrooves and ridges. These were made of different materials, including polymers, such as PDMS [J. Mitchel and D. Hoffman-Kim, 2011] or PDLA [C. Miller *et al*., 2001] and hard materials, such as Si [M. Lietz *et al*., 2006]. According to these studies, groove width seems to be the key parameter for alignment of the Schwann cells. The width of Schwann cells varies from 5 to 10 μm and pattern widths or spacings ranging from 5 to 30μm were found to be optimal for the alignment of Schwann cells. More specifically, *J. Mitchell and D. Hoffman-Kim* studied the effect of anisotropic topography on rat Schwann cells growth cultured on laminin-coated microgrooved poly(dimethyl siloxane) platforms that were flat or presented repeating cellular

scale anisotropic topographical cues, 30 or 60 μm in width. They showed that the distance between the topographical features was important in determining the response of Schwann cell to microgrooved surfaces. A smaller distance (30μm *vs.* 60μm) between topographical features can reduce the prevalence of a multipolar morphology and result in movement that is more strongly oriented [J. Mitchel and D. Hoffman-Kim, 2011]. *Miller et al.* used microgrooved polymer substrates made of biodegradable PDLA. Groove width was found to be a signifcant factor in promoting Schwann cell alignment, and widths and spacings ranging from 10-20 μm were found to be optimal [C. Miller *et al*., 2001]. Smaller widths did not promote orientation because the groove widths were smaller than the cells, while larger widths were much larger than the cell size and therefore did not promote alignment. Groove depths of 1.4 μm or greater with initial cell seeding densities of greater than 50,000 cells/cm caused complete long-term alignment of the Schwann cells along the grooves. *M. Lietz et al*. used PDL/LN coated silicon chips with microgrooves of various widths (2-100 μm) and studied the effect of groove width on Schwann cell morphology. Whereas cells grown on non-structured areas appeared disorganized without preferential orientation, they displayed polar morphologies in parallel to the microgrooves when they were cultured on the micropatterned surfaces. It was shown that SCs were fully aligned on microgrooves of 2-10 μm width [M. Lietz *et al*., 2006]. In consistency with all these studies, the present study showed that even a discontinuous topographical pattern can promote Schwann cell alignment, provided that it contains an anisotropic feature (in our case an ellipse).

5.5 Topography-dependent neurite outgrowth and Schwann cell migration from DRG explant

It was then inquired whether the observed roughness- dependent growth orientation could be reproduced in a naturally occurring coculture system, which included the organotypic culture of dorsal root ganglion (DRG) explants. Interestingly, **both Schwann cell migration and axonal outgrowth exhibited a surface-dependent growth** (Fig. 4.18). More specifically, the cells on the low roughness substrates migrated away from the DRG explants at all possible directions (Fig. 4.19). In a similar way, the axons emanated from the DRG explants radially. However, on the intermediate and high roughness substrates (Fig. 4.20-21), which exhibit an anisotropic

topography, Schwann cell migration and axonal outgrowth exhibited a preferred parallel orientation towards a hypothetical horizontal axis.

Topography-dependant Schwann cell migration and axonal outgrowth from DRG explants have been demonstrated in different topographical models. The main topographical model used is the fibrous mat of parallel aligned electrospun fibers of micron (~up to 3 μm) or submicron (up to 500nm) diameter. Different types of polymers used include synthetic, such as PLA [J. Corey *et al*., 2007; H. Wang *et al*., 2010], Polydioxanone [Chow *et al*., 2009], Pan-MA [Y. Kim *et al*., 2008; V. Mukhatyar *et al*., 2011], PCL [J. Xie *et al*., 2009] or blend of synthetic and natural polymers, such as Collagen/PCL [E. Schnell *et al*., 2007]. Usually in these studies the fiber diameter is constant and (only) the orientation of the fibers is tuned (from random to highly parallel aligned). According to these studies, although DRG neurons grown on random electrospun polymer matrices show no directional preference, when the explants are grown on aligned matrices both axonal outgrowth and Schwann cell migration display directionality that mimics that of the underlying fiber orientation. Additionally, Schwann cells demonstrate the bipolar phenotype seen along the fiber. Remarkably, when seeded at the border between regions of aligned and random nanofibers, the same DRG simultaneously expressed aligned and random neurite fields in response to the underlying nanofibers [J. Xie *et al*., 2009].

X. Wen and P. Tresco studied the effect of filament diameter on DRG outgrowth. The fibers have been fabricated with the technique of thermal extrusion. An increasing pattern of neurite alignment and outgrowth and Schwann cell migration in the direction parallel to the long axis of the packed filament bundles with decreasing filament diameter, ranging from supracellular and beyond (500 to 100 μm), cellular (30 μm), down to subcellular size (5 μm) was observed. Neurites and Schwann cells were highly aligned and in close apposition along the 5 μm filaments. Interestingly, this increase in axial alignment was accompanied by a decrease in neurite fasciculation as the filament diameter decreased. More specifically, while on 500 μm-diameter filaments, neurites appeared organized into fascicles, neurite outgrowth on the smallest values diameters (i.e on 5 and 30μm) was dense, spread out, and uniformly distributed. This defasciculation as the filament diameter decreases was attributed to the increase of surface area giving more space for cells to adhere and grow [X. Wen and P. Tresco, 2006].

Some other topographical models have also been used. J. Richardson *et al*. have fabricated PDMS replicas of Schwann cell monolayer in random or aligned orientations via

replica-molding technique. PDMS conduits containing Schwann cell topography were in turn fabricated from these replicas, and DRG neurite outgrowth and morphological characteristics were analyzed. It was shown that DRG neurite outgrowth and morphology within conduits and on two-dimensional SC replicas were directed by the underlying Schwann cell topographical features [J. Richardson *et al*., 2011]. With this study the contribution of Schwann cell topography isolated from any biochemical influence to neurite guidance was emphasized. Microcontact printing was also used to create 2D patterns of proteins (laminin-LN- and chondroitin sulfate proteoglycans-CSPG) on glass coverslips. The micropattern consisted of parallel 50 μm stripes of 1 cm length separated by 50 μm spaces [C. Kofron *et al*., 2009]. On LN micropatterned substrates, more than 90% of the neurite segments from explants extended in the direction of the patterns, while no alignment was observed in 2D cultures of explants on control substrates (LN coated glass). On the contrary, DRG explants did not adhere and thus did not extend neurites on any of the coverslips containing CSPG, which is an inhibitor of neuronal growth. Interestingly, 2D micropatterned CSPG substrates did allow growth of dissociated DRG neurons.

It has to be mentioned that all topographical models described above, display continuous topographies according to the classification of 1.3.1 (Fig. 1.5). To the best of our knowledge, the effect of discontinuous topography on anisotropic DRG explant growth has not been exploited. The results presented here suggest that this specific type of discontinuous microconical topography is sufficient to promote DRG explant adhesion overcoming the necessity for protein coating. Furthermore, this topographical model can induce isotropic or anisotropic Schwann cell migration and axonal outgrowth in a topography-dependent manner

5.6 Organization of fibronectin on micropatterned Si substrates

The morphological analysis of the DRG growth on the laser micropatterned Si substrates revealed that migrating cells developed on top of the substrate's microcones. The cells migrated away from the explant in a topography-dependent manner. More specifically, the cells largely followed single microcone directions and migrated along the "corridor" created by the sequential lines of the microcones (Fig. 4.22-23). Moreover, confocal microscopy analysis revealed that **the migrating glial cells created a "carpet" onto which the neurites could grow** (Fig.4.28-29).

Interaction between axons and Schwann cells plays a fundamental role in the normal development and successful regeneration of peripheral injured nerves. During early

development, Schwann cells originating from the neural crest migrate along the embryonic nerve toward the growth cones. After this initial migration along the axonal surfaces, Schwann cells migrate radially into the nerve bundles, divide actively, and eventually separate and ensheath individual axons. Following transection of peripheral nervous trunk, Schwann cells proliferate and elaborate a scaffold of basement membrane proteins (including laminin and fibronectin) in advance of the regrowing axons to promote regeneration. Glial cell migration and reorganisation leads to the temporary formation of a longitudinally oriented framework of overlapping Schwann cell processes which is associated with directional axon regeneration [R. Bunge, 1987; G. Brook *et al*., 1998].

Therefore, Schwann cells modify their environment by synthesizing and secreting extracellular matrix (ECM) components. To this respect, the organization of fibronectin (Fn), which is an important ECM molecule, on the herein described topographical model, was studied. Fn and its main receptor, α5β1, are found in the basal lamina of Schwann cells and perineurial cells [Palm and Furcht, 1983; Lefcort *et al*., 1992]. The strongest Fn expression is found during the embryonic development in axons and Schwann cells, whereas it is downregulated in the adult and strongly re-expressed after injury [Lefcort *et al*., 1992]. Fn is believed to have a role during development in Schwann cell precursor migration [A. Baron Van Evercooren *et al*., 1982; Milner *et al*., 1997] and in nerve regeneration through facilitation of axonal outgrowth and Schwann cell proliferation [A. Baron Van Evercooren *et al*., 1982]. Most cells assemble rich matrices via an integrin-dependent contractile process that incorporates Fn molecules, either synthesized by cells or reorganized from their surroundings, into matrix fibrils [Y. Mao and J. Schwarzbauer, 2005; M. Salmerón-Sánchez *et al*., 2011].

Organization of Fn (molecules) into a physiological fibrillar network upon adsorption on micropatterned (material) surfaces has not been thoroughly investigated. *L. Chou et al.* have studied the regulation of cell shape, fibronectin mRNA level, secretion and assembly by substratum surface topography in human gingival fibroblasts cultured on titanium-coated smooth or V-shaped grooved substrata produced by micromachining [L. Chou *et al*., 1995]. Interestingly, substratum surface topography alters cell shape and modulates fibronectin at the transcriptional and post-transcriptional levels, as well as the amount of fibronectin assembled into extracellular matrix. In another interesting study, V. Mukhatyar *et al*. used thin films consisting of aligned poly-acrylonitrile methyl acrylate (PAN-MA) fibers in order to investigate the potential role of

differential protein adsorption on topography-dependent neurite outgrowth and Schwann cell migration from DRG explants. It was shown that organization of Fn secreted by glial cells cultured on aligned fibers was enhanced by underlying topographical cues. Aligned fibers enabled formation of organized Fn network compared to smooth films. Fn adsorption mediated the ability of topographical cues to influence Schwann cell migration and neurite outgrowth from DRG explants [V. Mukhatyar *et al*., 2011].

In this study, in order to investigate the organization of Fn in relation to the migrating non neuronal cells and outgrown neuritis, whole DRG explants were applied onto the laser micropatterned Si substrates. Confocal microscopy analysis at high magnification showed that **the outgrowth of extracellular Fn was organized into many parallell fibers in the region around the neighboring migrating cells** (Fig. 4.31-33). Interestingly, **its organization had a similar orientation with the one of the outgrown neuritis**. Therefore, axons were shown to grow within an interconnected network of Fn fibrils.

5.7 Neurons-Schwann cell interactions on micropatterned Si substrates

Results from dissociated cultures showed that both cell types of the peripheral nervous system (i.e. sympathetic and sensory neurons and Schwann cells) can grow on the micropatterned substrates, exhibiting a roughness-dependent growth orientation. The more complex model of DRG whole explants revealed that Schwann cells create a cellular "carpet" onto the substrates. Neurons were, in turn, outgrown on top of them. Therefore, the **following hypothesis is formulated**: **The plasticity of Schwann cells and their processes allowed them to create a "carpet". This glial cell "carpet" served as a substrate for the outgrown neuritis.** Neurite guidance is likely influenced by both the topography of the Schwann cell monolayer and molecules expressed on the Schwann cell surface.

In order to confirm this hypothesis, coculture of dissociated sympathetic neurons and Schwann cells was performed. **Schwann cells were grown on micropatterned Si substrates. Sympathetic neurons grown on top of them followed Schwann cell orientation** (Fig. 4.17). Therefore, a Schwann cell-directed neurite outgrowth on the present topographical models is reported. Aligned monolayers of Schwann cells have been shown that can direct neuronal outgrowth to follow the direction of alignment even in the absence of other topographical cues [A. Seggio *et al*., 2010]. D. *Thompson and H. Buttner* fabricated micropatterned laminin

substrates onto which Schwann cell were grown. Schwann cell outgrowth orientation was similar to that of the underlying protein pattern. Dissociated rat spinal neurons were seeded onto oriented Schwann cell monolayers, whose alignment provided the only directional cue for growing neuritis. It was shown that the orientation of neurite outgrowth mimicked that of the Schwann cells [D. Thompson and H. Buettner, 2006]. *M. Lietz et al*. used PDL/LN coated Si microgrooved substrates, onto which Schwann cells were grown. When Schwann cells were preseeded onto grooved scaffolds of 15 μm depth, over 60% of them aligned on 50 and 100 μm width grooves, while over 90% aligned on 2-20 μm grooves. These substrates were presented to DRG neurons and neurites were shown to run parallel to pre-oriented SCs.

These studies confirm the guidance effect of Schwann cells on neurite outgrowth (of sympathetic and sensory neurons). However, this guidance effect could be described as the result of two components, not easily differentiable in the *in vitro* culture models. The first includes the topographical cues induced by Schwann cells themselves (orientation, microroughness, etc.). The second involves all biochemical components secreted by Schwann cells, necessary in axon-Schwann cell interactions. In this respect, a replica molding technique has been developed in order to replicate Schwann cell surface onto a polymer [J.Bruder *et al*., 2006]. By isolating Schwann cell topographical from biochemical components, the contribution of solely Schwann cell topography in neurite guidance could be studied *in vitro*. According to this study, DRG neurons grown on such LN coated PDMS impression replicas extended neurites that aligned along features that replicated Schwann cell topography.

5.8 Investigation of cellular growth and neuronal and non-neuronal cell functions on laser micropatterned Si surfaces - Conclusion

The present study evokes a novel type of semiperiodical discontinuous topography with anisotropic features. This geometry intended to test the effect of surface architecture on cellular development and morphology, beyond the well-studied anisotropic continuous geometries (i.e. grooves, ridges, parallel fibers, etc.) or isotropic discontinuous geometries (i.e. pillars or posts). The simplicity of the irradiation process offers the possibility of patterning areas with different degrees of roughness on the same culture substrate. The construction of a single scaffold containing all three different roughness ratios allowed direct comparison of the effect of MCs topology on cell growth preference.

It was shown that **these distinct geometrical characteristics of surface roughness could influence a variety of neuronal and neuroglial cell functions**, however in a different manner. In the PC12 cell study, the interspike space -among the different topographical characteristics of MCs-, did effectively influence PC12 cells' differentiation fate. It seems that the anisotropy in geometry did not play an important role. On the contrary, in primary cell cultures, it was shown that the distinct anisotropic morphology of the microconical surfaces did strikingly influence the outgrowth orientation of both neurons and Schwann cells in a surface-dependent manner. This surface -induced guidance effect was observed in both single and more complex cell cultures (like co-culture and organotypic whole DRG explants model). It can be concluded from this study that **even a discontinuous topographical pattern can promote Schwann cell and axonal alignment, provided that it contains an anisotropic feature (in this case an ellipse)**.

The laser patterned silicon (Si) substrates presented here could potentially be used as model scaffolds for the systematic exploration of the role of 3D microtopography on cell differentiation and neural network outgrowth and to investigate other Schwann cell–neuronal interactions that may be important in successful regeneration, with the ultimate goal of providing mechanistic insight to guide the development of clinically relevant strategies for nerve repair.

6. References

Adams JC, Watt FM, 1993, *Regulation of development and differentiation by the extracellular matrix*, **Development**, 117: 1183.

Al-Bayati AH, Orrman-Rossiter KG, Van den Berg JA, Armour DG, 1991, *Composition and structure of the native Si oxide by high depth resolution medium energy ion scattering*, **Surface Science**, 241:91.

Alberts B, Alexander J, Lewis J, Raff M, Roberts K, Walter P, 2002, **Molecular Biology of the Cell**, New York, Garland Science

Anderson D, Axel R, 1986, *A bipotential neuroendocrine precursor whose choice of cell fate is determined by NGF and glucocorticoids*, **Cell**, 47:1079.

Andersson H, Van den Berg A, 2004, *Microfabrication and microfluidics for tissue engineering: state of the art and future opportunities*, **Lab on a Chip**, 4:98.

Anton ES, Weskampt G, Reichardt LF, Matthew WD, 1994, *Nerve growth factor and its low-affinity receptor promote Schwann cell migration*, **Proc Natl Acad Sci U S A**, 91:2795.

Barberoglou M, 2012, *Femtosecond laser micro/nano structuring of solid surfaces: Fundamentals and applications*, PhD thesis, University of Crete, Heraklion

Baron-Van Evercooren A, Kleinman HK, Seppa HE, Rentier B, Dubois-Dalq M, 1982, *Fibronectin Promotes Rat Schwann Cell Growth and Motility*, **The Journal of Cell Biology**, 93:211.

Bellamkonda RV, 2006, *Peripheral nerve regeneration: An opinion on channels, scaffolds and anisotropy*, **Biomaterials**, 27:3515.

Bettinger CJ, Langer R, Borenstein JT, 2009, *Engineering Substrate Topography at the Micro- and Nanoscale to Control Cell Function*, **Angew Chem Int Edit**, 48:5406.

Bhushan B, 1990, *Solid Surface Characterization*, In **Tribology and Mechanics of Magnetic Storage Devices**, Springer US

Birk DE, Zycband EI, Winkelmann DA, Trelstad RL, 1989, *Collagen fibrillogenesis in situ: fibril segments are intermediates in matrix assembly*, **Proc Natl Acad Sci U S A**, 86:4549.

Bissell MJ, Hall HG, Parry G, 1982, *How Does the Extracellular Matrix Direct Gene Expression?*, **J. Theor. Biol.** , 99:31.

Brook GA, Plate D, Franzen R, Martin D, Moonen G, et al, 1998, *Spontaneous Longitudinally Orientated Axonal Regeneration Is Associated With the Schwann Cell Framework Within the Lesion Site Following Spinal Cord Compression Injury of the Rat*, **Journal of Neuroscience Research**, 53:51.

Brown MS, Arnold CB, 2010, *Fundamentals of Laser-Material Interaction and Application to Multiscale Surface Modification*, In **Laser Precision Microfabrication**, ed. K Sugioka, M Meunier, A Piqué, Springer Series in Materials Science

Bucaro MA, Vasquez Y, Hatton BD, Aizenberg J, 2012, *Fine-tuning the degree of stem cell polarization and alignment on ordered arrays of high-aspect-ratio nanopillars*, **ACS Nano**, 6:6222.

Bunge RP, 1987, *Tissue culture observations rleevant to the study of axon-Schwann cell interactions during peripheral nerve development and repair*, **J. Exp. Biol.** , 132:21.

Bunge RP, Bunge MB, 1978, *Evidence that contact with connective tissue matrix is required for normal interaction between Schwann cells and nerve fibers*, **The Journal of Cell Biology**, 78:943.

Bunge RP, Fernandez-Valle C, 1995, *Basic Biology of the Schwann Cell*, In **Neuroglia**, ed. H Kettenmann, BR Ransom, Oxford University Press

Burnett MG, Zager EL, 2004, *Pathophysiology of peripheral nerve injury: a brief review*, **Neurosurg Focus**, 16:1.

Canty EG, Lu Y, Meadows RS, Shaw MK, Holmes DF, Kadler KE, 2004, *Coalignment of plasma membrane channels and protrusions (fibripositors) specifies the parallelism of tendon*, **The Journal of Cell Biology**, 165:553.

Carrey J, 2004, *Femtosecond-laser Microstructuring of Silicon for Novel Optoelectronic Devices*, PhD thesis, Harvard University Cambridge, Massachusetts

Carter M, Shieh J, 2010, **Guide to research techniques in neuroscience**, Academic Press

Cecchini M, Bumma G, Serresi M, Beltram F, 2007, *PC12 differentiation on biopolymer nanostructures*, **Nanotechnology**, 18:505103.

Chew SY, Mi R, Hoke A, Leong KW, 2008, *The Effect of the Alignment of Electrospun Fibrous Scaffolds on Schwann Cell Maturation*, **Biomaterials**, 29:653.

Chou L, Firth JD, Uitto VJ, Brunette DM, 1995, *Substratum surface topography alters cell shape and regulates fibronectin mRNA level, mRNA stability, secretion and assembly in human fibroblasts.*, **J Cell Sci.**, 108:1563.

Chow WN, Simpson DG, Bigbee JW, Colello RJ, 2007, *Evaluating neuronal and glial growth on electrospun polarized matrices: bridging the gap in percussive spinal cord injuries*, **Neuron Glia Biol.**, 3: 119.

Christopherson GT, Song H, Mao HQ, 2009, *The influence of fiber diameter of electrospun substrates on neural stem cell differentiation and proliferation*, **Biomaterials**, 30:556.

Corey JM, Lin DY, Mycek KB, Chen Q, Samuel S, et al, 2007, *Aligned electrospun nanofibers specify the direction of dorsal root ganglia neurite growth*, **Journal of Biomedical Materials Research Part A**, 83A:636.

Cortadellas N, Fernández E, Garcia A. 2012. *Biomedical and Biological Applications of Scanning Electron Microscopy.* Handbook of instrumental techniques. Scientific and Technological Centers of the University of Barcelona

Cyster LA, Parker KG, Parker TL, Grant DM, 2004, *The effect of surface chemistry and nanotopography of titanium nitride (TiN) films on primary hippocampal neurones*, **Biomaterials**, 25:97.

Das KP, Freudenrich TM, Mundy WR, 2004, *Assessment of PC12 cell differentiation and neurite growth: a comparison of morphological and neurochemical measures*, **Neurotoxicology and Teratology**, 26:397.

Deal BE, Grove AS, 1965, *General Relationship for the Thermal Oxidation of Silicon* **Journal of applied physics**, 36:3770.

Dee KC, Puleo DA, Bizios R, 2003, **An Introduction to Tissue-Biomaterial Interactions**, John Wiley & Sons, Inc.

Dolgaev SI, Lavrishev SV, Lyalin AA, Simakin AV, Voronov VV, Shafeev GA, 2001, *Formation of conical microstructures upon laser evaporation of solids*, **Applied Physics A: Materials Science & Processing**, 73:177.

Dowell-Mesfin NM, Abdul-Karim M-A, Turner AM, Schanz S, Craighead HG, et al, 2004, *Topographically modified surfaces affect orientation and growth of hippocampal neurons*, **J. Neural Eng.** , 1:78.

Dunn GA, Heath JP, 1976, *A new hypothesis of contact guidance in tissue cells*, **Experimental Cell Research**, 101:1.

Fan YW, Cui FZ, Hou SP, Xu QY, Chen LN, Lee I-S, 2002, *Culture of neural cells on silicon wafers with nano-scale surface topography*, **Journal of Neuroscience Methods**, 120:17.

Ferrari A, Cecchini M, Dhawan A, Micera S, Tonazzini I, et al, 2011, *Nanotopographic Control of Neuronal Polarity*, **Nano Letters**, 11:505.

Flemming RG, Murphy CJ, Abrams GA, Goodman SL, Nealey PF, 1999, *Effects of synthetic micro- and nano-structured surfaces on cell behavior*, **Biomaterials**, 20:573.

Foley JD, Grunwald EW, Nealey PF, Murphy CJ, 2005, *Cooperative modulation of neuritogenesis by PC12 cells by topography and nerve growth factor*, **Biomaterials**, 26:3639.

Gaudet AD, Popovich PG, Ramer MS, 2011, *Wallerian degeneration: Gaining perspective on inflammatory events after peripheral nerve injury*, **Journal of Neuroinflammation**, 8:110.

Goldner JS, Bruder JM, Li G, Gazzola D, Hoffman-Kim D, 2006, *Neurite bridging across micropatterned grooves*, **Biomaterials**, 27:460.

Gomez N, Lu Y, Chen S, Schmidt CE, 2007, *Immobilized nerve growth factor and microtopography have distinct effects on polarization versus axon elongation in hippocampal cells in culture*, **Biomaterials**, 28:271.

Greene LA, Farinelli SE, Cunningham ME, Park DS, 1998, *Culture and Experimental Use of the PC12 Rat Pheochromocytoma Cell Line*, In **Culturing Nerve Cells**, ed. G Banker, K Goslin, The MIT press

Greene LA, Tischler AS, 1976, *Establishment of a noradrenergic clonal line of rat adrenal pheochromocytoma cells which respond to nerve growth factor*, **Proc. Natl. Acad. Sci. USA**, 73:2424.

Gupta D, Venugopal J, Prabhakaran M, Dev VR, Low S, et al, 2009, *Aligned and random nanofibrous substrate for the in vitro culture of Schwann cells for neural tissue engineering*, **Acta Biomaterialia**, 5:2560.

Guroff G, 1985, *PC12 Cells as a Model of Neuronal Differentiation* In **Cell Culture in the Neurosciences**, ed. JE Bottenstein, G Sato, Springer US

Hallstrom W, Martensson T, Prinz C, Gustavsson P, Montelius L, et al, 2007, *Gallium phosphide nanowires as a substrate for cultured neurons*, **Nano Lett.** , 7:2960.

Hanson JN, Motala MJ, Heien ML, Gillette M, Sweedler J, Nuzzo RG, 2009, *Textural guidance cues for controlling process outgrowth of mammalian neurons*, **Lab Chip**, 9:122.

Haq F, Anandan V, Keith C, Zhang G, 2007, *Neurite development in PC12 cells cultured on nanopillars and nanopores with sizes comparable with filopodia*, **Int J Nanomed**, 2:107.

Hatten ME, 1990, *Riding the glial monorail: a common mechanism for glial- guided neuronal migration in different regions of the developing mammalian brain*, **TINS**, 13:179.

Hierlemann A, *Thermal Oxidation of Silicon*, **Microtechnology and microelectronics**.

Hoffman-Kim D, Mitchel JA, Bellamkonda RV, 2010, *Topography, Cell Response, and Nerve Regeneration*, **Annu Rev Biomed Eng**, 12:203.

Hollinger G, Jugnet Y, Pertosa P, Minh Duc T, 1975, *X-ray photoelectron spectroscopy of thermally grown silicon dioxide films on silicon* **Chemical physics letters**, 36:441.

Hunt LP, 1990, *Silicon Precursors: Their Manufacture and Properties* In **Handbook of semiconductor silicon technology**, ed. WC O'Mara, RB Herring, LP Hunt, Noyes Publications

Hurtado A, Cregg JM, Wang HB, Wendell DF, Oudega M, et al, 2011, *Robust CNS regeneration after complete spinal cord transection using aligned poly-l-lactic acid microfibers*, **Biomaterials**, 32,.

Ibach H, Rowe JE, 1974, *Electron orbital energies of oxygen adsorbed on silicon surfaces and of silicon dioxide* **Phys. Rev. B**, 10:710.

Jingwei X, MacEwan MR, Li X, Sakiyama-Elbert SE, Xia Y, 2009, *Neurite Outgrowth on Nanofiber Scaffolds with Different Orders, Structures, and Surface Properties*, **ACS Nano**, 3:1151.

Johansson F, Carlberg P, Danielsen N, Montelius L, Kanje M, 2006, *Axonal outgrowth on nano-imprinted patterns*, **Biomaterials**, 27:1251.

Johnson MI, 2001, *Primary Cultures of Sympathetic Ganglia*, In **Protocols for Neural Cell Culture**, ed. LC Doering, Humana Press

Jolly F, Rochet F, Dufour G, Grupp C, Taleb-Ibrahimi A, 2001, *Oxidized silicon surfaces studied by high resolution Si 2p core-level photoelectron spectroscopy using synchrotron radiation*, **Journal of Non-Crystalline Solids**, 280:150.

Kandel ER, Schwartz JH, Jessell TM, 2000, **Principles of Neural Science**, McGraw-Hill

Kettenmann H, Ransom BR, 1995, **Neuroglia**, Oxford University Press

Khan SP, Auner GG, Newaz GM, Tai YC, 2005, *Influence of nanoscale surface roughness on neural cell attachment on silicon*, **Nanomedicine: Nanotechnology, Biology, and Medicine**, 1:125.

Kim D-H, Provenzano PP, Smith CL, Levchenko A, 2012, *Matrix nanotopography as a regulator of cell function*, **J. Cell Biol.**, 197:351.

Kim HA, Maurel P, 2010, *Primary Schwann Cell Cultures*, In **Protocols of neural cell culture**, ed. LC Doering, Humana Press

Kim Y, Haftel VK, Kumar S, Bellamkonda RV, 2008, *The role of aligned polymer fiber-based constructs in the bridging long peripheral nerve gaps*, **Biomaterials**, 29:3117.

Kisa M, 2004, *Silicon oxidation by atomic and molecular oxygen*, MSc thesis, University of Pittsburgh

Kofron CM, Fong VJ, Hoffman-Kim D, 2009, *Neurite outgrowth at the interface of 2D and 3D growth environments*, **J. Neural Eng.** , 6: 016002

Koh HS, Yong T, Chan CK, Ramakrishna S, 2008, *Enhancement of neurite outgrowth using nano-structured scaffolds coupled with laminin.*, **Biomaterials**, 29:3574.

Leach MK, Feng Z-Q, Gertz CC, Tuck SJ, Regan TM, et al, 2011, *The Culture of Primary Motor and Sensory Neurons in Defined Media on Electrospun Poly-L-lactide Nanofiber Scaffolds*, **Journal of Visualized Experiments**.

Lee JY, Bashur CA, Goldstein AS, Schmidt CE, 2009, *Polypyrrole-coated electrospun PLGA nanofibers for neural tissue applications*, **Biomaterials**, 30:4325.

Lefcort F, Venstrom K, McDonald JA, Reichardt LF, 1992, *Regulation of expression of fibronectin and its receptor, alpha 5 beta 1, during development and regeneration of peripheral nerve.*, **Development**, 16:767.

Lelkes PI, Unsworth BR, Saporta S, Cameron DF, Gallo G, 2006, *Culture of Neuroendocrine and Neuronal Cells for Tissue Engineering*, In **Culture of Cells for Tissue Engineering**, ed. G Vunjak-Novakovic, R Ian Freshney, Wiley-Liss

Li N, Folch A, 2005, *Integration of topographical and biochemical cues by axons during growth on microfabricated 3-D substrates*, **Experimental Cell Research**, 311:307

Li Y, Huang G, Zhang X, Wang L, Du Y, et al, 2014, *Engineering cell alignment in vitro*, **Biotechnology Advances**, 32:347.

Lichtman JW, Conchello J-A, 2005, *Fluorescence microscopy*, **Nature methods**, 2:910.

Lietz M, Dreesmann L, Hoss M, Oberhoffner S, Schlosshauer B, 2006, *Neuro tissue engineering of glial nerve guides and the impact of different cell types*, **Biomaterials**, 27:1425.

Lin CH, Forscher P, 1993, *Cytoskeletal remodeling during growth cone-target interactions*, **J Cell Biol**, 121:1369.

Liu X, Chen J, Gilmore KJ, Higgins MJ, Liu Y, Wallace GG, 2010, *Guidance of neurite outgrowth on aligned electrospun polypyrrole/poly(styrene-β-isobutylene-β-styrene) fiber platforms*, **Journal of Biomedical Materials Research Part A**, 94:1004.

Logofatu C, Negrila C-C, Ghita RV, Ungureanu F, Cotirlan C, et al, 2011, *Study of SiO2/Si Interface by Surface Techniques*, In **Crystalline Silicon - Properties and Uses**

Luckenbill - Edds L, Van Horn C, Greene LA, 1979, *Fine structure of initial outgrowth of processes induced in a pheochromocytoma cell line (PC12) by nerve growth factor*, **Journal of Neurocytology**, 8:493.

Ludwig KA, Uram JD, Yang J, Martin DC, Kipke DR, 2006, *Chronic neural recordings using silicon microelectrode arrays electrochemically deposited with a poly(3,4-ethylenedioxythiophene) (PEDOT) film*, **J. Neural Eng.** , 3:59.

Mahanthappa NK, Anton ES, Matthew WD, 1996, *Glial Growth Factor 2, a Soluble Neuregulin, Directly Increases Schwann Cell Motility and Indirectly Promotes Neurite Outgrowth*, **The Journal of Neuroscience**, 16:4673.

Maher MP, Pine J, Wright J, Tai YC, 1999, *The neurochip: a new multielectrode device for stimulating and recording from cultured neurons*, **Journal of Neuroscience Methods**, 87:45.

Mahoney MJ, Chen RR, Tan J, Mark Saltzman W, 2005, *The influence of microchannels on neurite growth and architecture*, **Biomaterials**, 26:771.

Mao S-Y, Javois LC, Kent UM, 1999, *Overview of Antibody Use in Immunocytochemistry*, In **Immunocytochemical Methods and Protocols**, ed. LC Javois, Humana Press

Mao Y, Schwarzbauer JE, 2005, *FN fibrillogenesis, a cell-mediated matrix assembly process.*, **Matrix Biol.**, 24:389.

Margolis LB, Samoilov VI, Vasiliev JM, Gelfand IM, 1975, *Quantitative evaluation of cell orientation in culture* **J. Cell Set.** , 17:1.

Martínez E, Engel E, Planell JA, Samitier J, 2009, *Effects of artificial micro- and nano-structured surfaces on cell behaviour*, **Annals of Anatomy - Anatomischer Anzeiger**, 191:126.

McNamara LE, McMurray RJ, Biggs MJ, Kantawong F, Oreffo RO, Dalby MJ, 2010, *Nanotopographical control of stem cell differentiation*, **J Tissue Eng**, 2010:120623.

Merz M, Fromherz P, 2005, *Silicon Chip Interfaced with a Geometrically Defined Net of Snail Neurons*, **Advanced Functional Materials**, 15:739.

Miller C, Shanks H, Witt A, Rutkowski G, Mallapragad S, 2001, *Oriented Schwann cell growth on micropatterned biodegradable polymer substrates*, **Biomaterials**, 22:1263.

Mingorance-Le Meur A, Mohebiany AN, O'Connor TP, 2009, *Varicones and growth cones: two neurite terminals in PC12 cells*, **PLoS One**, 4:e4334.

Mitchel JA, Hoffman-Kim D, 2011, *Cellular Scale Anisotropic Topography Guides Schwann Cell Motility*, **PLoS ONE**, 6:e24316.

Moore SW, Sheetz MP, 2011, *Biophysics of Substrate Interaction: Influence on Neural Motility, Differentiation, and Repair*, **Develop Neurobiol.**, 71:1090.

Morita M, Ohmi T, Hasegawa E, Kawakami M, Ohwada M, 1990, *Growth of native oxide on a silicon surface*, **J. Appl. Phys.** , 68:1272.

Mukhatyar V, Salmerón-Sánchez M, Rudra S, Mukhopadaya S, Barker TH, et al, 2011, *Role of fibronectin in topographical guidance of neurite extension on electrospun fibers*, **Biomaterials**, 32: 3958.

Nagata I., Kawana A, Nakatsuji N, 1993, *Perpendicular contact guidance of CNS neuroblasts on artificial microstructures*, **Development**, 117:401.

Nedzved A, Belotserkovsky A, Ablameyko S. 2005. Detection of cells orientation factor for cancer diagnostics. In *The International Conference on Advanced Information and Telemedicine Technologies for HealthUIIP NASB*, pp. 183. Minsk, Belarus

Noori A, Upadhyaya S, Selvanganapathy PR, 2008, *Materials and Microfabrication Processes for Microfluidic Devices* In **Microfluidics for Biological Applications**, ed. EF Wei-Cheng Tian Springer

Norman JJ, Desai TA, 2006, *Methods for fabrication of nanoscale topography for tissue engineering scaffolds*, **Ann Biomed Eng**, 34:89.

Ortinau S, Schmich J, Block S, Liedmann A, Jonas L, et al, 2010, *Effect of 3D-scaffold formation on differentiation and survival in human neural progenitor cells*, **Biomed Eng Online**, 9:70.

Palsson BO, Bhatia SN, 2004, **Tissue Engineering**, Pearson Prentice Hall

Papadopoulou EL, Samara A, Barberoglou M, Manousaki A, Pagakis SN, et al, 2010, *Silicon scaffolds promoting three-dimensional neuronal web of cytoplasmic processes*, **Tissue Eng Part C Methods**, 16:497.

Park J, Koito H, Li J, Han A, 2009, *Microfluidic compartmentalized co-culture platform for CNS axon myelination research*, **Biomedical Microdevices**, 11:1145.

Park TH, Shuler ML, 2003, *Integration of cell culture and microfabrication technology*, **Biotechnol Prog.** , 19:243.

Pearce TM, Williams JC, 2007, *Microtechnology: Meet neurobiology*, **Lab on a Chip**, 7:30.

Pearse DD, Pereira FC, Marcillo AE, Bates ML, Berrocal YA, et al, 2004, *cAMP and Schwann cells promote axonal growth and functional recovery after spinal cord injury.*, **Nat Med.**, 10:610.

Pedraza AJ, Fowlkes JD, Lowndes DH, 1999, *Silicon microcolumn arrays grown by nanosecond pulsed-excimer laser irradiation*, **Phys. Lett.** , 74:2322

Petersen KE, 1982, *Silicon as a Mechanical Material*, **Proceedings of the IEEE**, 70.

Petreaca M, Martins-Green M, 2007, *The Dynamics of Cell–ECM Interactions*, In **Principles of Tissue Engineering**, ed. L Lanza, and Vacanti, Academic Press

Qin D, Xia Y, Rogers JA, Jackman RJ, Zhao X-M, Whitesides GM, 1998, *Microfabrication, Microstructures and Microsystems*, **Topics in Current Chemistry**, 194:1.

Queirolo G, Manzini S, Meda L, Anderle M, Canteri R, et al, 1988, *On the silicon dioxide/polycrystalline silicon interface width measurement*, **Surface and Interface Analysis**, 13:202.

Rajnicek AM, Britland S, McCaig CD, 1997, *Contact guidance of CNS neurites on grooved quartz: influence of groove dimensions, neuronal age and cell type*, **J Cell Sci**, 110:2905.

Ranella A, Barberoglou M, Bakogianni S, Fotakis C, Stratakis E, 2010, *Tuning Cell Adhesion by controlling the roughness and wettability of 3D micro/nano silicon structures*, **Acta Biomaterialia**, 6: 2711.

Rangappa N, Romero A, Nelson KD, Eberhart RC, Smith GM, 2000, *Laminin-coated poly(L-lactide) filaments induce robust neurite growth while providing directional orientation*, **J Biomed Mater Res.** , 51:625.

Ratner B, Hoffman A, Schoen F, Lemons J, 2004, **Biomaterials Science; An Introduction to Materials in Medicine**, Academic Press

Ribeiro-Resende VT, Koenig B, Nichterwitz S, Oberhoffner S, Schlosshauer B, 2009, *Strategies for inducing the formation of bands of Bu¨ngner in peripheral nerve regeneration*, **Biomaterials**, 30:5251.

Richardson JA, Rementer CW, Bruder JM, Hoffman-Kim D, 2011, *Guidance of dorsal root ganglion neurites and Schwann cells by isolated Schwann cell topography on poly(dimethyl siloxane) conduits and films*, **J. Neural Eng.** , 8:046015.

Rosso F, Giordano A, Barbarisi M, Barbarisi A, 2004, *From Cell–ECM Interactions to Tissue Engineering*, **Journal of cellular physiology**, 199:174.

Saile V, Wallrabe U, Tabata O, Korvink JG, 2009, *Introduction: LIGA and Its Applications* In **LIGA and Its Applications**, Verlag GmbH & Co

Salmerón-Sánchez M, Rico P, Moratal D, Lee TT, Schwarzbauer JE, García AJ, 2011, *Role of material-driven fibronectin fibrillogenesis in cell differentiation*, **Biomaterials**, 32:2099.

Schindler M, Nur-E-Kamal A, Ahmed I, Kamal J, Liu HY, et al, 2006, *Living in three dimensions - 3D nanostructured environments for cell culture and regenerative medicine*, **Cell Biochem Biophys**, 45:215.

Schnell E, Klinkhammer K, Balzer S, Brook G, Klee D, et al, 2007, *Guidance of glial cell migration and axonal growth on electrospun nanofibers of poly-e-caprolactone and a collagen/poly-e-caprolactone blend*, **Biomaterials**, 28:3012.

Seggio AM, Narayanaswamy A, Roysam B, Thompson DM, 2010, *Self-aligned Schwann cell monolayers demonstrate an inherent ability to direct neurite outgrowth*, **J. Neural Eng.**, 7: 046001

Shen MY, Crouch CH, Carey JE, Mazur E, 2004, *Femtosecond laser-induced formation of submicrometer spikes on silicon in water* **Appl. Phys. Lett.** , 85:5694.

Sievila P, 2013, *Microfabrication technologies for single-crystal sensors*, PhD thesis, Aalto University

Simitzi C, Stratakis E, Fotakis C, Athanassakis I, Ranella A, 2013, *Microconical silicon structures influence NGF-induced PC12 cell morphology*, **J Tissue Eng Regen Med**.

Smith LE, Smallwood R, Macneil S, 2010, *A Comparison of Imaging Methodologies for 3D Tissue Engineering*, **Microscopy research and technique**, 73:1123.

Stevens MM, Georg JH, 2005, *Exploring and Engineering the Cell Surface Interface*, **Science**, 310:1135.

Stratakis E, 2012, *Nanomaterials by ultrafast laser processing of surfaces*, **Sci Adv Mater**, 4:407.

Stratakis E, Ranella A, Fotakis C, 2011, *Biomimetic micro/nanostructured functional surfaces for microfluidic and tissue engineering applications*, **Biomicrofluidics**, 5:013411

Su WT, Liao YF, Wu TW, Wang BJ, Shih YY, 2013, *Microgrooved patterns enhanced PC12 cell growth, orientation, neurite elongation, and neuritogenesis*, **Journal of Biomedical Materials Research Part A**, 101A:185.

Sundaram SK, Mazur E, 2002, *Inducing and probing non-thermal transitions in semiconductors using femtosecond laser pulses*, **Nature Materials**, 1:217

Sze SM, 2002, **Semiconductor Devices, Physics and Technology**, Wiley

Taylor AM, Blurton-Jones M, Rhee SW, Cribbs DH, Cotman CW, Jeon NL, 2005, *A microfluidic culture platform for CNS axonal injury, regeneration and transport*, **Nat Methods**, 2:599.

Temenoff JS, Mikos AG, 2008, **Biomaterials: The Intersection of Biology and Materials Science**, Prentice Hall

Tessier-Lavigne M, Goodman CS, 1996, *The Molecular Biology of Axon Guidance*, **Science** 274:1123

Thompson DM, Buettner HM, 2006, *Neurite Outgrowth is Directed by Schwann Cell Alignment in the Absence of Other Guidance Cues*, **Annals of Biomedical Engineering**, 34:669.

Ulrich MD, Rowe JE, Keister JW, Niimi H, Fleming L, Lucovsky G, 2006, *Comparison of ultrathin SiO2/Si (100) and SiO2/Si (111) from soft x-ray photoelectron spectroscopy*, **J. Vac. Sci. Technol. B.**, 24.

Vainio S, Muller U, 1997, *Inductive Tissue Interactions, Cell Signaling, and the Control of Kidney Organogenesis*, **Cell**, 90:975.

Vaudry D, Stork PJ, Lazarovici P, Eiden LE, 2002, *Signaling pathways for PC12 cell differentiation: making the right connections*, **Science**, 296:1648.

Vincent AM, Feldman EL, 2010, *Primary Sensory and Motor Neuron Cultures*, In **Protocols for Neural Cell Culture**, ed. LC Doering, Humana Press

Voldman J, Gray ML, Schmidt MA, 1999, *Microfabrication in biology and medicine*, **Annu Rev Biomed Eng**, 1:401.

Von der Linde D, Sokolowski-Tinten K, Bialkowski J, 1997, *Laser–solid interaction in the femtosecond time regime*, **Applied Surface Science**, 109-110:1.

Wang HB, Mullins ME, Cregg JM, McCarthy CW, Gilbert RJ, 2010, *Varying the diameter of aligned electrospun fibers alters neurite outgrowth and Schwann cell migration*, **Acta Biomaterialia**, 6:2970.

Warren S, Chute RN, 1972, *Pheochromocytoma*, **Cancer**, 29:327.

Wen X, Tresco PA, 2006, *Effect of filament diameter and extracellular matrix molecule precoating on neurite outgrowth and Schwann cell behavior on multifilament entubulation bridging device in vitro*, **J Biomed Mater Res.**, 76A:626.

Whitesides GM, Ostuni E, Takayama S, Jiang X, Ingber DE, 2001, *Soft lithography in biology and biochemistry*, **Annu. Rev. Biomed. Eng.**, 3:335.

Yamada KM, Spooner BS, Wessells NK, 1970, *Axon Growth - Roles of Microfilaments and Microtubules*, **P Natl Acad Sci USA**, 66:1206.

Yang F, Murugan R, Wang S, Ramakrishna S, 2005, *Electrospinning of nano/micro scale poly(L-lactic acid) aligned fibers and their potential in neural tissue engineering*, **Biomaterials**, 26:2603.

Yao L, Wang S, Cui W, Sherlock R, O'Connell C, et al, 2009, *Effect of functionalized micropatterned PLGA on guided neurite growth*, **Acta Biomaterialia**, 5:580.

Young JF, Sipe JE, Van Driel HM, 1984, *Laser-induced periodic surface structure. III. Fluence regimes, the role of feedback, and details of the induced topography in germanium*, **Phys. ReV.B**, 30:2001.

Yuan Y, Zhang P, Yang Y, Wang X, Gu X, 2004, *The interaction of Schwann cells with chitosan membranes and fibers in vitro*, **Biomaterials**, 25:4273.

Zareen N, Greene LA, 2009, *Protocol for Culturing Sympathetic Neurons from Rat Superior Cervical Ganglia (SCG)*, **Journal of Visualized Experiments**, 30.

Zhang K, Jinglei W, Huang C, Mo X, 2013, *Fabrication of Silk Fibroin/P(LLA-CL) Aligned Nanofibrous Scaffolds for Nerve Tissue Engineering*, **Macromol. Mater. Eng.** , 298:565.

Zorba V, 2007, *Study of electron and ion emission mechanisms from micro/nano-structured Si surfaces using ultrashort laser pulses*, PhD thesis, University of Crete, Heraklion

Zorba V, Persano L, Pisignano D, Athanassiou A, Stratakis E, et al, 2006, *Making silicon hydrophobic: wettability control by two-lengthscale simultaneous patterning with femtosecond laser irradiation*, **Nanotechnology**, 17:3234.

Webpages:

http://javiciencias.blogspot.gr/2014_05_01_archive.html

http://jonlieffmd.com/blog/extra-cellular-matrix-is-critical-to-neuroplasticity